2019

Study of effects of rigid body vibrations on external hypersonic flow using smoothed particle hydrodynamics

Tyler Englestad

Study of Effects of Rigid Body Vibrations on External Hypersonic Flow using Smoothed Particle Hydrodynamics

by

Tyler Englestad

A DISSERTATION

Submitted in partial fulfillment of the requirements
For the degree of Doctor of Philosophy
in
The Department of Mechanical and Aerospace Engineering
of
The School of Graduate Studies
of
The University of Alabama in Huntsville

HUNTSVILLE, ALABAMA

2019

In presenting this thesis in partial fulfillment of the requirements for a doctor of philosophy degree from The University of Alabama in Huntsville, I agree that the Library of this University shall make it freely available for inspection. I further agree that permission for extensive copying for scholarly purposes may be granted by my advisor or, in his/her absence, by the Chair of the Department or the Dean of the School of Graduate Studies. It is also understood that due recognition shall be given to me and to The University of Alabama in Huntsville in any scholarly use which may be made of any material in this thesis.

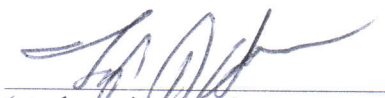

(student signature)

11/7/19

(Date)

DISSERTATION APPROVAL FORM

Submitted by Tyler Englestad in partial fulfillment of the requirements for the degree of Doctor of Philosophy in Mechanical Engineering and accepted on behalf of the Faculty of the School of Graduate Studies by the thesis committee.

We, the undersigned members of the Graduate Faculty of the University of Alabama in Huntsville, certify that we have advised and/or supervised the candidate on the work described in this thesis. We further certify that we have reviewed the thesis manuscript and approve it in partial fulfillment of the requirements of the degree of Doctor of Philosophy of in Mechanical Engineering.

Dr. Jason T. Cassibry — 11/7/19 (Date) — Committee Chair

Dr. Brian Landrum — 11/13/19 (Date) — Committee Member

Dr. Kunning Gabe Xu — 11/8/19 (Date) — Committee Member

Dr. Phillip Ligrani — 11/07/2019 (Date) — Committee Member

Dr. Mark Tillman — 11/7/19 (Date) — Committee Member

Dr. Keith Hollingsworth — 11/13/19 (Date) — Department Chair

Dr. Shankar Mahalingam — 11/13/19 (Date) — College Dean

Dr. David Berkowitz — 11/14/19 (Date) — Graduate Dean

ABSTRACT

The School of Graduate Studies
The University of Alabama in Huntsville

Degree Doctor of Philosophy College/Dept. Engineering/Mechanical and Aerospace Engineering

Name of Candidate Tyler Englestad
Title Study of Effects of Rigid Body Vibrations on External Hypersonic Flow using Smoothed Particle Hydrodynamics

Vibrations plague wind tunnel data and are caused by several factors, such as sensor placement, flow inconsistencies due to imperfect collimation, and the sub-scale model mechanically vibrating upon its mounting apparatus, called a sting. This study focuses on the latter source, particularly at hypersonic velocities, due to fundamental changes that occur within the flow at these speeds. These flow changes differ from those at lower velocities, where the mechanical vibrations are generally superimposed upon the data and thus are easily remove via notch or band-stop filtering. Therefore, traditional post-processing noise removal techniques are not as effective.

This dissertation presents an investigation into these flow changes as well as a computational fluid dynamics (CFD) method to simulate the behavior in order to more effectively characterize, and predict, how sting vibrations affect the data collected within a hypersonic wind tunnel. The CFD techniques used are based on a mesh-free Lagrangian technique called Smoothed Particle Hydrodynamics (SPH) in which the solid boundaries are able to move about as necessary, i.e. model vibrations, in contrast to more traditional, static gridded CFD codes.

The SPH method is first verified in 2D and 3D flow cases, and then validated against actual wind tunnel data, wherein the noise itself it modeled and matched. Confident in the method's accuracy, simulations are then performed with vibrations based on a hypothetical sting. The results show the sting's frequencies are not superimposed upon the output data, with some frequencies shifted or attenuated, which is caused by fundamental changes in the hypersonic flow itself.

Abstract Approval:

Committee Chair _____ 11/7/19 (Date)

Department Chair _____ 11/13/19 (Date)

Graduate Dean _____ 11/14/19 (Date)

ACKNOWLEDGEMENTS

First and foremost, I would like to thank my advisor, Dr. Jason Cassibry. Throughout my long and tenuous topic selection and personal problems, he stuck with me and offered encouragement and advice. I have never met a more dedicated educator, mentor, and friend throughout my academic career. I am proud to call him my advisor.

Next I would like to thank my parents, John and Rena. From a young age I was always expected to get good grades and attend college, and that lifelong encouragement left a substantial imprint. As a result, I have always enjoyed school and learning, and is the primary reason I continue my education.

I also want to thank Dave Keen and Barbara Breland. Dave was my first mentor, fresh out of college at a small contracting firm, and continues to provide sage life advice. I'll never forget Dave calling me a doctoral candidate when I had barely started graduate school at all. Similarly for Barbara, the life experiences and guidance has been immensely helpful. Both of them have gotten me through some tough times and for that I am eternally grateful.

Finally, I would like to thank my girlfriend, Loralei Oswald. It's been a whirlwind couple of years, full of adventure and wonder, and I look forward to many more.

TABLE OF CONTENTS

LIST OF FIGURES

LIST OF TABLES

LIST OF SYMBOLS

SYMBOL	DEFINITION
C_d	drag coefficient
C_l	lift coefficient
C_m	pitching moment coefficient
ρ	density (kg/m^3)
P	pressure (N/m^2)
d	characteristic length for aerodynamic coefficients (m)
h	SPH local smoothing distance; also called particle spacing (m)
M	Mach number
c	speed of sound (m/s)
V	volume (m^3)
k	thermal conductivity (W/m·K)
m	mass (kg)
S	area for aerodynamic coefficients (m^2)
γ	specific heat ratio (c_p/c_v)
Π	artificial viscosity (m/s^2)
η	shear viscosity (kg/m·s)
ζ	bulk viscosity (kg/m·s)
θ	deflection angle
W	kernel smoothing function)
τ	Deviatoric stress tensor

O()	Big O notation of algorithm computational complexity
σ	standard deviation
$_a$ (subscript)	SPH particle in question
$_b$ (subscript)	shorthand for all the neighbors of the particle in question
$\bar{A}_{ab}$ (bar)	shorthand for the average value of A between the particle in question and all its neighbors
$_{ab}$ (subscript)	shorthand for the difference in a parameter, such a position or velocity, between the particle in question and all its neighbors
$_0$ (subscript)	shorthand for initial and/or free-stream value

CHAPTER 1

INTRODUCTION

This dissertation investigates vibrations that occur in hypersonic wind tunnels, how these vibrations impact the flow over the test article, and a novel approach to modeling these phenomena. Noise plagues almost all wind tunnel data and is caused by several factors [1,2], including but not limited to, sensor accuracy or placement, precision of the acquisition equipment, unintended flow perturbations within the test section of the tunnel due to imperfect collimation, and the sub-scale model mechanically vibrating in space [3]. The latter source of measurement errata is the primary focus of this study.

While computational fluid dynamics (CFD) has come a long way to accurately estimate aerodynamic performance of aircraft, it typically is not fully predictive—it must be validated with known information [4]. Said another way, while CFD is an immeasurably important tool aiding aircraft design, it is not quite capable of completely estimating all the necessary aerodynamic parameters of an aircraft before test flights and must be anchored with verified, trusted information [5]. Wind tunnels are the primary source of ground-truth data for aerodynamic measurements. However, as wind tunnel experiments are very expensive, therefore there is a need for blended wind tunnel experimentation and CFD; wind tunnel experimentation is used to point verify

aerodynamic parameters for a set of conditions. The CFD model is then used to parametrically analyze the flowfield within the validated data.

However, wind tunnel data is imperfect; the data has noise superimposed upon the measurements of interest which must be dealt with. A large contributor to this errata is the spatial movement of the wind tunnel model itself, caused primarily by the model vibrating on its mounting apparatus—called a sting—within the tunnel's test section [6]. Sting designs have several, somewhat conflicting, requirements. It needs to be substantial enough to hold the model effectively while being minimal such that it does not impact the flow characteristics over the model. As a mechanical device, even carefully designed stings bend and vibrate at measurable resonate frequencies, thus superimposing noise at these fundamental frequencies on the measured signals. Typically, this particular type of noise is dealt with by applying band-stop (also called "notch") filters on the data during post processing [7]. This works with acceptable results at subsonic, where the ratio of velocity to the speed of sound, or Mach, is less than 1, and transonic ($0.8 < \text{Mach} < 1.2$) velocities. At higher flight speeds (i.e. supersonic; $1.2 < \text{Mach} < 5$), these vibrations are known to impact the flow more so than simply superimposing noise upon the signals [8]. However, previous post-processing and filtering approaches still match flight test data adequately for aircraft design purposes due to the relatively low stagnation pressures and temperatures not typically threatening the airframe. At hypersonic velocities ($\text{Mach} > 5$), these vibrations fundamentally affect the flow over the vehicle, in addition to the noise superimposed on the sensor measurements. Specifically, at hypesonic speed the post-processed data still has the effects of the

vibrations within, even though the obvious resonant-frequency noise has been filtered out.

As will be expanded upon in the literature review in Chapter 2, there is limited previous work in simulating vibrating wind tunnel test articles because moving boundaries in typical gridded CFD codes is difficult for high-frequency vibrations in M > 5 flow. Due to the complications of noisy data at hypersonic speeds, this leaves open the opportunity to study these effects within a flow field which can capture these effects. The hypothesis is, for hypersonic wind tunnel data, the noise cannot simply be filtered out as with slower flight regimes, and these vibrations fundamentally alter lift and drag computations to an extent beyond the superimposed noise on the measurements. The goal of this dissertation is to study these phenomena using a mesh free Lagrangian technique where vibrating the model is trivial, allowing us to compare vibrating and stationary models to study this hypothesis.

1.1 Hypersonic Flow

Hypersonic flow is broadly defined as the regime where the free-stream velocity is more than 5 times the speed of sound, i.e. the Mach number is greater than 5. In contrast with other flow regime delineations, there are no physical discontinuities that exist at this velocity, it is defined as such simply a matter of convenience [9]. For example, subsonic flow (Mach < 0.8) is generally classified as where there are no locally supersonic regions anywhere on the aircraft. Transonic flow (0.8 < Mach < 1.2) is roughly defined as where incompressible assumptions are no longer valid and the presence of sonic (Mach = 1), or higher, areas of flow somewhere on the vehicle (most

commonly on top of the wings) with some sub-sonic regions persisting. Supersonic flow is delineated as when all the flow around the aircraft is no longer transonic and must be modeled as compressible. This regime is where shocks begin to appear and greatly influence the flow. However, perfect/ideal gas assumptions are still generally valid. Hypersonic flow, on the other hand, is a softer boundary, with several defining approaches converging upon the Mach > 5 boundary [9–11]:

- Aerodynamic heating is of greater concern, strongly driving aircraft designs. So much so the air itself is sometimes heated to the point of dissociation and ionization (generally important at Mach > 10, but can occur earlier)
- The specific heat at constant pressure, C_p, and constant volume, C_v, and their ratio, γ, therefore are no longer constant, invalidating most standard supersonic equations of motion, such as oblique shock relations that assume a constant γ
- Shock interactions are stronger and greatly impact vehicle design as they can cause catastrophic airframe failure if not planned for and mitigated properly
- Traditional rockets and air-breathing SCRAM jets are the only propulsion options

These flow regimes along with their typical flight altitudes and representative vehicle shapes are shown in Figure 1.1

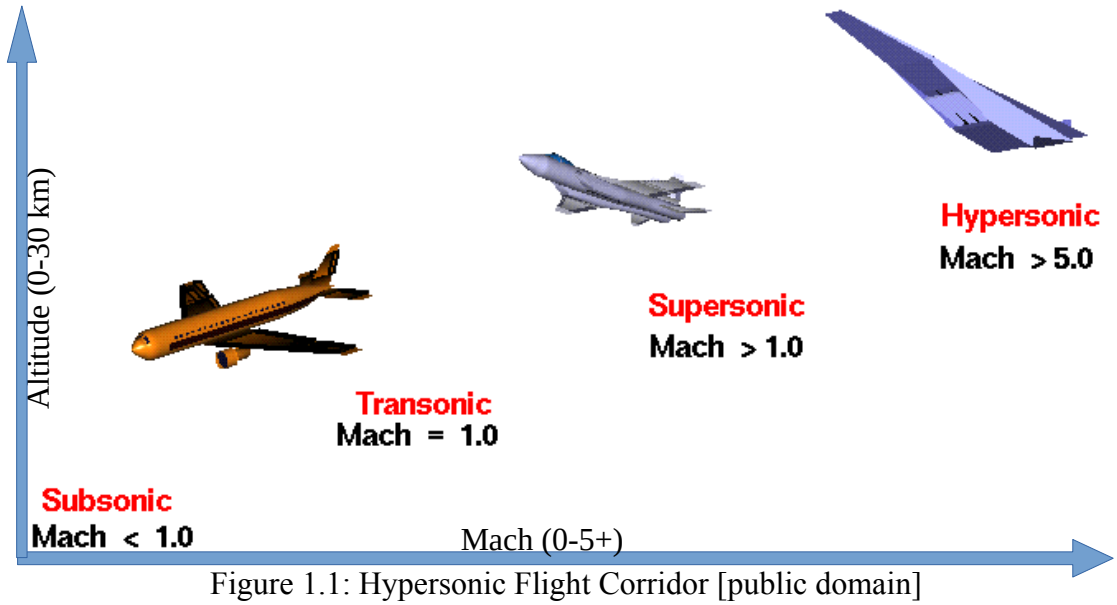

Figure 1.1: Hypersonic Flight Corridor [public domain]

Hypersonic vehicle design is difficult due to the fact that it is and engine integrated airframe—no elements of the aircraft are independent from one another. Every component can potentially disrupt the flow that impinges upon another component, and any of the above mentioned hallmarks of hypersonic flow can cause catastrophic failure. It is important to fully characterize the behavior of the flow over the body to as great an extent at practicable, before attempting expensive, and dangerous, full-scale flight tests (manned or otherwise).

For the purposes of this dissertation, the fluid is assumed to maintain state (not dissociate) and γ is constant, as these assumptions allowed the simulations to still adequately match empirical and theoretical results. More details of the hydrodynamic assumptions used in this study are presented in later sections.

1.2 CFD Approaches

Throughout the pursuit of flight, at higher altitudes and faster velocities, aircraft and spacecraft designers have continually leaned upon modeling and simulation in order to predict the aerodynamic behavior of full-scale aircraft. Producing and flying aircraft is an expensive and dangerous process, especially if their sole purpose is for testing, so any methods to connect the theoretical calculations and expectations to real life phenomenon is a welcome option. For the first few decades of flight, wind tunnels (or sub-scale flight) were the primary option; the only stepping stone between the theoretical equations of motion and flying real aircraft. Once computers became sophisticated and fast enough, however, virtual wind-tunnels via CFD came to the forefront. Early versions solved wind-tunnel-derived empirical formulas, filling in the gaps between experimental points from wind tunnel data. Further refinement led to CFD implementing more general equations of motion, including discretized Navier-Stokes equations and the like [12].

In order to solve the equations of motion, CFD approaches can be divided into 2 major categories: Gridded (Eulerian) and non-gridded (typically Lagrangian) solvers. For most of the history of CFD, gridded methods have been at the forefront, perhaps due to their relative computational simplicity or simply the direction of research at the time [13]. In the last few decades, however, non-gridded (and unstructured grid) approaches have become more popular, especially for rarefied (very low-pressure) and hypersonic (high-speed) flow [14]. Since this dissertation is primarily about hypersonic flow and the simulation thereof, this section will focus on some of the most commonly used CFD

approaches for modeling hypersonic flow. The following section will provide an introduction to the method used in this dissertation.

1.2.1 Eulerian-based (gridded)

Gridded codes generally fall into 3 categories: finite-difference, finite-volume, and finite element methods. Over the course of history and refinement, each has found its niche for different modeling scenarios—for example, finite-element has become the forefront technique for modeling load analysis [15], while finite-volume is popular for fluid flows [16,17]. However, for the purposes of this discussion, it is the common characteristic between them all that is important—the initial grid structure. It is this unmovable grid, carefully constructed within the control volume to maximize accuracy where transitions in the flow are most likely, which generally lends it best to simulating steady-state, static flows. This is due to the fact that, in the most simple terms, all flow within a grid's miniature control volume is considered homogeneous. In hypersonic flows, however, large changes in the flow can occur in relatively small distances. Additionally, several large modifications are required in order to allow the grid to move during the simulation, such as modeling vibrations, generally with a Lagrangian method providing that modification, as discussed later.

1.2.2 Direct simulation Monte Carlo (DSMC)

DSMC is a non-gridded probabilistic approach to solve the Boltzmann equation for rarefied or hypersonic flow, first proposed by Dr. Bird of the University of Sydney. It is similar to Lagrangian codes in that it is particle-tracking based. However, the primary

equation of motion describes the statistical behavior of a non-equilibrium thermodynamic system; meaning it provides a probability of where a particle is located in space and its momentum—from these, other parameters are derived, such as temperature and density. Extensions of the method have used the Boltzmann equation to derive fully conservative fluid dynamic equations [18].

DSMC has been shown to provide excellent results for blunt bodies [19], especially at higher Mach numbers than those studied in this dissertation, and is typically associated with reentry dynamics (very high Mach and altitude) [20], including reconstruction of the STS-107 disaster [20], and weapon reentry vehicle dynamics [19].

1.2.3 Arbitrary Lagrangian-Eulerian (ALE)

Arbitrary Lagrangian-Eulerian codes try to mix the best of both worlds between gridded and non-gridded CFD approaches. These codes tend to heavily modify a gridded Eulerian code with a Lagrangian subroutine whose purpose is to provide in-situ modification to the grid. More specifically, at each time step, flow parameters such as pressure are calculated via Eulerian methods; these are handed to a Lagrangian subroutine which determines if any of these pressures would have caused the body or airframe under analysis to deform (perhaps over-pressure on a wing surface). If so, the Lagrangian subroutine modifies the grid and returns this new grid to the Eulerian code for the next time step. This computationally complex code can achieve very accurate results, even for dynamic bodies, at the expense of code complexity and runtime [21–24].

1.3 Smoothed Particle Hydrodynamics (SPH)

Smoothed particle hydrodynamics is an implementation of the mesh-free Lagrangian fluid mechanics model to solve equations of state in physical systems, contrasting with gridded, Eulerian approaches. Originally conceived to simulate astrophysical phenomenon [25], it has been adapted for use in other large-scale simulations, including dam-breaking flows [26], soil erosion [27], as well as smaller-scale free-surface flow [28], turbine internal flow [29], wave-impact on solid surfaces [30], and plasma-electrode erosion behavior [31].

Mesh-free simulations, such as SPH, are initialized with a simple collection of points directly carrying state information. These particles, the analogue to finite method grid points, move within the simulation as Lagrangian particles and their physical properties (temperature, pressure, density, etc) are interpolated via a nearest-neighbor weighted kernel function. The use of these individual particles bring several advantages, which will be discusses in more detail later, including: material property differences are easily modeled (static vs. dynamic, molecular species, etc), parallelizable computations lending well to high performance computing modifications [32], and the aforementioned grid-less setup skips the time-consuming mesh-generation steps required in finite difference or finite volume methods. The down-side is boundary conditions are more difficult to implement [33].

1.3.1 Overview of SPH

SPH was first theorized and described by Gingold and Monaghan in 1977 as a means to more accurately predict and model the behavior of astrophysical phenomenon, specifically protostar formation within a dense interstellar cloud [25]. It is a particle method and therefore does not need a grid to calculate spatial derivatives nor gradients, nor is the complicated initial step of grid setup required. Instead, derivatives and gradients are determined by statistical differentiation via a weighted interpolation function, described in detail in a later chapter. This lends itself well to being extensible to much more complex problems than astrophysical systems, however it is computationally intensive and solving the gradient functions at boundaries can be difficult [34]. The state of the art in both computing capabilities and boundary conditions has made extensions of SPH into other simulation domains more readily implementable. A deeper history of SPH and current cutting-edge implementations, particularly in modeling high-speed flow, will be described in Chapter 2.

1.3.2 Merits and Challenges

One of the biggest benefits to using SPH for this dissertation's analysis is the fact that, being particle-based and non-gridded, the experimenter is free to move the boundary points at will anytime during the simulation. More specifically, to fulfill the objectives herein, implementation of vibrations is somewhat trivial—the boundary points can simply have the harmonic motion directly overlaid upon their initial spatial positions and the simulation will adjust accordingly. This is due to the fact that, from a fluid particle's perspective, when a boundary moves the fluid particle's pressure changes accordingly,

just as if it was encountering another fluid particle, and the other state variables (temperature, density, etc) follow as well.

However, there are a couple complications to take into account before considering SPH as a panacea for all things fluid mechanics related:

- First, boundary conditions can be difficult to implement. In fact, this is a large, active research area within the SPH community [34–36]. In this implementation, relatively simplistic boundaries are imposed, consisting primarily of treating fluid and boundary interactions as elastic collisions (similar to Newton's Method) [37], with the fluid particle being deflected as necessary in order to not penetrate the boundary. Another method includes the use of ghost particles; effectively, mirrored particles on the other side of a boundary in order to fully satisfy the kernel function, which will be discussed further in Chapter 2. This issue tends to lead SPH to be slightly less accurate than some of the best gridded/Eulerian-based codes used to simulate fluid flow, but the results can still be within reasonable error for aircraft performance prediction (within ~10%).
- Second are the computationally intensive algorithms necessary to properly implement SPH. SPH implementations calculate the spatial derivatives and gradients by satisfying a weighted statistical average over an arbitrary number of nearest neighbors of each fluid particle (for a cubic spline in 3D, typically around 45 points contribute to the summation interpolant; 60 are used in this implementation to facilitate vectorized code). Nearest neighbor algorithms tend to have a time complexity on the order of N, also written as O(N), where N is the

number of particles in the simulation. When a typical simulation can have on the order of 100,000 points, over which the algorithm runs for each particle, this becomes computationally challenging quickly. As computational power has increased over time, as well as state-of-the-art hardware techniques (e.g. processing on graphics cards) [32], this has become a manageable problem. However, in the case of processing on graphics cards, memory becomes the next limiting factor.

1.4 Objectives of Dissertation

This dissertation investigates the applicability of previous wind tunnel data noise reduction techniques, such as filtering, for use with modern hypersonic flow. Noise in wind tunnel data is an unavoidable problem, produced via several aforementioned causes and previous filtering techniques are not sufficient for use with hypersonic analyses. For the first time, vibrations upon sting-mounted test articles are modeled and similar filtering techniques are applied in order to compare the results and determine the errors thereof.

Previously, the noise in wind tunnel data caused by mounting hardware deflection and vibration was filtered and the resulting reduced data used for vehicle analysis. This reduced and filtered data is then used to validate the CFD models used for the overall vehicle design. This method does not capture all of the inherent vibrations themselves caused fundamental flow alterations, such as minor eddies that impact further along the test article.

Alternatively, this dissertation intends to model the entire wind tunnel test environment, including the sting and test article; a novel capability provided by the use of Lagrangian code vice the structured grids typically used in aircraft CFD. This allows the designer to avoid a data reduction and filtering step, thus minimizing the possibility of losing critical data. Is it the author's contention that any artificial removal of experimental data, filtering or otherwise, is a chance at removing something important and useful.

There are several overarching objectives to the research presented in this dissertation. First and foremost is the advancement of the state-of-the-art for using SPH to model hypersonic flow. This is accomplished by verifying and validating (V&V) SPH results with both empirical closed-form solution data and wind tunnel experiments found in literature. The V&V is accomplished for hypersonic flow over a 2D flat plate at several angles of incidence (i.e. a compression corner) and right circular cones with multiple half-angles.

1.5 Summary of Approach

To satisfy the goals of this dissertation, SPH is used to simulate and reproduce the effects of wind tunnel model vibrations caused by sting deflections. This is accomplished via a building-block approach:

- SPH is first validated for 2D hypersonic flow (M = 5), specifically a compression corner with varying angles of incidence (10°, 15°, 20°, and 25°). The results are

compared to oblique shock theory. Stretch cases including a mild supersonic flow (M = 2) and a differing gas (CO_2, M = 5, γ = 1.3) are also presented.

- Building upon those results, SPH is then verified and validated for hypersonic flow (M = 5) over right circular cones, of varying cone half-angles (5°, 10°, 15°, 20°, 25°), with results compared to Taylor-Maccoll theory and wind tunnel data. Similar stretch cases of mild supersonic and a different fluid are again included.
- The conical models are then vibrated within SPH simulations similar to real-world data obtained via literature of wind-tunnel experimentation results [7]. The simulation data and wind tunnel data are processed similarly to make quantitative comparisons between the experiment and simulation to provide validation of the methods used to study vibrations and filtering in this dissertation. Additionally, pre-processed data are compared in order to see if the flow was fully characterized. This, in effect, validates SPH for modeling vibrations in wind tunnel data, and allows for future post processing techniques to be better tested before being used to filter out possibly important and useful data.

1.6 Synopsis of the Dissertation

The primary goal of this dissertation is to investigate potential departures from the assumption that notch filtering does not filter out real data at hypersonic velocities. This is done by modeling the vibrations, validating the approach, and finally, performing similar post-processing on both simulated and real data to see if they arrive at the same post-shock flow properties.

The remainder of this dissertation is organized as follows. Chapter 2 includes a literature review of the areas of interest, including current modeling states-of-the-art, computational processing techniques, and a brief background of SPH. Chapter 3 describes the governing equations used in SPH, the modeling approach, and the validation procedures in depth. Chapter 4 presents the results thereof, including the building-block approach used to validate SPH for hypersonic flows. Finally, conclusions, the benefits of the work, and future research opportunities are described in Chapter 5.

CHAPTER 2

LITERATURE REVIEW

The modeling of hypersonic flow is a challenging field with substantial ongoing research. This chapter will guide the reader through the history and state-of-the-art via literature pertaining to the objectives of this dissertation, as well as more in-depth reasoning behind the method chosen, SPH, to tackle those goals.

2.1 Sting Interference and Vibrations in Wind Tunnels

The wind tunnel model mounting apparatus, called the sting, and its effects on the flow have plagued experimenters since wind tunnels were invented. In 1960, using delta-wing models at Mach 6.8 with base-mounted stings angles of incidence between 0-20°, Peckham [38] noted sting length and diameter play a significant role in the transition from laminar to turbulent flow; and if the sting must be kept short to limit deflections, it is helpful to encourage the flow to transition to turbulent ahead sting. It was further noted, for aft and base-mounted stings, the diameter directly influences the base pressure measurement, with slimmer sting producing the most accurate results, albeit with higher probabilities of shock standoff interfering upstream with the model.

The body of literature grows in the early 1970's, with Pick [39] investigating the effects of a sting on sharp cones at Mach 6.3 and 9.9, concluding below an angle of attack of 15°, the base-mounted sting effects, while present, could be mitigated via several pressure transducers mounted around the base and averaging the values. Between 15-40° angle of attack, the pressure distribution is greatly distorted and varied greatly between sting-mounted and free-flight models, with usable results sometimes being available via careful pressure probe placement and interpolation. Above 40° angle of attack, the pressure distribution is so corrupted there was no hope of matching free-flight models with sting-mounted ones.

Mabey [40] detailed the effects of sting interference via deflections and vibrations at subsonic and transonic speeds of jet engine inlet diffusers. It was determined that typical sting vibrational modes occur between 20-900 Hz and could be divided into 2 subcategories based on the effects they caused: light buffeting which was associated with minor vortex separation and heavy buffeting which caused flow separation on the body. At the time, the tunnel and stings themselves were modified to mitigate these issues. Similarly, albeit at slightly lower vibrational frequencies (10-16 Hz), due to different sting design parameters, Young [3] found angle of attack sensors were unable to distinguish the gravity vector effectively from model deflection and vibrations, and required significant post-process filtering to recover usable data, primarily affecting the drag and pitching moment data. More recently (2017), Liu [7] studied a 10° half-angle right circular cone at Mach 7 and determined that the sting had vibrational modes of 40

and 55 Hz causing fluctuations in drag calculations which were later filtered during post-processing.

Likewise, Billingsley [41] documented sting deflection and vibration caused by the shock loading associated with the initial aerodynamic loading of the wind tunnel flow impinging upon the model. For the models studied, these severe initial loads would sometimes break the sting and destroy the model and test suite, so stiffer sting materials were investigated in order to maintain a thin sting diameter while providing the strength and rigidity necessary to handle the forces.

Reding and Ericsson [42–44] compiled and studied several wind tunnel datasets attempting to characterize sting deflection and vibration effects. The analyses included data from subsonic through high-hypersonic (Mach = 20). While predicting the flow effects a-priori proved challenging, the analyses provided insight into post-processing mitigation methods—perhaps the first attempt at modeling the deflections and vibrations—one of which is to test a model with several diameter stings with different dynamic deflection characteristics and attempt to extrapolate zero-sting data, likely leading to very expensive wind tunnel testing.

In addition to studying sting deflection effects, mitigation strategies varied over the decades. In an early example from 1968, Igoe [45] was able to reduce wind tunnel model vibrations of a low-supersonic (Mach ≈ 1.3) aircraft via installing a tuned mass-dampener into the model itself. This method reduced the pitch vibrations by roughly 50% at the expense of inherently modifying the model possibly causing later issues with measuring other aerodynamic parameters, such as pitching moment.

Beginning in the 1980's and continuing into the present, more active mitigation strategies were developed. Combining both a movable sting and a closed-loop feedback mechanism, He [46] and Shen [47] studied several control algorithms in order to reduce model vibrations—the work of Shen reduced vibrations by roughly 88% using a cutting-edge Neural Network Proportional-Integral-Derivative (NNPID) control loop. He's efforts reduced measured displacements by roughly 91% using in-situ filtering of the data at a-priori known sting vibration frequencies.

Most recently, in parallel to characterization and mitigation research, the topic of modeling the vibrations has been breeched; a significant gap documented by Barber [12,48]. In 2009, Ye [6] used a (gridded) Unsteady Reynolds-Average Navier-Stokes code to predict the effect of vibrations on high-aspect wings at high angles of attack. One interesting finding of this work includes the onset of stall occurring 2° sooner while vibrated versus static, due to vortex shedding at the wingtips creeping up the wing span, detaching the flow sooner than expected. Along a similar vein, Šidlof [49] measured a symmetrical NACA0015 airfoil, at Mach = 0.3, vibrating within 2 degrees of freedom—pitch and plunge—at 14.5 and 16.8 Hz, and modeled the behavior [50] with the gridded OpenFOAM CFD code with mixed results, matching overall values sufficiently with phasing mismatch as compared to measured data. The conclusions state the gridded CFD's ability to handle the quickly moving airfoil required very small time steps, thus requiring immense computational time, hereby limiting the simulation.

2.2 History of SPH

SPH was first conceived in 1977 by Gingold and Monaghan, influenced by a lecture given by Leon Lucy in 1976 [25], as a new hydrodynamic code in order to simulate stellar models. It was observed, for these types of simulations, gridded codes were unacceptable due to the large numbers of grid points necessary to capture the flow accurately, whereas as few as 80 particles could be used in SPH to achieve reasonable results (within a few percent). This was particularly useful at the time, due to computing power and memory constraints.

Over the decades that followed, SPH continually evolved to become more capable outside stellar gas cloud modeling, such as magnetohydrodynamics [51], in order to include magnetic effects in fluid flows; useful for plasma or liquid metal modeling. In 1993, the Workshop on Advances in Smoothed Particle Hydrodynamics was held to discuss the (then) state-of-the-art for the method and modifications implemented to extend SPH's capabilities [52]. For instance, the addition and continued enhancement of boundary conditions allows for modeling fluids interacting with walls; a pivotal development for later use in smaller-scale applications. Shock capturing via artificial viscosity, an improvement added to address fast-moving stellar gas interaction, proved useful in all manner of other SPH applications, from free-surface flow to internal turbine flow and external aircraft simulations. This section will delve into the most pertinent of these enhancements and how they have broadened the applicability of SPH.

2.2.1 Astrophysical Beginnings

SPH was first developed to overcome the shortcomings of gridded, finite-difference methods when used to model stellar gas cloud and accretion disc interactions, as best summarized by Monaghan in 1988 [53]. The primary benefits realized for this implementation includes no dissipation; accurate advection; and exact conservation of mass, momentum, angular momentum, energy, and entropy. However, its disadvantages include: dissipation must be explicitly added, where needed, such as in post-shock regions, and noise can appear in the results due to the lack of flexibility in the exact conservation [54,55]. Modifications over time, primarily the addition of artificial viscosity to be discussed in depth later, have mostly alleviated these shortcomings and SPH is still widely used in this field [51,56].

2.2.2 Developments in SPH Techniques Pertaining to Hypersonics Applications

SPH first saw usage within the realm of super- and hypersonic flow in 1993 when Amdalh [37] compared the SPH predicted flow to theoretical results of air at Mach 2 into a 14.75° compression corner followed by a return to axial flow via an expansion fan. For this single case, SPH accurately predicted the post-shock pressure and density very well, within 3%, and Mach number within 10%. No other flow parameters were presented. It was noted, however, shocks were on the order of 3 particles “thick”. While significantly thicker than real life, did not appear to negatively affect the overall results. It should also be noted that these results were computed on a Cray supercomputer of the time and the author mentioned the significant computational cost associated with the SPH method.

In recent years, there are more examples in the literature of this method being used in aerodynamic applications. This is likely due to the advances in computing capabilities and the limitations of traditional, gridded approaches. Moylan [57], via Stellingwerf [58], used SPH in a slightly different—yet related—manner to calculate droplet demise behavior after going through the shock generated by a 10° wedge encountering air flow at Mach 2, 4, and 6. As part of this effort, SPH accurately predicted the shock angle and the post-shock droplet Mach number, to within a few percent, however no other thermodynamic parameters (density, etc) were compared.

Perhaps the most recent, and comparable, publication in the literature is the work by Silla [13] in 2017. Here, compression corners were again simulated, and the shock angle of a Mach 3.8 air flow was compared to theoretical results. Six deflection angles (15°, 20°, 25°, 30°, 35°, and 38°) were analyzed and the largest error between modeled and theoretical oblique angles was 2.98%. Unfortunately, no other flow parameters were compared. These results did include an empirically-adjusted coefficient in the boundary condition repulsion force used to keep fluid particles from penetrating the walls.

2.2.2.1 Boundary Conditions

The treatment of boundary conditions in SPH is an area of research of SPH users. Since its initial inception of mostly modeling gas clouds, which were expected and encouraged to interact and penetrate one another, boundaries did not become an issue until SPH was extended into other areas, such as free-surface flow, where the fluid is not expected to penetrate the walls of the container. Considering this topic has so much

literature, primarily dealing with boundary conditions useful for incompressible flow, this section will deal with the methods used with high-speed, compressible flow.

Silla [13], in studying compression corners with SPH, used a combination of 2 techniques: ghost particles and a Lennard-Jones-like molecular repulsion force. Ghost particles are "mirror image" particles enplaced, every time step, mirroring fluid particles at a boundary. Said another way, as a fluid particle approaches a boundary, therefore excluding space from the weighted kernel function, mirror image (ghost) particles are placed at points on the opposite side of the boundary corresponding to the particles real fluid neighbors, with the same flow properties as those neighbors. This allows the interpolation integral to work as expected over the whole local smoothing distance, and attempts to create a repulsive force to prevent fluid particles from penetrating the boundary. This typically works for slow-moving flow, but for supersonic and hypersonic flow, additional measures were necessary. This additional repulsive force was a Lennard-Jones-like repulsion force

$$\boldsymbol{f}_r = \begin{cases} D\left[\left(\frac{h_0}{r_{ab}}\right)^{12} - \left(\frac{h_0}{r_{ab}}\right)^{6}\right]\frac{\boldsymbol{x}_{ab}}{r_{ab}^2} & \left(\frac{h_0}{r_{ab}}\right) > 1 \\ 0 & \left(\frac{h_0}{r_{ab}}\right) \le 1 \end{cases} \tag{2.1}$$

where h_0 is the initial particle spacing; r_{ab} is the distance from the particle to its wall neighbors; x_{ab} is the vector from the particle to its wall neighbors; and $D = a[max(V)^2]$, a parameter tied to the maximum particle wall-approaching velocity, with a adjusted

empirically to match theoretical results. This produces a wall-repelling force roughly proportional to the speed at which a particle is approaching a wall. It should be noted, Stellingwerf [58] attempted these analyses with ghost particles alone, however does not appear to have been able to match post-shock flow properties outside of shock angle.

Another approach to handle boundary conditions for high speed flow is the use of geometrical boundaries, as used by Amdahl [37] to model compression corners. In this method, boundaries are defined by a list of line segments, each with a boundary condition value set. These include inflow, outflow, and inviscid. Inflow and outflow boundaries are straightforward—outflow boundaries simply remove a fluid particle from the particle list, inflow boundaries input fluid particles into the simulation with predefined parameters. Inviscid boundaries intend to contain the fluid particles within the boundaries of the simulation. As a fluid particle approaches to intersect the boundary line-segment, it is reflected away from the wall, maintaining their parallel velocity component while negating the perpendicular component. This is done with no actual wall particles implemented; simply the geometrical line segments as mentioned earlier. The downside to this approach is the long list of line segments generated for complex geometries—the boundary list could quickly approach the complexity of a grid, which is a main issue being avoided with the use of SPH. However, this elegant solution did inspire the one used in this dissertation, but instead of defining boundary condition line segments, wall particles are used to define the boundaries, and fluid particles reflect away from wall particles as part of a quickly-running search routine, discussed in the Chapter 3.

2.2.2.2 Artificial Viscosity and Shock Capturing

Artificial viscosity is the set of equations that give a CFD code the ability to capture shock formation and prevent particle penetration. The Navier-Stokes momentum equation for viscous flow, in vector notation, is

$$\frac{\mathrm{d}v_i}{\mathrm{d}t} = -\frac{1}{\rho}\frac{\partial P}{\partial x_i} + \left[\frac{\partial}{\partial x_k}\left(\eta\left(\frac{\partial v_i}{\partial x_k} + \frac{\partial v_k}{\partial x_i} - \frac{2}{3}\delta_{ik}\nabla\cdot v\right)\right) + \frac{\partial}{\partial x_i}(\zeta\nabla\cdot v)\right] \tag{2.2}$$

where η and ζ are the shear and bulk viscosity, respectively, and v is the velocity in the respective axial direction. This could have been estimated directly using the SPH interpolation scheme, but it was found to not perfectly conserve linear and angular momentum [59]. Alternatively, for SPH, Monaghan [60], in 1983, first proposed an analogue to the Von Neumann-Richtmyer method typically used in gridded codes [61,62]

$$\Pi = \begin{cases} \alpha\Delta x^2\rho(\nabla\cdot\boldsymbol{v})^2 & \nabla\cdot\boldsymbol{v} < 0 \\ 0 & \nabla\cdot\boldsymbol{v} \geq 0 \end{cases} \tag{2.3}$$

where α is a non-dimensional constant approximating shear viscosity, $\boldsymbol{v}$ is velocity, and Δx is the position of adjacent grids. This simple implementation consisted of

$$\Pi_{ab} = -\mu\left(\frac{v_{ab}\cdot\boldsymbol{r}_{ab}}{r_{ab}^2 + \epsilon\bar{h}_{ab}^2}\right) \tag{2.4}$$

where v_{ab} and r_{ab} is the velocity and spatial difference between a particle and its neighbors, respectively, ε ~ 0.01 to prevent a division-by-zero when $\mathbf{r}_{ab} = 0$, h_{ab} is the

average local smoothing difference between a particle and its neighbors, and μ is defined as

$$\mu = \frac{\alpha \bar{h}_{ab} \bar{c}_{ab}}{\bar{\rho}_{ab}} \tag{2.5}$$

where, again, α is approximated as shear viscosity (a constant), c_{ab} and ρ_{ab} is the average speed of sound and average density between a particle and its neighbors, respectively, which is all incorporated into the standard SPH acceleration term

$$\frac{\mathrm{d}v_a}{\mathrm{d}t} = -\sum_b m_b \left(\frac{P_a}{\rho_a^2} + \frac{P_b}{\rho_b^2} + \Pi_{ab} \right) \nabla_a W_{ab} \tag{2.6}$$

This, while elegant and simple to implement, had a tendency to provide too much repulsive force between particles, and had no provisions for bulk viscosity and the lack of the piecewise functionality reducing the effect during particle expansion. Common modifications to this "baseline" Monaghan artificial viscosity formulation include the addition of "switches", an example proposed by Monaghan in 1992 [63], in order to have the effects only turn on where particles are on collision courses and turn off in areas of pure shear or expansion, for instance

$$\Pi_{ab} = \begin{cases} \dfrac{-\alpha \bar{c}_{ab} \mu_{ab} + \beta \mu_{ab}^2}{\bar{\rho}_{ab}} & \boldsymbol{v}_{ab} \cdot \boldsymbol{r}_{ab} < 0 \\ 0 & \textit{otherwise} \end{cases} \tag{2.7}$$

where α is effectively shear viscosity, β an approximate bulk viscosity to prevent penetration at high approach speeds [64], and μ is redefined as

$$\mu_{ab} = \frac{\bar{h}_{ab} \boldsymbol{v}_{ab} \cdot \boldsymbol{r}_{ab}}{\boldsymbol{r}_{ab}^2 + \epsilon h_{ab}^2} \tag{2.8}$$

which causes viscosity to vanish, via the piecewise function, when particles are moving away from one another. However, it would still sometimes produce an effect in strong shear situations (e.g. stationary boundaries with adjacent supersonic flow), due to minute converging velocities causing the dot product to be positive. The addition of the Balsara switch [56,65,66],

$$B_i = \frac{|\nabla \cdot \boldsymbol{v}|_i}{|\nabla \times \boldsymbol{v}|_i + |\nabla \cdot \boldsymbol{v}|_i} \tag{2.9}$$

which is appended to the μ term from earlier

$$\mu_{ab} = \frac{\bar{h}_{ab} \boldsymbol{v}_{ab} \cdot \boldsymbol{r}_{ab}}{\boldsymbol{r}_{ab}^2 + \epsilon h_{ab}^2} B_i \tag{2.10}$$

further inhibits the effects of viscosity and typically solves shear and convection problems in most SPH use cases, namely gaseous cloud collisions and the like.

Artificial viscosity switches are still an active area of research, with the latest literature including time in the switch, via Cullen [67], in order to limit unwanted post-shock dissipation, or second-order velocity derivatives to predict impending compression and "prepare" the integrator for shock onset, as proposed by read Read [68], both of which provide better results for SPH simulations outside of hypersonic external flow and were deemed unnecessary and too complicated for these analyses. For this dissertation, the traditional Balsara switch still had a tendency to provide unwanted viscosity in strong

shear conditions, so it was used to influence the development of a similarly simple, yet novel compression switch was used and is discussed in the Methods chapter.

2.2.3 Other SPH Analyses

Other hard-science applications, outside of astrophysical simulations, have also seen the use of SPH. As recently as 2017, Rodriguez [31] used SPH to model plasma electrode erosion and ablation. Large-scale, subsonic, external flow applications were also studied at length, with applications to accurately model water impacting a sea wall, Liang [30], and subsequent dam breakage, Leroy [36] and Jian [23]. Along this vein, SPH was also used to model soil erosion, Krištof [27], and sediment re-disposition, Fourtakas [69]. These sources are mentioned because most of them include novel boundary conditions implementations that were helpful in advancing the state-of-the-art of SPH.

SPH, through all these developments and improvements, is no longer limited to use by astrophysics and hard-science users. With the growth in computational power, and relatively easy implementation, SPH is seeing use in consumer applications such as video games and computer graphics, as documented by Kalager [70] where near-real time (2-20 frames-per-second) were achieved in a video game application; Tomasi [71] experimented with SPH for in realistic movie computer graphics; and Weaver [72] used SPH to capture bubbles, foaming, and splashing for consumer applications.

2.3 High Performance Computing and SPH

As computers become faster and more capable, CFD researchers have been at the forefront of using the latest technologies and implementations to speed up this computationally-intensive application. In an effort to cull the vast literature within niche field of research, this section will focus on techniques that have been applied to SPH.

SPH is a particularly computationally-intensive CFD method due to the regular nearest-neighbor search algorithm as well as the interpolation of flow parameters between particles and a sizable number of its neighbors [73,74]. Fortunately, it is also well-suited to parallelization because the majority of these calculations are not interdependent and can be accomplished in parallel.

The primary new technique is the use of Graphics Processing Units (GPUs), rather than the computer's Central Processing Unit (CPU) for the substantial number of calculations. GPUs have several thousand stream processors that, while operating at a lower frequency than the CPU, can operate in parallel in an impressive fashion. All of the examples presented in this section use the CUDA® architecture by NVIDIA® corporation [75], due to its immense support network, bundled/provided libraries, and relative ease of implementation [28,72].

One of the most computationally-intensive aspects of any SPH implementation is the k-nearest-neighbor (kNN) search algorithm. This routine, computed roughly every simulation time step, determines the k closest particle neighbors to each particle in the simulation. The neighbor list is usually on the order of 60. kNN algorithms have a

computational complexity on the order of N, more commonly written as O(N), which when applied to every particle in the domain makes the overall complexity $O(N^2)$. Efforts to parallelize this code to run across the thousands of processors present in modern GPUs can dramatically reduce runtimes. For example, Dominguez [73] saw runtimes cut by 56.2 times when going from single-threaded CPU SPH algorithms to optimized GPU implementations and 12.5 time improvements from fully-optimized CPU (8-thread) versions to GPU versions, while Fourtake [69] experienced a similar 58 time improvement between single-thread and GPU implementations. Additionally, Chow [76,77] achieved between 10-18 time improvement (single-thread) and ~4.5 time (16-thread) while solving incompressible flow problems. Finally, Pazouki [32,78] and Hérault [74] were able to demonstrate, if carefully implemented and optimized with proper memory management, SPH runtimes can scale almost-linearly with the number of particles in the simulation, even though the algorithm has a computational complexity $O(N^2)$, due to the ability of parallelization to manage the expanding number of computations.

CHAPTER 3

METHODS

All CFD algorithms numerically solve the fluid dynamics equations. Typically, starting with the Navier-Stokes and mass/momentum conservation equations, in either Eulerian or Lagrangian coordinates, some simplifications are assumed (e.g. neglecting body forces, convection, viscosity, constant specific heat ratio) and these reduced equations are discretized in order to solve numerically. This chapter will present these standard Lagrangian fluid dynamics equations and how they are simplified and implemented for the purposes of this dissertation.

3.1 Equations of Fluid Motion

The first equation of fluid motion is based on the principle of conservation of mass: matter can neither be created nor destroyed, given in differential form as

$$\frac{d\rho}{dt}+\rho(\nabla\cdot\mathbf{u})=0 \tag{3.1}$$

where ρ is density, **u** is the velocity vector, t is time, *d* is material derivative.

Similarly, momentum must remain constant within a system, so the differential form of conservation of momentum is used, given by

$$\frac{d\boldsymbol{u}}{dt} = -\frac{1}{\rho}\nabla p + \frac{1}{\rho}\nabla\cdot\boldsymbol{\tau} \tag{3.2}$$

where p is static pressure, $\boldsymbol{\tau}$ is viscous stress tensor, and $\boldsymbol{\tau}$ expands to

$$\boldsymbol{\tau} = \begin{bmatrix} \tau_{xx} & \tau_{xy} & \tau_{xz} \\ \tau_{yx} & \tau_{yy} & \tau_{yz} \\ \tau_{zx} & \tau_{zy} & \tau_{zz} \end{bmatrix} \tag{3.3}$$

For Newtonian fluids, where the viscous stresses are linearly proportional to the local strain rate (i.e. "shear-thinning"), the symmetry of $\tau_{ij} = \tau_{ji}$ applies, which reduces this from 9 parameters to 6, defined as

$$\tau_{xy} = \tau_{yx} = \mu\left(\frac{\partial v}{\partial x} + \frac{\partial u}{\partial y}\right) \tag{3.4}$$

$$\tau_{yz} = \tau_{zy} = \mu\left(\frac{\partial w}{\partial y} + \frac{\partial v}{\partial z}\right) \tag{3.5}$$

$$\tau_{zx} = \tau_{xz} = \mu\left(\frac{\partial u}{\partial z} + \frac{\partial w}{\partial x}\right) \tag{3.6}$$

$$\tau_{xx} = \lambda(\nabla\cdot\boldsymbol{u}) + 2\mu\frac{\partial u}{\partial x} \tag{3.7}$$

$$\tau_{yy} = \lambda(\nabla\cdot\boldsymbol{u}) + 2\mu\frac{\partial v}{\partial y} \tag{3.8}$$

$$\tau_{zz} = \lambda(\nabla\cdot\boldsymbol{u}) + 2\mu\frac{\partial w}{\partial z} \tag{3.9}$$

The Stokes hypothesis [79] gives the bulk viscosity as

$$\lambda = -\frac{2}{3}\mu \tag{3.10}$$

where μ is the shear viscosity

For a 3D coordinate system (x, y, z), the momentum equation expands to

$$\frac{du}{dt}=\frac{1}{\rho}\left(-\frac{\partial P}{\partial x}+\frac{\partial \tau_{xx}}{\partial x}+\frac{\partial \tau_{yx}}{\partial y}+\frac{\partial \tau_{zx}}{\partial z}\right) \tag{3.11}$$

$$\frac{dv}{dt}=\frac{1}{\rho}\left(-\frac{\partial P}{\partial y}+\frac{\partial \tau_{xy}}{\partial x}+\frac{\partial \tau_{yy}}{\partial y}+\frac{\partial \tau_{zy}}{\partial z}\right) \tag{3.12}$$

$$\frac{dw}{dt}=\frac{1}{\rho}\left(-\frac{\partial P}{\partial z}+\frac{\partial \tau_{xz}}{\partial x}+\frac{\partial \tau_{yz}}{\partial y}+\frac{\partial \tau_{zz}}{\partial z}\right) \tag{3.13}$$

However, if viscous effects are ignored, due to dominance by the density terms, and allowed to be captured solely by the artificial viscosity shock-capturing routine, momentum conservation reduces to

$$\frac{du}{dt}=\frac{1}{\rho}\left(-\frac{\partial P}{\partial x}\right) \tag{3.14}$$

$$\frac{dv}{dt}=\frac{1}{\rho}\left(-\frac{\partial P}{\partial y}\right) \tag{3.15}$$

$$\frac{dw}{dt}=\frac{1}{\rho}\left(-\frac{\partial P}{\partial z}\right) \tag{3.16}$$

Lastly, the conservation of energy, in differential form, is

$$\frac{de}{dt}=-\frac{P}{\rho}\nabla\cdot\mathbf{u}+\frac{\boldsymbol{\tau}}{\rho}\nabla\cdot\mathbf{u}+\frac{1}{\rho}\nabla\cdot(k\nabla T) \tag{3.17}$$

where k is thermal conductivity and T is temperature. Finally, as the particles must move throughout the simulation, particle positions are updated with

$$\frac{d\boldsymbol{r}}{dt}=\boldsymbol{u} \tag{3.18}$$

The following sections describe how these fundamental conservation laws are implemented in SPH, and any simplifications assumed.

3.2 Smoothed Particle Hydrodynamics

SPH is a mesh-free Lagrangian method to solve the mass, momentum, and energy conservation equations in fluid mechanics in which the properties are approximated with kernel integral

$$A_a(\boldsymbol{r}) = \int A(\boldsymbol{r}')\, W(\boldsymbol{r}-\boldsymbol{r}', h)\, d\boldsymbol{r}' \tag{3.19}$$

where A is the parameter to be solved (e.g. density), **r** is the position vector, and W is the interpolation kernel which has 2 properties

$$\int W(\boldsymbol{r}-\boldsymbol{r}', h)\, d\boldsymbol{r}' = 1 \tag{3.20}$$

and

$$\lim_{h\to 0} W(\boldsymbol{r}-\boldsymbol{r}', h) = \delta(\boldsymbol{r}-\boldsymbol{r}') \tag{3.21}$$

where the limit and integral work together to ensure homogeneity between a particle and its closest neighbors as the particle size approaches 0. The integral in Eq. (3.19) is solved over an arbitrary, but constant, number of neighbors to the particle in question—60 in this study. The integral is discretized, in order to derive equations for any flow parameter, as

$$A_a = \sum_b A_b V_b W_{ab}(\boldsymbol{r}_{ab}, h_{ab}) \tag{3.22}$$

where h_{ab} is the difference in local smoothing distance (i.e. $h_a - h_b$), and V is a particle's volume, defined as

$$V = \frac{h^3}{\eta^3} \tag{3.23}$$

where $\eta = 1.11$. The subscript a indicates the particle in question, and subscript b indicates all it neighbors; in essence, this summation is calculated over all the relevant neighbors of particle a, weighted based on W_{ab}, a cubic spline kernel interpolation function, defined as

$$W_{ab} = \begin{cases} \frac{1}{4\pi h_{ab}^3}\left[(2-q)^3 - 4(1-q)^3\right] & for\ 0 \le q \le 1 \\ \frac{1}{4\pi h_{ab}^3}(2-q)^3 & for\ 1 \le q \le 2 \\ 0 & for\ q > 2 \end{cases} \tag{3.24}$$

where q = r/h, the Euclidean distance divided by the local smoothing distance. Gradients can be approximated [63]

$$\nabla A_a = \sum_b A_b V_b \nabla W_{ab}(r_{ab}, h_{ab}) \tag{3.25}$$

The final key to SPH implementation is the balancing of the local smoothing distance, h, with the kernel weighting function, W, which is accomplished via the following, summed over the same 60 neighbors as previous equations

$$\sum_b V_b W_{ab} = 1 \tag{3.26}$$

$$\sum_b V_b \nabla W_{ab} = 0 \tag{3.27}$$

This rest of this section will explain how these discretized equations are used to implement the aforementioned conservation equations.

3.2.1 Equations of Motion as Implemented in SPH

This section will present the equations of motion from Section 3.1 in their discretized form, as solved within SPH. First is the continuity Eq. (3.1), is redefined to compute density directly via

$$\rho_a = \sum_b m_b W_{ab} \tag{3.28}$$

where m is the particle mass and held constant, with the kernel function providing particle volume from the h^3 and q^3 terms, thus strictly enforcing mass conservation ($\rho = m/V$).

Particle position 3.18 is updated with

$$\boldsymbol{r}_{new} = \boldsymbol{r}_{old} + \boldsymbol{u}\, t_s \tag{3.29}$$

where the new position vector, $\mathbf{r}_{new}$, is calculated from the old position times the particle velocity, $\mathbf{u}$, and time step, t_s.

Conservation of momentum, Eq. (3.14-3.16), is achieved via

$$\frac{d\boldsymbol{u}}{dt} = -\sum_b \left(V_a \left(\frac{p_a}{\rho_a} + \frac{p_b}{\rho_b} + \Pi_{ab} \right) \nabla W_{ab} \right) \tag{3.30}$$

where Π_{ab} is the artificial viscosity term, which is discussed at length Section 3.2.3.

Conservation of energy first simplified to

$$\frac{de}{dt} = -\frac{p}{\rho}\nabla \cdot \mathbf{u} \tag{3.31}$$

with viscosity and temperature gradient terms removed due to their minimal impact compared to the velocity term and the fact that the effect will also be captured in the artificial viscosity routine. This simplified equation is implemented as

$$\frac{de}{dt} = -\sum_b \left(V_a \left(\frac{p_a}{\rho_a} + \frac{p_b}{\rho_b} + H_a \right) \boldsymbol{u}_{ab} \nabla W_{ab} \right) \tag{3.32}$$

where H_a is the heating due to artificial viscosity, also discussed in Section 3.2.3.

Finally, in order to fully couple the equations of state, the ideal gas equation is used

$$p_a = \rho_a R T_a \tag{3.33}$$

where R is the specific gas constant of the fluid in question.

3.2.2 Boundary Conditions

For this investigation, boundaries are represented with additional particles placed in the shape of the object being modeled. These boundary particles have a static "flag" set telling the code these particles are not to be treated as fluid particles, which freezes their properties causing them to behave as if they are a wall. Fluid particles approaching these wall particles causes 3 things to happen. First, the fluid particle's velocity is decomposed into parallel and perpendicular components (to the nearest wall particle),

$$\boldsymbol{v}_a = \boldsymbol{v}_{a\|wall} + \boldsymbol{v}_{a\perp wall} \tag{3.34}$$

Then, the particle's parallel component is temporarily copied to the nearest wall particle. This is done just prior to calling the artificial viscosity routine in order to reduce the tendency of the viscosity effects to turn on, as described in the next section. Finally, the fluid particles perpendicular component, if pointing into the wall, is flipped, and the components recombined, defined by

$$\boldsymbol{v}_{a,wall} = \begin{cases} \boldsymbol{v}_{a\|wall} + \boldsymbol{v}_{a\perp wall} & for\ \boldsymbol{v}_{a,fluid} \cdot \boldsymbol{x}_{a,wall} \geq 0 \\ \boldsymbol{v}_{a\|wall} - \boldsymbol{v}_{a\perp wall} & for\ \boldsymbol{v}_{a,fluid} \cdot \boldsymbol{x}_{a,wall} < 0 \end{cases} \tag{3.35}$$

where **x** is the vector from the fluid particle to the nearest wall neighbor. This is shown conceptually in Figure 3.1, and in-situ during a simulation in Figure 3.2. Overall, this novel boundary condition method treats fluid-to-wall interactions as elastic collisions, similar to Newton's surface inclination theory for fluid flows [80].

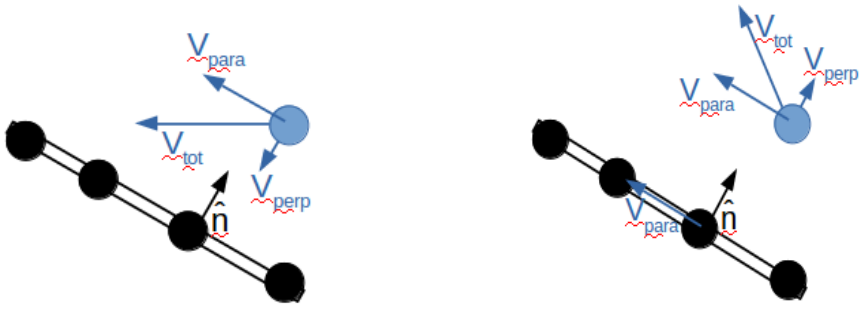

(a) (b)

Figure 3.1: Conceptual depiction of elastic wall interaction with fluid parallel component copied to wall

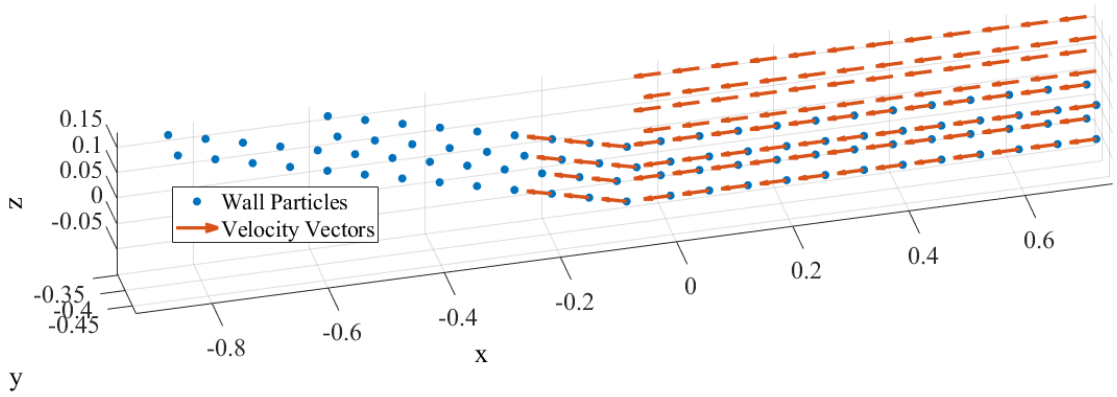

Figure 3.2: Example of boundary conditions during a simulation

3.2.3 Artificial Viscosity and Heating

The basic approach to shock capturing, via artificial viscosity, is intended to provide a deceleration term to particles on collision courses. The idea is for the routine to prevent particle collisions and penetrations in such a way that a second-order approximating deceleration term is added to particles, proportionate to their current distance apart and velocity toward one another, such that they do not collide. If these two particles are on perfect collision courses, most artificial viscosity routines are implemented such that the particles come to a standstill before colliding. However, this perfect collision alignment rarely happens in practice. The routine used in this implementation is a method which will be referred to as the modified Monaghan method, which includes the modifications added in 1992 [63] to the baseline routine first proposed in 1983 [60]. Modified Monaghan [67], is defined by

$$\Pi_{ab} = \begin{cases} \alpha \bar{c}_{ab} \phi_{ab} - \beta \phi_{ab}^2 & \boldsymbol{v}_{ab} \cdot \boldsymbol{x}_{ab} < 0 \\ 0 & otherwise \end{cases} \tag{3.36}$$

where $\alpha = 1$, $\beta = 2$ [51,63], whose terms approximate shear and bulk viscosity, respectively, and is added to the pressure terms in Eq. (3.30). ϕ is defined as

$$\phi_{ab} = \frac{\bar{h}_{ab} \boldsymbol{v}_{ab} \cdot \boldsymbol{x}_{ab}}{|\boldsymbol{x}_{ab}^{2}| + 0.01 h_{ab}^{2}} U_c \tag{3.37}$$

and U_c is the under compression switch [81], in lieu of the typical Balsara switch, and is defined

$$U_c = |\boldsymbol{r}_{ab} + \dot{\boldsymbol{r}}\, dt| < h_{ab} \tag{3.38}$$

This novel switch, combined with the aforementioned fluid velocity parallel components boundary condition, was determined to be most effective at turning off artificial viscosity effects in areas of high-shear (e.g. fluid particles passing over a stationary wall), as well as maintaining the primary goal of artificial viscosity switching to have zero effect outside of the very small shock region, both downstream and upstream. This implementation was able to accurately capture the shock angle and post-shock density, but temperature was too low and pressure was too high. Post-shock temperature was fixed via a technique developed by Noh [82], which is effectively artificial heating due to artificial viscosity, and takes the form of

$$H_a = -\sum_b V_b q_{ab} \frac{e_{ab}}{|x_{ab}|^{2} + 0.001 h_{ab}^{2}} \boldsymbol{x}_{ab} \cdot \nabla \boldsymbol{W}_{ab} \tag{3.39}$$

where e_{ab} is the difference in internal energy between a particle and its neighbors, is added to the energy terms in Eq. (3.32), and q_{ab} is

$$q_{ab} = \alpha h_{ab} \bar{c}_{ab} + \beta h_{ab}^2 \left(\left| V_b \boldsymbol{v}_{ab} \cdot \nabla \boldsymbol{W}_{ab} \right| - V_b \boldsymbol{v}_{ab} \cdot \nabla \boldsymbol{W}_{ab} \right) \tag{3.40}$$

This heating technique, combined with the modified switch for artificial viscosity, allows SPH to adequately match post-shock behavior of all flow parameters: density, temperature, pressure, and the shock angle.

3.2.4 Force and Moment Calculations

Forces and moments are generated by first calculating the pressure at the surface, using a novel, modified form of Eq. (3.22) that only takes into account neighboring fluid particles, defined by

$$P_a = \sum_b P_b V_b W_{ab} K \quad b \notin surface \tag{3.41}$$

where K is a similarly modified kernel scaling function,

$$K = \frac{1}{\sum_b W_{ab} V_b} \quad b \notin surface \tag{3.42}$$

which effectively renormalizes Eq. (3.26) and Eq. (3.27) over only fluid particles. Static particles are not included in the calculations because their properties do not change throughout the simulation and thus would erroneously insert the initial free-stream values into the surface calculation averaging.

Once the pressures are calculated at each surface particle, a force can be determined by an area over which it is applied. These areas are determined a-priori in the generation of the simulation geometry, by appropriately dividing the surface areas among

the surface particles. For highly symmetrical shapes, such as blocks, this is accomplished by simply dividing the total surface area by the number of surface particles. For axi-symmetric shape, such as cones, this is done by calculating an appropriate area based on the radial and axial location of the point. More specifically, the area for each point is calculated by computing the surface area of the conical frusta for each ring of particles and dividing that by the number of particles in that ring.

Now that a force is computed, the direction is calculated via an a-priori defined surface normal, via a novel geometry primitive routine. These surface normals are defined during the geometry generation, prior to the SPH routines, and is computed based on the geometry of the current shape. An example of these normals is shown in Figure 3.3 for a 10° half-angle cone. Similar novel geometry primitive generators for blocks and cylinders were also implemented for this dissertation and examples of which are shown throughout.

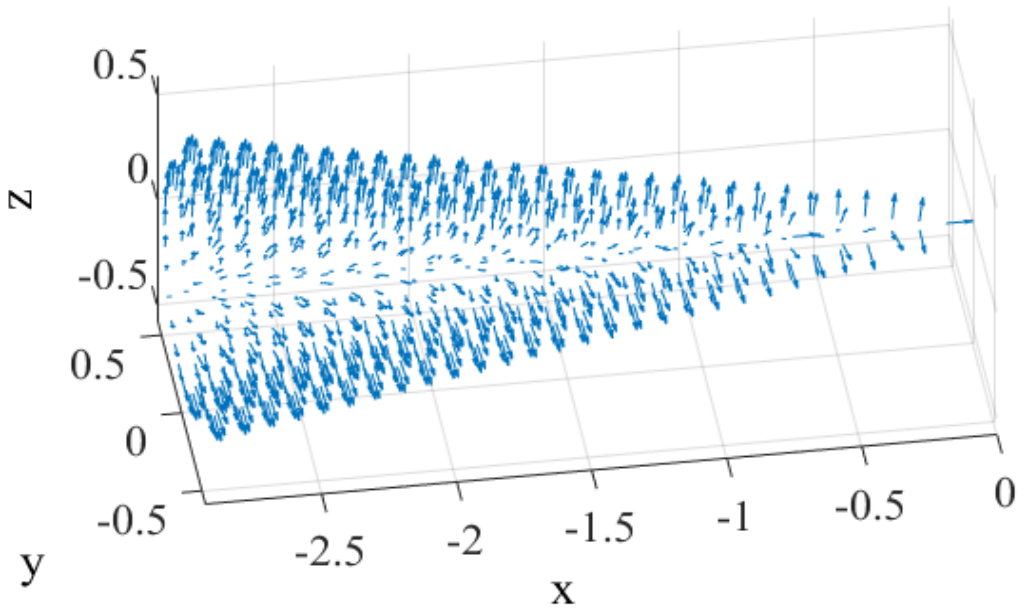

Figure 3.3: Surface normals example for a 10° half-angle cone

At this point total forces can be calculated by

$$\vec{F}_a = P_a S_a \hat{N}_a \tag{3.43}$$

where S_a is the particle's surface area and $\hat{N}_a$ is the surface normal. Moments are similarly calculated with a cross product

$$\vec{M}_a = \vec{F}_a \times \vec{r}_a \tag{3.44}$$

where $\vec{r}_a$ is the vector from the particle to the reference datum. For this dissertation, the nose of the body is used. These are then summed over the body with

$$\vec{F}_{total} = \sum_{surface} \vec{F}_a \tag{3.45}$$

and similarly for the moments via

$$\vec{M}_{total} = \sum_{surface} \vec{M}_a \tag{3.46}$$

Now that all surface and moments have been calculated, the aerodynamic coefficients can be determined. The traditional definitions are used [9], with the lift coefficient given by

$$C_l = \frac{F_l}{\frac{1}{2}\rho V^2 S} \tag{3.47}$$

where S is the total surface area. The drag coefficient defined as

$$C_d = \frac{F_d}{\frac{1}{2}\rho V^2 S} \tag{3.48}$$

and moments given via

$$C_m = \frac{M}{\frac{1}{2}\rho V^2 Sd} \tag{3.49}$$

where d is the characteristic length; for cones it is usually the base diameter. For these analyses, since the shapes are always aligned with the x-axis, with the y-axis into the page as the pitching axis, the drag force is defined as sum of forces in the x direction and lift is defined as the forces in the z direction. The moments are summed about the y-axis.

3.2.5 Vibration Implementation

As mentioned previously, in a particle-based Lagrangian code, the movement of the particles, fluid or boundary, is divorced from any type of simulation construct that otherwise limits movement. This is in contrast to gridded codes—be it finite-difference finite-element, or finite-volume—where the grid must remain stationary throughout the simulation, with the exception of the computationally-complex ALE methods mentioned in Chapter 1. Normally, the equations of motion are solely allowed to handle particle movement, but sometimes the ability to directly move particles is beneficial, and this boundary-moving capability is used for the first time in this research.

As such, moving boundary particles is trivial in SPH. Implementing vibrations on boundary or wall particles requires updating the velocity vector used in Eq. (3.29) to include predefined motion, defined by the derivative of simple harmonic motion position

$$\boldsymbol{u}_{wall} = \boldsymbol{u}_{wall} + 2A_1\pi f_1 \sin(2\pi f_1 t) + 2A_2\pi f_2 \sin(2\pi f_2 t) + \cdots + 2A_n\pi f_n \sin(2\pi f_n t) \tag{3.50}$$

where $\mathbf{u}_{wall}$ are the SPH model-calculated velocity vectors of wall particles, and $\{f_1 \ldots f_n\}$ and $\{A_1 \ldots A_n\}$ are the relevant vibrational frequencies and amplitudes, respectively. This is used to vibrate the CFD model simulation at the same frequencies and magnitudes as the wind tunnel model sting.

For all test cases presented in Section 4.6, the model is vibrated solely in the x-axis direction, as shown in Figure 3.4 for a 5° angle of attack case. A test case where the model was vibrated in angle-of-attack was also performed, with mixed results.

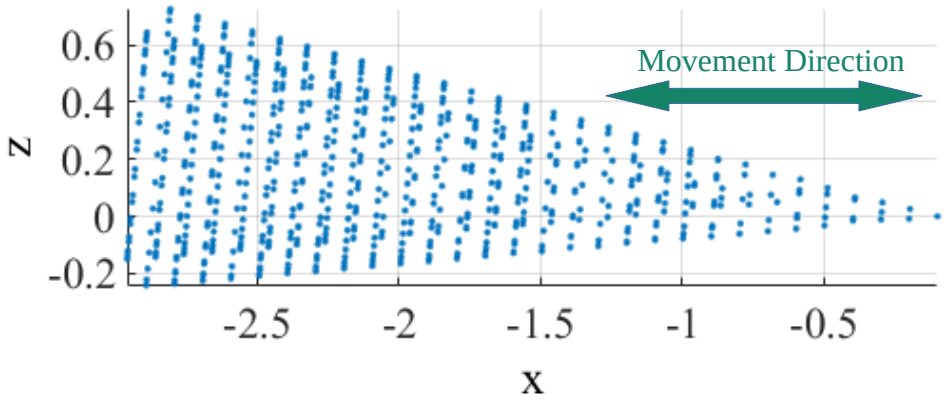

Figure 3.4: Vibration implementation direction for simulations

To vibrate in angle-of-attack, the model was rotated about the point at the nose, with the simple harmonic motion superimposed upon an angular velocity

$$\omega_{wall} = A_1 \sin(2\pi f_1 t) + A_2 \sin(2\pi f_2 t) + \cdots + A_n \sin(2\pi f_n t) \tag{3.51}$$

where the surface normals were rotated via a rotation matrix about the y-axis

$$\hat{\boldsymbol{n}}_{t+1} = \begin{bmatrix} \cos(\omega t) & 0 & \sin(\omega t) \\ 0 & 1 & 0 \\ -\sin(\omega t) & 0 & \cos(\omega t) \end{bmatrix} \hat{\boldsymbol{n}}_t \tag{3.52}$$

where $\hat{\boldsymbol{n}}$ are the surface normals, and the model particle velocity are calculated via

$$\boldsymbol{u}_{wall} = \boldsymbol{\omega} \times \vec{d} \tag{3.53}$$

where $\vec{d}$ is the lever arm (distance) between the particle and the noise point. This motion is shown in Figure 3.5, with the point about which the rotation was performed circled in red.

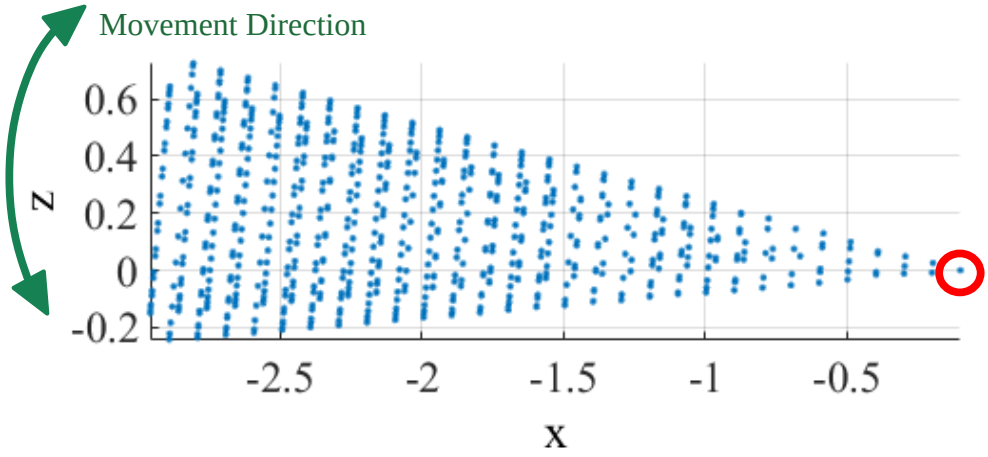

Figure 3.5: Vibration in angle-of-attack, about nose point

3.2.6 Other SPH modifications

The SPH modifications discussed thus far pertain to changes necessary to more accurately model physics-based phenomena, such as modifications to artificial viscosity to more accurately capture shocks in hypersonic flow. This section contains implementation-specific modifications necessary to SPFmax to conduct the necessary simulations for the research. They are included because the strategies may be useful for other SPH implementations.

3.2.6.1 Particle Recycling

In order to simulate the time durations necessary, on the order of 200 ms, while fitting within the memory constraints of the computer used, a novel particle recycling routine was developed. This routine effectively divided up the fluid column into several smaller cylinders (generally 4 or 5) lined up with one another, such that they are physically indistinguishable from a single cylinder (e.g. consistent density, temperature, h-size spacing, etc), as shown in Figure 3.6.

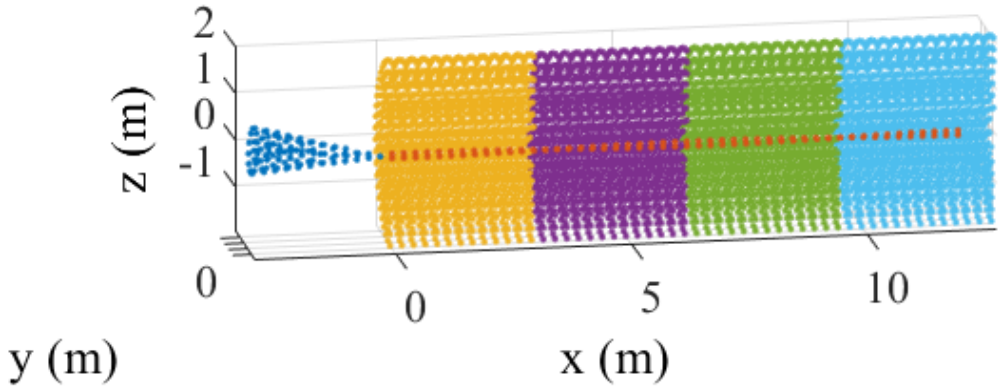

Figure 3.6: Initial setup of particle cycling routine, showing the 4 fluid subcylinders in different colors

Then, as the columns move forward in time, once an entire cylinder's particles have exited the area of interest (i.e. beyond the rear of the test cone), all the particles of that cylinder are collected, the physical properties reset to the initial freestream values, and reassembled into a new cylinder just behind the last trailing fluid cylinder in line. This allows for simulations to effectively be run in perpetuity. This is shown before-and-after in Figure 3.7, with consistent fluid color codes for each subcylinder.

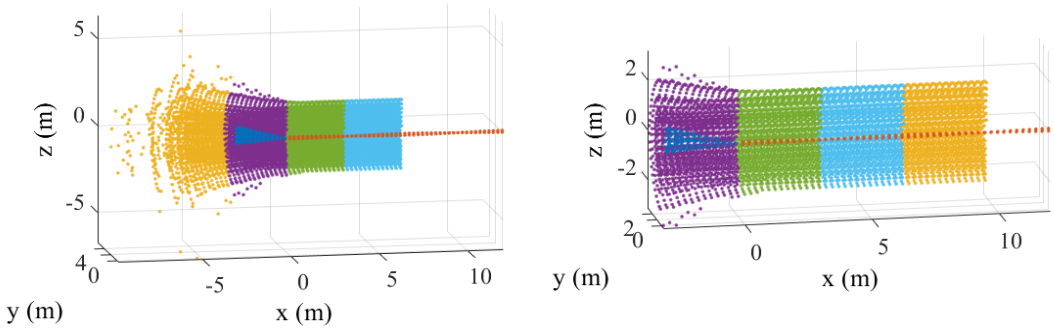

(a) (b)

Figure 3.7: Fluid subcylinders at t = 4.243 ms simulation time, (a) before particle recycling and (b) after

3.2.6.2 Particle Collimation

Another important code enhancement was the ability to freeze the properties of the flow until it entered the test section, effectively leaving the flow collimated until specific criteria were met. Generally, this consisted of maintaining a particle's physical properties until it reached 1 m before the origin, allowing for longer simulations. Without this capability, the fluid cylinder would isentropically expand long before reaching the test model. An example of this phenomena and how it works after the collimation enhancements are shown in Figure 3.8.

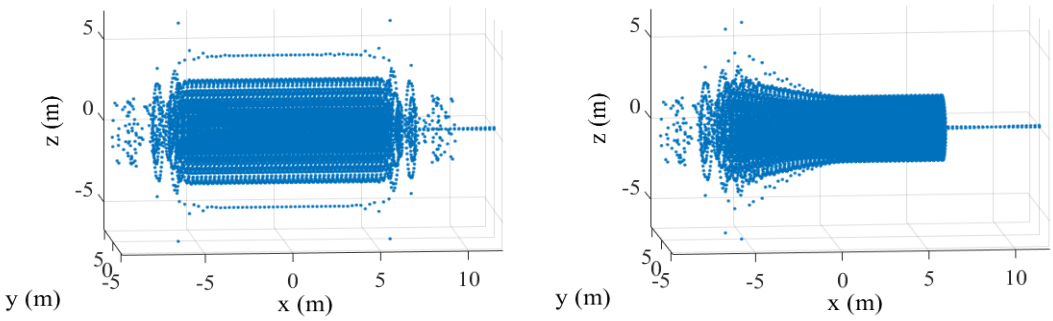

(a) (b)

Figure 3.8: Fluid at t = 4.2 ms, (a) without particle collimation (b) with the collimation routine unfreezing the flow at x < 1 m

3.2.7 Validation Procedure

A building-block approach for verification and validation is used to prove the SPH implementation worked as expected and provided accurate results for hypersonic flow. First, results for a 2D compression corner were simulated with SPH and compared to oblique shock theory, which itself is validated in literature against wind tunnel data [83]. The post-shock parameters compared include: temperature, pressure, density, velocity, Mach, and the shock angle. Second, the same post-shock parameters were compared between SPH and wind tunnel validated Taylor-Maccoll theory [84] for flow over a right circular cone. Finally, with these validations, it is assumed SPH can accurately model high-speed external flow, at which time the model is vibrated according to the sting parameters, with the accelerations of the conical body mimicking real wind tunnel data, implemented via Eq. (3.50). The rest of this section described how the

theoretical data are generated, as well as the methods for which data is captured from SPH.

3.2.7.1 Theoretical Result Generation

For the 2D compression corner, first the shock angle is calculated via the θ-β-M equation

$$\tan(\theta)=2\cot(\beta)\frac{M_1^2\sin^2(\beta)-1}{M_1^2(\gamma+\cos(2\beta))+2} \tag{3.54}$$

where θ is the compression corner angle, γ is the specific heat ratio, M_1 is the free-stream Mach number, and is numerically solved for the shock angle, β, as shown in Figure 3.9.

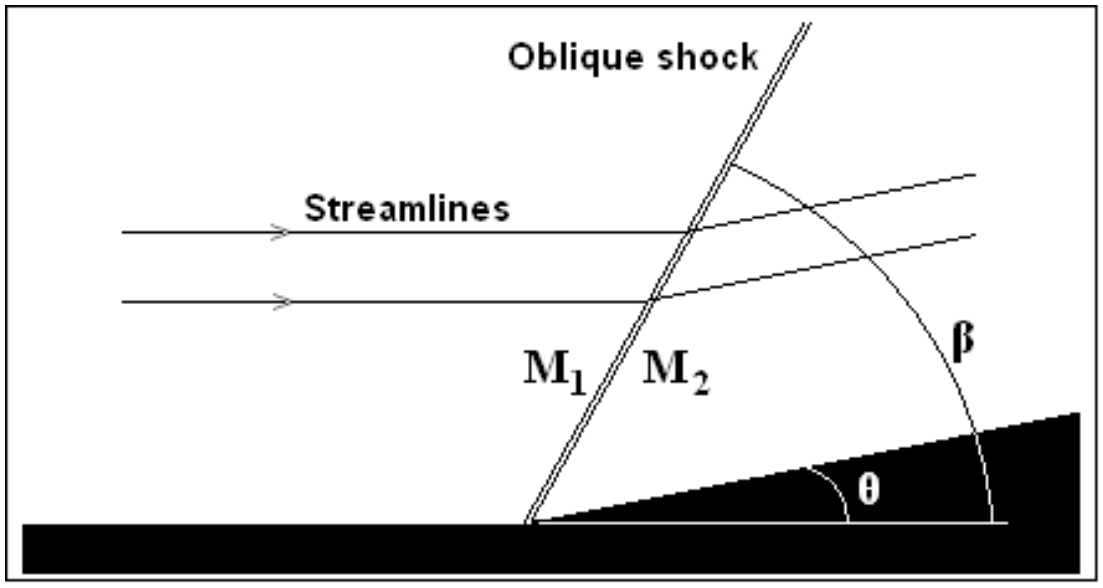

Figure 3.9: θ-β-M diagram [public domain]

To verify the function of the numerical solver, spot checks were conducted against a pre-calculated θ-β-M chart, such as the one shown in Figure 3.10

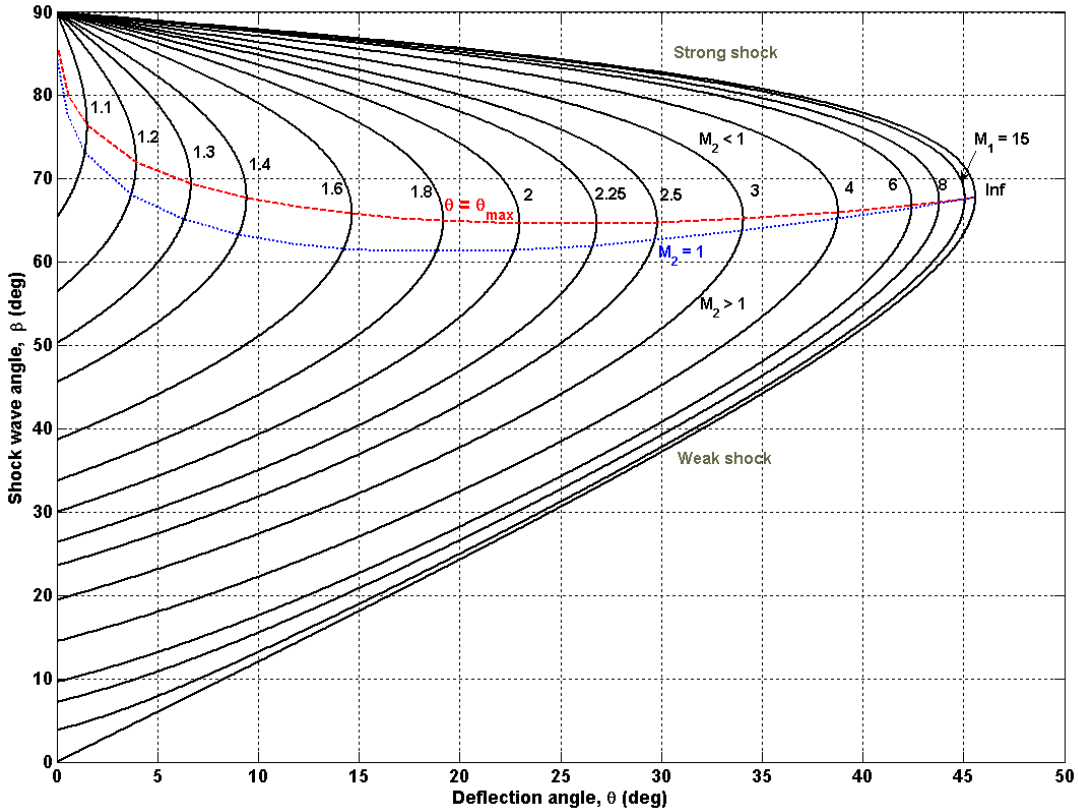

Figure 3.10: θ-β-M Chart [public domain]

Once the shock angle is calculated, the other post-shock parameters are computed with the standard oblique shock relations [83], given by

$$\frac{p_2}{p_1} = 1 + \frac{2\gamma}{\gamma+1}\left(M_1^2 \sin^2(\beta) - 1\right) \tag{3.55}$$

$$\frac{\rho_2}{\rho_1} = \frac{(\gamma+1) M_1^2 \sin^2(\beta)}{(\gamma-1) M_1^2 \sin^2(\beta) + 2} \tag{3.56}$$

$$\frac{T_2}{T_1} = \frac{p_2}{p_1}\frac{\rho_1}{\rho_2} \tag{3.57}$$

$$M_2 = \frac{1}{\sin(\beta-\theta)} \sqrt{\frac{1 + \frac{(\gamma-1)}{2} M_1^2 \sin^2(\beta)}{\gamma M_1^2 \sin^2(\beta) - \frac{(\gamma-1)}{2}}} \tag{3.58}$$

where a subscript 2 indicates the post-shock value, and a subscript 1 indicates the free-stream (pre-shock) value.

Verification and validation is then extended to axisymmetric flow over right circular cones. This is not as simple as the 2D case because no closed-from solutions exist for this type of flow. Instead, numerical solutions to calculate the shock angle are used, specifically to solve the Taylor-Maccoll equation [85]

$$\frac{\gamma-1}{2}\left[V_{max}^2-V_r^2-\left(\frac{dV_r}{d\theta}\right)^2\right]\left[2V_r+\frac{dV_r}{d\theta}\cot(\theta)+\frac{d^2V_r}{d\theta^2}\right] - \frac{dV_r}{d\theta}\left[V_r\frac{dV_r}{d\theta}+\frac{dV_r}{d\theta}\left(\frac{d^2V_r}{d\theta^2}\right)\right]=0 \tag{3.59}$$

where V_r is radial velocity (along a ray from the vertex, as shown in Figure 3.11), and θ is the independent variable representing local deflection angle. Once the shock angle, θ_s, is determined, the other post-shock flow properties are calculated as above, with Eq. (3.55-3.58).

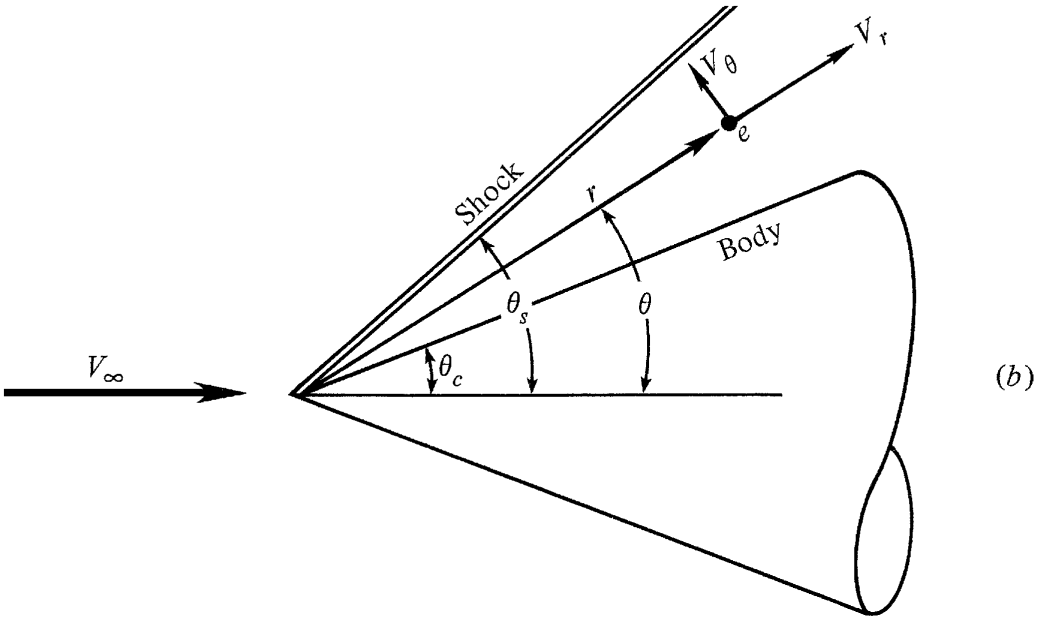

Figure 3.11: Cylindrical Coordinates for Taylor-Maccoll equation [98]

Similar to the θ-β-M relations above, the Taylor-Maccoll equation is solved and graphed, shown in Figure 3.12 as the θ_s-θ_c-M relation, where θ_s is the shock angle and θ_c is the cone angle. This plot is used to spot-check the numerical algorithm used to calculate the shock angles for cones used in this study.

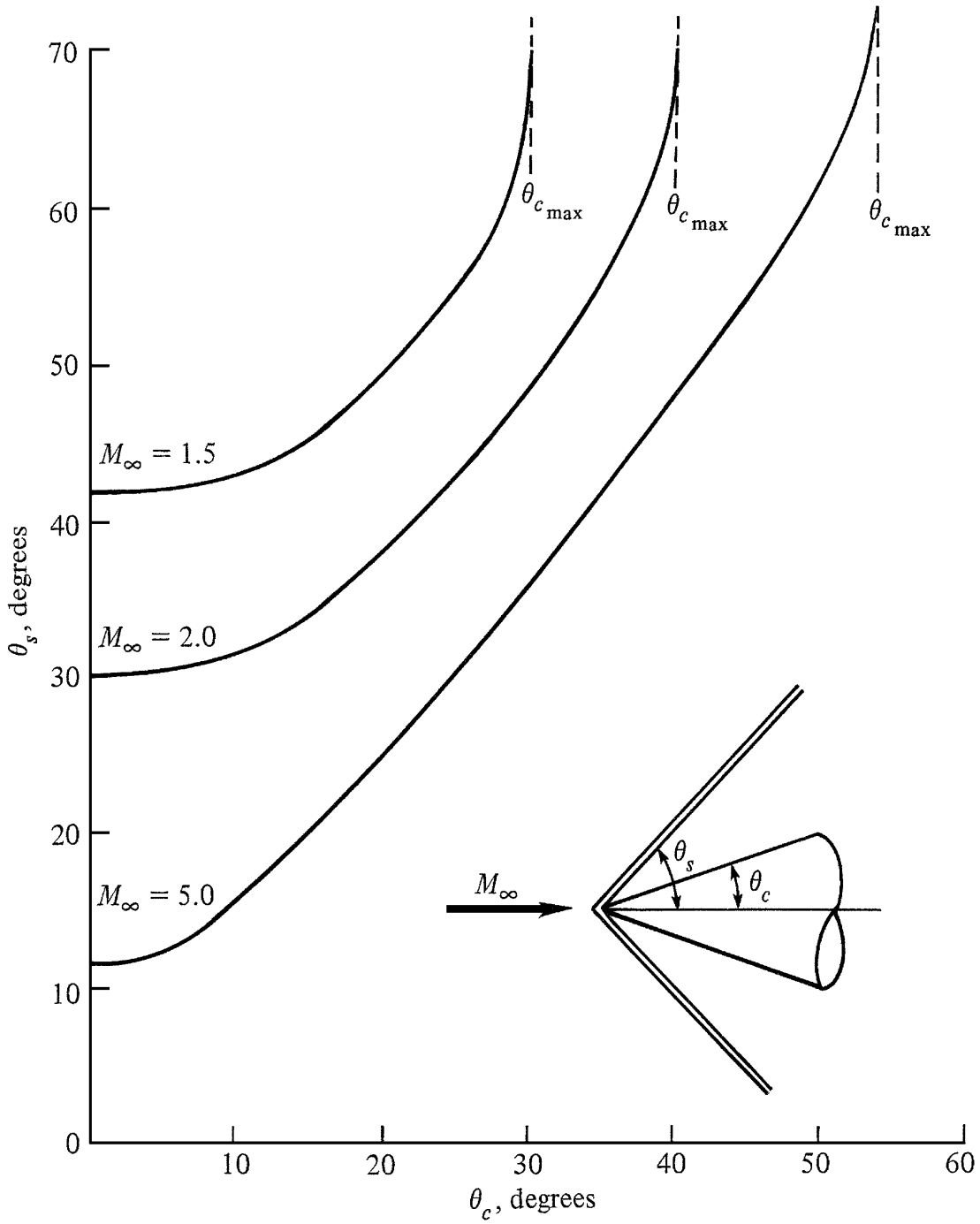

Figure 3.12: θ_s-θ_c-M for cones [98]

Once the right circular cone flow is proven accurate, then vibrations were implemented according to Section 3.2.4 to match the sting characteristics as necessary.

3.2.7.2 SPH Data Capture Methodology

The post-shock flow parameters (temperature, pressure, density, velocity, and Mach) were calculated by finding the peak temperature location along a data slice perpendicular to the x-axis (in the y-z plane), at an x-location corresponding to the more-aft distance used in the shock angle calculations described below, typically in the middle-to-aft third of the body and is shown by the arrows in Figure 3.13. This location is the radial distance from the x-axis at which the post-shock temperature peaks, effectively marking the back-side of the shock. Data at this point is integrated and averaged over as long a time span as possible based on the flow conditions, typically a minimum of 10 time-steps, or ~1.5 ms, with 20 time-steps preferred (~2.5 ms). The data frames used for averaging is determined by 2 factors: first, when the flow reaches that point along the x-axis, usually within the first 15-20 time-steps; second, when the ambient temperature and pressure start to fall due to the isentropic expansion along the top of the air column.

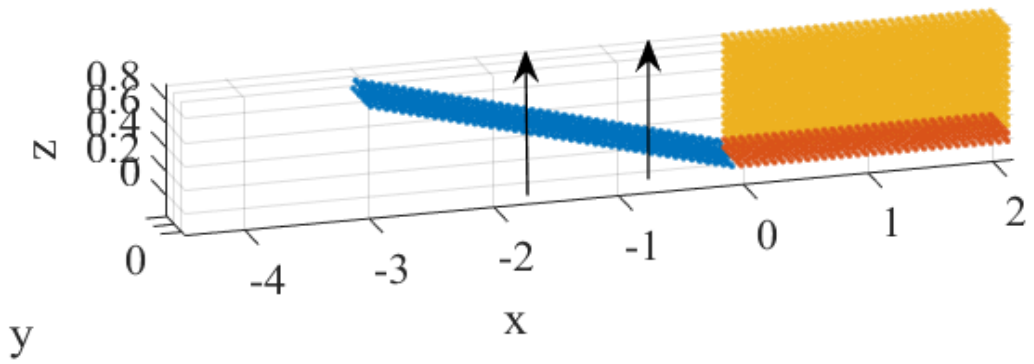

Figure 3.13: Example of 10° compression corner data slice direction and location

The sensitivity to location is minimal for these post-shock parameters as long as the data selection is a) located outside the front 0.5 m of the body, minimizing noise and turbulence, and b) values are averaged over as long a timespan as possible (as explained above).

Shock angle is calculated by determining the onset of the temperature jump condition due to the shock at 2 locations along the x-axis—for cones, it also happens to be along the longitudinal axis. These 2 points are as far aft as practicable while maintaining consistency with other test cases, with enough separation to effectively calculate the angle—0.5 m minimum separation, with 1.0 m preferred. For example, on long and slender cones (e.g. 5° half-angle), these points were x = {-2.0, -1.0}, while on short and blunt cones (e.g. 22.5° half-angle), these points were x = {-1.25, -0.75}.

Measurements near the front of the body were avoided as it was determined the shock onset data is excessively noisy within the first ~0.5 m; likely due to the flow transition from pure shear to inclined along the body, thus causing excessive turbulence, as well as the particle h-size being larger than the flow parameters require for such measurement.

The temperature jump condition is determined as follows: using the calculated post-shock temperature from above, the ambient temperature is subtracted (288 K in the validation cases), multiplied by 10%, then added back to the ambient temperature. This new value is defined as the jump condition onset, T_{onset}, and is effectively where the flow temperature climbs 10% above ambient on its way to the peak, post-shock temperature. This value is found along the same data slice cut in the y-z plane to find the radial distance at which the shock onset occurs at that x-location along the body, with an example shown in Figure 3.14 where $T_{onset} = 302.6$ K, giving a T_{onset} radius of 0.38 m. Finally, the inverse tangent of these radii calculated at 2 different x-locations is the shock angle.

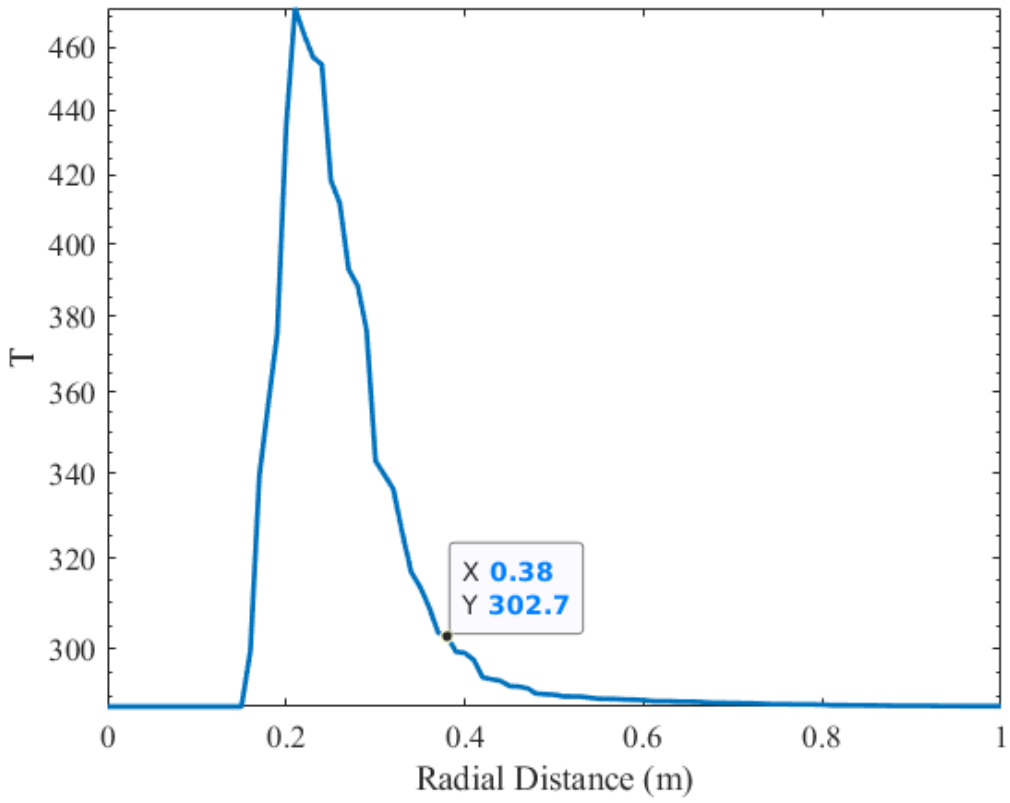

Figure 3.14: Example T_{onset} location at x = -0.75 m for 10° compression corner

The shock-angle capturing is the most sensitive to the locations selected along the x-axis of the body, with further aft locations being preferable. This is due to the data granularity (roughly corresponding to the h-size at flow deflection), making measurement difficult near the front of the body. For example, if the 10%-above-ambient peak is measured near the nose of a cone, this may occur at a radial distance between 0.18 m and 0.22 m. This combined with a similar ambiguity near the middle of the cone (e.g. 0.32 m and 0.36 m) can lead to vastly different calculations of shock angle (a minimum of 5.7° to a maximum of 10.2°—error margins exceeding 4.5°), mostly attributable to interpolation

errors. Conversely, if measurements are taken further aft along the same cone, where these radial distances are between {0.52 m, 0.56 m} and {0.24 m, 0.28 m}, the error margins are reduced to less than 3.2°, with further reductions possible with careful interpolation. Also, the data is overall less noisy further aft (with temperatures peaking over shorter radial distances), making the interpolation between these bracketed onset radii easier to calculate, thus reducing the error margin to further.

The results presented in Chapter 4 will delve deeper into the locations chosen and the calculations thereof.

CHAPTER 4

RESULTS

This chapter will present the results of the aforementioned building-block approach to verification and validation of SPH simulating hypersonic flow, as well as the fundamental changes in flow that occur due to model vibrations. Generally, with exceptions outlined where necessary, the goal is to match theoretical or measured data within 10%. Any assumptions made concerning a set of simulations is outlined, as well as any known sources of error within the data. The specific implementation of SPH used in this study is called SPFmax [86], a software package written in MATLAB in active development by the UAH's Propulsion Research Center. SPFmax has seen use in a wide array of applications, including fusion propulsion [87] and plasma rail guns [88], both of which require accurate, high-speed shock-capturing capabilities. As discussed in Chapter 3, modifications were implemented in SPFmax as part of this dissertation to generate these results.

4.1 2D Flat Plate Results and Validation

This section presents the verification and validation of SPH simulating hypersonic flow into a compression corner, a 2D test case. Figure 4.1 shows the layout for all simulations, with 3 main components: the fluid 'block' (yellow); a bottom plate (red) to prevent the air from isentropically expanding downward; and the flat plate itself (blue), at an angle of incidence, θ. The initial particle spacing, h, is 0.066 m arbitrarily chosen to maintain a reasonable number of particles within the simulation while providing a small initial local smoothing distance. The fluid block is 10 m long, 2 m tall, and 1 m wide, with 74,896 particles. The bottom plate 10 m long, 2 particles tall/thick (i.e. 0.066 m), and 1 m wide, with 4,832 particles. The flat plate has the same width and thickness as the bottom plate, is 3 m long, with a total of 1,472 particles, giving the simulation a grand total of 81,200 particles. The flat and bottom plates are 2 particles thick in order to prevent fluid particle penetration. To maintain consistency, these dimensions and particle counts are used throughout the compression corner test cases, with the angle of incidence as the independent variable. For all runs, the initial freestream temperature is 288 K and density is 0.02 kg/m^3, and via the ideal gas law, a freestream pressure of 1653.1 Pa for the air cases and 1088.2 Pa for the CO_2 case, roughly simulating flight at 25 km altitude.

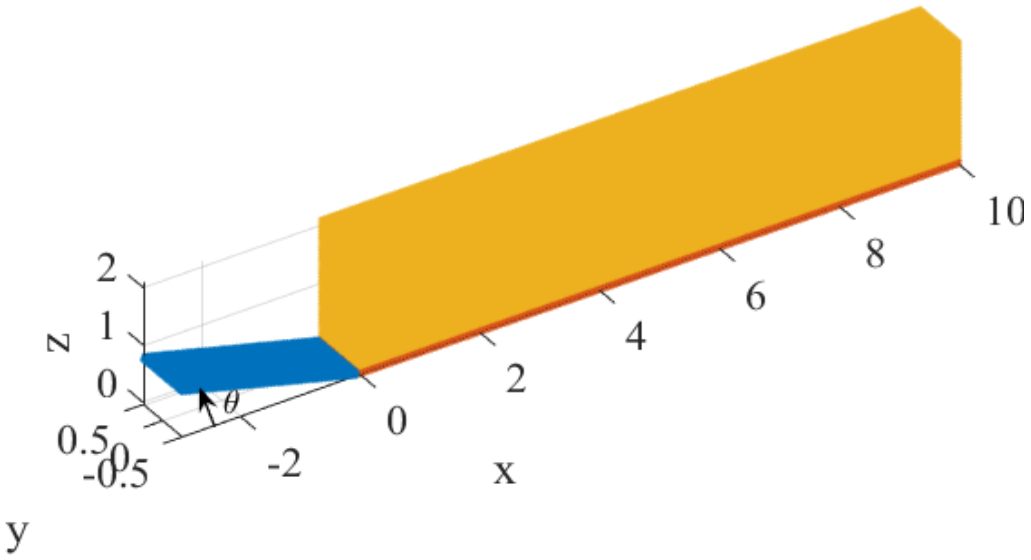

Figure 4.1: Initial compression corner V&V configuration (15° shown)

The test cases are in Table 4.1, with the primary verification objective being Mach 5 air, with 2 additional stretch test cases: supersonic air at Mach 2, to evaluate SPH with lower-speed supersonic flow; and hypersonic CO_2 with its differing specific heat ratio, $\gamma = 1.3$, which would be applicable in Martian atmospheric analyses.

Table 4.1: Compression corner test cases

Fluid	Mach	Angle of Incidence (θ)	Run #
Air	2	10°	1
	5	10°	2
		15°	3
		20°	4
		25°	5
		30°	6
CO_2		20°	7

The post-shock properties for Mach 5 air are presented in Table 4.2. Properties remain within the 10% threshold defined earlier until the angle of incidence reaches 30° at which point pressure and density are predicted too high; by 16.7% and 15.78%, respectively. This error growth at such a high incidence angle is considered inconsequential as it is not expected for any hypersonic vehicle to fly at such angles attack—even then, temperature is predicted within 1%, so for applications such as thermal protection design, there is no such incidence angle limit. General trends show SPH predicts post-shock temperature and pressure higher than their theoretical values, while shock angle remains low, and density, velocity, and Mach have no evident trend.

Table 4.2: Downstream results for air at Mach = 5

Run #	Compression angle	Temp (K)	Pressure (Pa)	Density (kg/m^3)	Velocity (m/s)	Mach	Shock Angle	
2	10°	432.87	5,130.63	0.0414	1,631.29	3.92	18.26°	SPFmax
		411.00	5,031.00	0.0426	1,626.00	4.00	19.37°	Theory
		5.32%	1.98%	2.87%	0.33%	2.05%	5.73%	% error
3	15°	501.09	8,290.21	0.0578	1,570.43	3.51	22.05°	SPFmax
		500.05	7,903.00	0.0551	1,571.00	3.50	24.32°	Theory
		0.21%	4.90%	4.99%	0.04%	0.06%	9.33%	% error
4	20°	620.13	12,067.38	0.0683	1,544.70	3.10	27.47°	SPFmax
		611.00	11,633.00	0.0663	1,498.00	3.02	29.8°	Theory
		1.49%	3.73%	2.97%	3.12%	2.58%	7.82%	% error
5	25°	769.22	16,679.72	0.0755	1,372.09	2.47	32.6°	SPFmax
		745.89	16206	0.0757	1,405.0	2.57	35.78°	Theory
		3.13%	2.92%	0.22%	2.34%	3.73%	8.89%	% error
6	30°	910.78	25,206.94	0.0964	1,163.16	1.93	37.23°	SPFmax
		903.00	21,600.00	0.0833	1,287.00	2.14	42.34°	Theory
		0.86%	16.70%	15.78%	9.62%	9.77%	12.1%	% error

Verification results for supersonic (Mach = 2) air are shown in Table 4.3. Again, the results agree within 10% of oblique shock theory. Interestingly, the overall trend is reversed from the hypersonic flow—namely, temperature and pressure are predicted low, while the shock angle is predicted 2.7% higher than oblique shock theory would prescribe. With only one angle of incidence simulated, no trends can be stated for density, velocity, and Mach.

Table 4.3: Results for air at Mach = 2

Run #	Compression angle	Temp (K)	Pressure (Pa)	Density (kg/m^3)	Velocity (m/s)	Mach	Shock Angle	
1	10°	314.23	2,724.33	0.0302	614.76	1.73	40.36°	SPFmax
		337.00	2,821.00	0.0292	603.60	1.64	39.3°	Theory
		6.76%	3.43%	3.45%	1.85%	5.5%	2.70%	% error

Finally, the results of hypersonic (M = 5) Carbon Dioxide are displayed in Table 4.4. Again, the results are within 10% of their predicted values, with the same trends from hypersonic air emerging—temperature and pressure estimated slight higher than their theoretical values by 2.82% and 1.41%, respectively, with shock angle estimated 4.45% lower. As with the supersonic case, with only one angle of incidence simulated, no trend conclusions can be drawn for density, velocity, and Mach.

Table 4.4: Results for CO_2 at Mach = 5

Run #	Compression angle	Temp (K)	Pressure (Pa)	Density (kg/m^3)	Velocity (m/s)	Mach	Shock Angle	
7	20°	532.91	7,074.07	0.0706	1,205.83	3.34	27.47°	SPFmax
		518.30	6,976.00	0.0712	1,179.00	3.31	28.75°	Theory
		2.82%	1.41%	0.81%	2.28%	0.96%	4.45%	% error

The detailed data from which Tables 4.2-4.4 are generated are presented in Table 4.5. This includes the calculated T_{onset}, as described in Chapter 3, and the radial distance (T_{z1}, T_{z2}) this temperature is reached at each of the x-axis locations (x_1, x_2). For example, the shock angle for Run #3 is calculated via

$$\beta = \arctan\left(\frac{T_{z1} - T_{z2}}{x_1 - x_2}\right) = \arctan\left(\frac{0.835 - 0.43}{-1.75 + 0.75}\right) = 22.05^{\circ} \tag{4.1}$$

which is the value shown in Table 4.2. The value z_1 is the point at which the maximum temperature is achieved at x_1, and is the point at which the other properties are taken, averaged over the time steps given, ts_1 through ts_2. Figure 4.2 shows this graphically, for the 15° corner case, with only the inclined portion of the compression corner plotted with the points used for calculating the post-shock properties. Figure 4.3 shows, for the 10° compression corner, how the radial T_{onset} distances, T_{z1} and T_{z2}, are computed at x_1 (left) and x_2 (right). Figure 4.4 shows the simulation at t = 3 ms, with the shock forming and the isentropic expansion at the top of the air block.

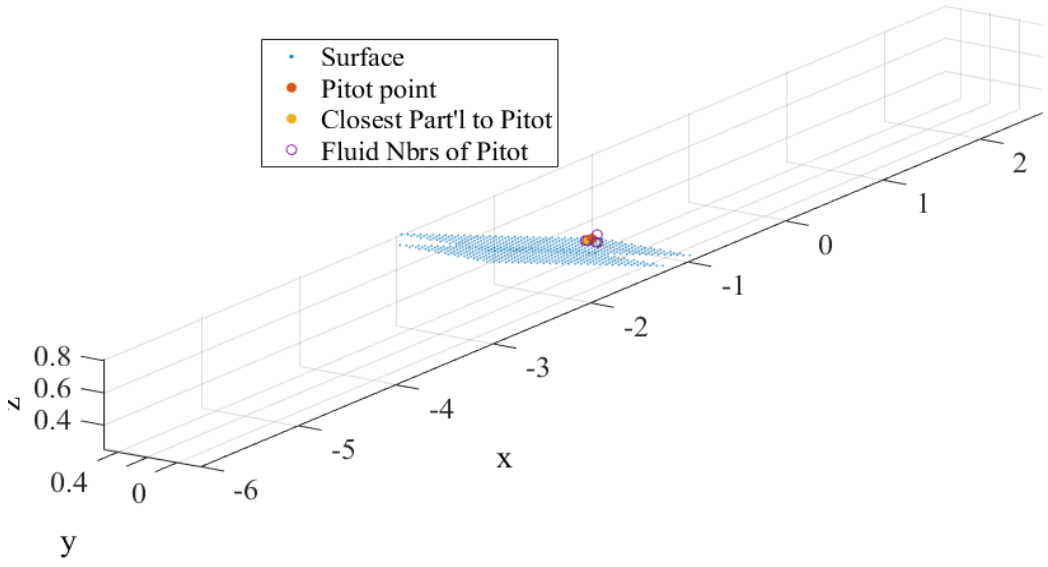

Figure 4.2: Measurement points for 15° compression angle

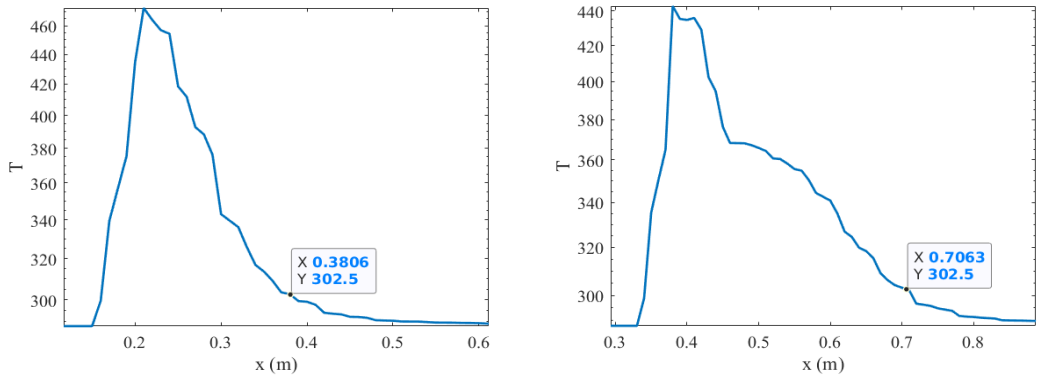

(a) (b)

Figure 4.3: 10° corner T_{onset} and shock angle calculation

Table 4.5: Detailed data for compression corner cases

Fluid	Mach	Compression Angle	T_{onset} (K)	T_{z1}/T_{z2} (m)	x_1/x_2 (m)	z_1 (m)	ts_1, ts_2
Air	2	10°	290.6	1.17	-1.25	0.7	20, 25
				0.75	-0.75		
	5	10°	302.5	0.71	-1.75	0.42	20, 40
				0.38	-0.75		
		15°	309.3	0.835	-1.75	0.56	
				0.43	-0.75		
		20°	321.2	0.99	-1.75	0.7	
				0.47	-0.75		
		25°	336.1	1.055	-1.5	0.72	
				0.415	-0.5		
		30°	350.3	1.29	-1.5	0.92	
				0.53	-0.5		
CO_2		20°	312.5	0.985	-1.75	0.7	
				0.465	-0.75		

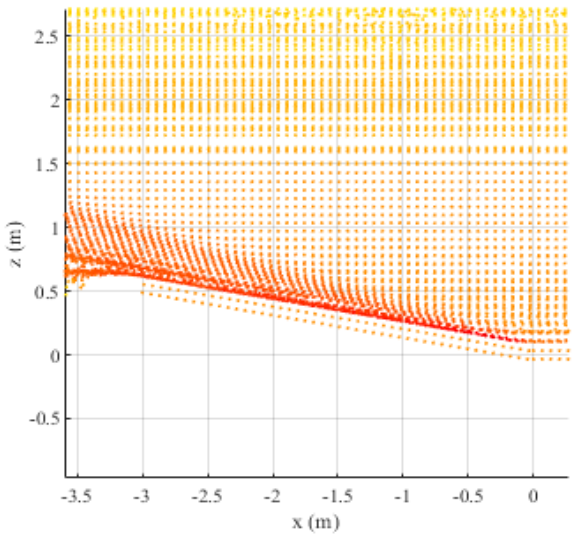

Figure 4.4: 10° case at t = 3 ms

4.2 Right Cylindrical Cone Results and Validation

Validation is then extended to axisymmetric flow over right circular cones. Figure 4.5 shows the setup for a 15° cone, with all others being similar save the cone half-angle. Similar to the compression corner cases, there are 3 main components: the fluid cylinder (yellow), shown here cut in half for visibility; a shear cylinder (red), to prevent the fluid cylinder from expanding inward and its particles perfectly impacting the cone point and creating stand-off shocks, and the cone itself (blue). The initial local smoothing distance is 0.1 m, again chosen somewhat arbitrarily to keep a tight particle

spacing within a reasonable number of particles. The fluid is 2 m in diameter, 8 m long, with 106,353 particles. The shear cylinder is 0.1 m in diameter (1 h-size) and also 8 m long, with 324 particles. In all cases, the cone has a base diameter of 1 m, which means the length will differ according to the half-angle. In the 15° case pictured, the cone is 1.866 m long, with 524 points, giving the simulation a grand total of 107,201 particles. This number is the product of the initial h-size spacing as previously mentioned maintained consistently across the item dimensions and provides for reasonable results with the computing resources available. Section 4.3 discusses the role in which the number of particles affects the results and their accuracy.

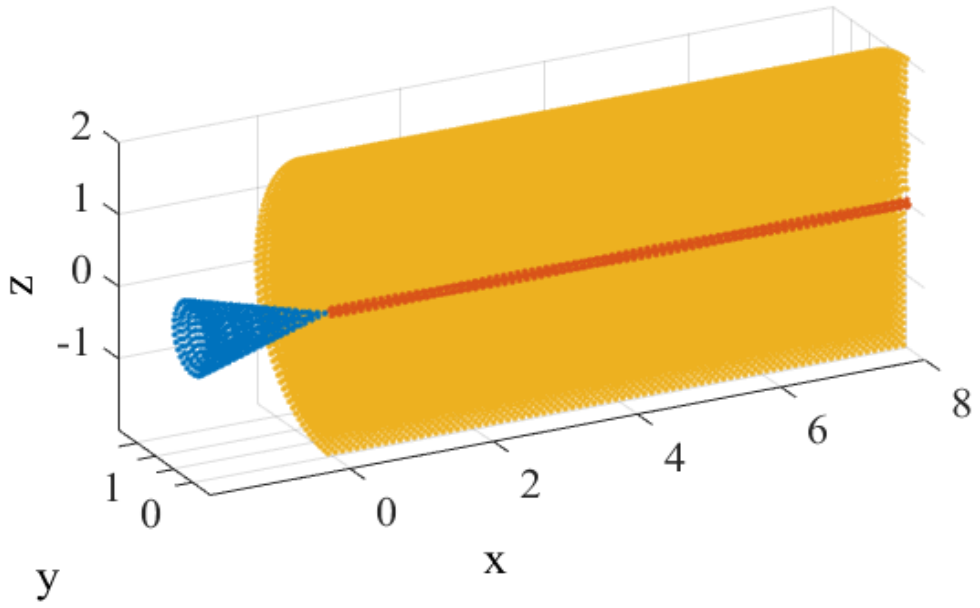

Figure 4.5: Initial configuration for cone validation (15° shown)

The measurement of cone half-angle is shown in Figure 4.6; zoomed in on the same 15° case from Figure 4.5.

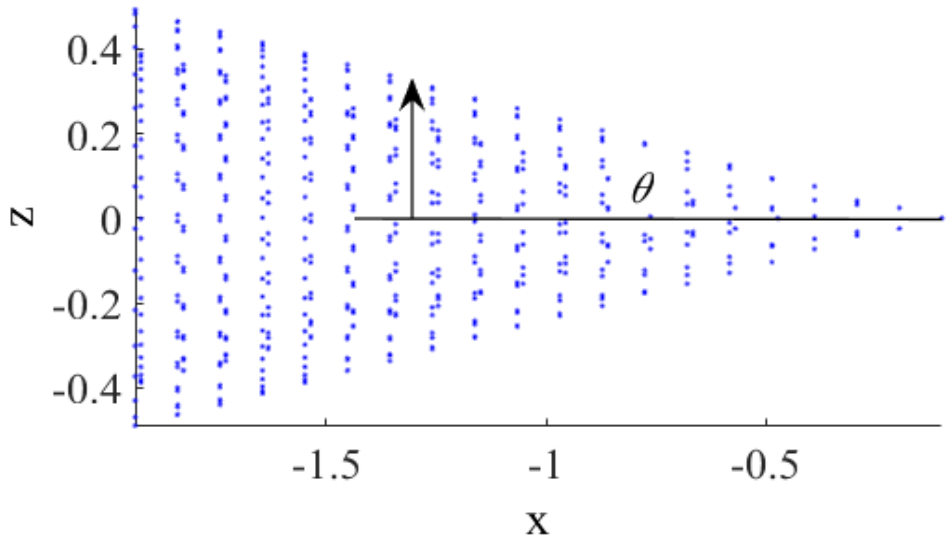

Figure 4.6: Cone half-angle diagram, 15° shown

Table 4.6 shows the test cases modeled, with the validation focusing on air at Mach 5, with more test cases than for 2D flow as the vibrations would later be applied to similar geometries. The same 2 additional stretch cases were carried over from the compression corner validation: air at Mach 2 to see if the lower-speed validation is maintained in 3D, and CO_2 at Mach 5 with its different specific heat ratio.

Table 4.6: 3D Cone validation test cases

Fluid	Mach	Cone half-angle	Run #
Air	2	10°	8
	5	5°	9
		6°	10
		7°	11
		8°	12
		9°	13
		10°	14
		15°	15
		20°	16
		25°	17
CO_2		20°	18

The resulting cone lengths, cone particles, and total particle counts for the simulations are in Table 4.7. The number of particles in the cone varies due to the varying length—the base diameter is constant at 1 m.

Table 4.7: Cone validation particle counts

Run #	Cone half-angle	# Cone particles	Cone Length (m)	# Fluid particles	# Shear cylinder particles	# Particles Total
8, 14	10°	775	2.836	106,353	324	107,452
9	5°	1,525	5.715			108,202
10	6°	1,270	4.757			107,947
11	7°	1,102	4.072			107,779
12	8°	935	3.558			107,612
13	9°	823	3.157			107,500
15	15°	524	1.866			107,201
16, 18	20°	383	1.374			107,060
17	25°	305	1.072			106,982

Similar to Figure 4.2, Figure 4.7 shows, for run number 14, the typical point layout used to capture the post-shock properties.

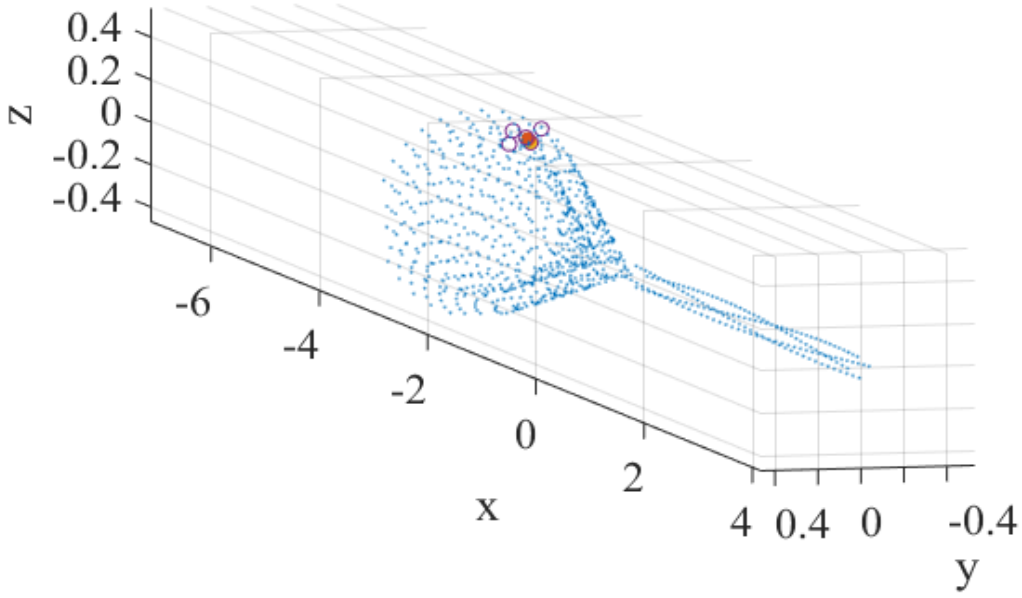

Figure 4.7: Measurement points for 10° cone

Figure 4.8 shows the particles of interest during a simulation for a 15° cone, both in their initial positions and at t = 2.31 ms, with the cone in blue and the air in red. The displacement of the air at the resulting shock angle are apparent.

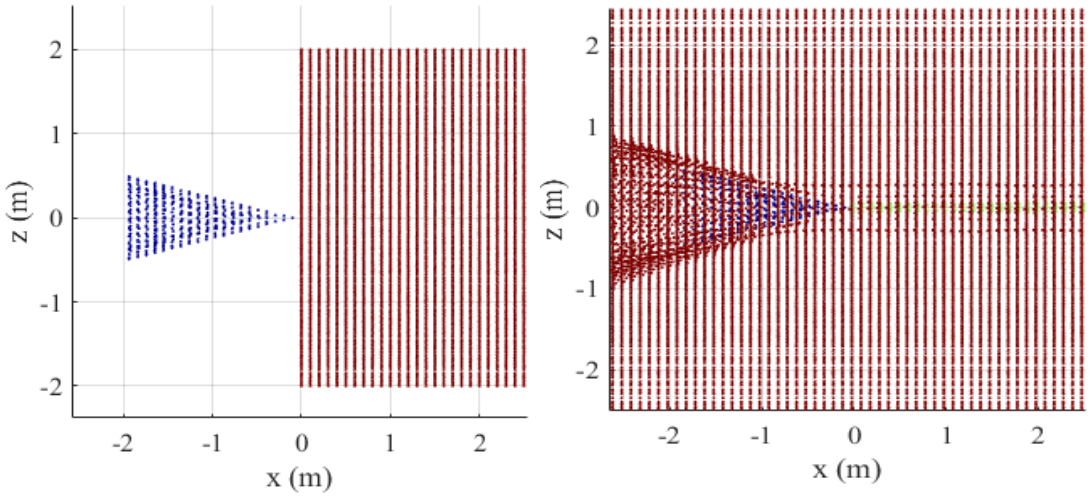

(a) (b)

Figure 4.8: 15° cone at (a) t = 0 and (b) t = 2.31 ms

The results for air at Mach 5 are presented in Table 4.8. The results are within 5% of those predicted by Taylor-Maccoll numerical method, with the exception of the shock angle in run number 9, the 5° half-angle case, where the error is approximately 1° (8%). The increased error is likely due to how shock angle is calculated with SPFmax, as noted in Chapter 3, and the difficulty in resolving the T_{onset} radial length, rather than the simulation itself. Unlike the flat plate test cases, fewer obvious trends emerge within the data. Temperature is predicted slight low, except for run number 15; velocity and Mach are predicted lower except for run number 9; pressure and density are predicted high about half the time; and shock angle is usually predicted low except for run number 14.

Table 4.8: 3D Flow over cone results, Air @ Mach 5

Run #	Cone half-angle	Temp (K)	Pressure (Pa)	Density (kg/m^3)	Velocity (m/s)	Mach	Shock Angle	
9	5°	303.48	2,305.81	0.0265	1,698.18	4.86	11.3°	SPFmax
		317.3	2,317.8	0.0254	1,683.68	4.72	12.29°	Taylor-Maccoll
		4.35%	0.52%	4.26%	0.86%	3.14%	8.06%	% error
14	10°	364.84	3,845.91	0.0366	1,627.05	4.26	16.17°	SPFmax
		368.9	3,815.6	0.0361	1,652.41	4.29	15.61°	Taylor-Maccoll
		1.10%	0.79%	1.35%	1.53%	0.84%	3.59%	% error
15	15°	448.31	6,133.72	0.0471	1,545.66	3.67	19.8°	SPFmax
		438.31	6,114.7	0.0486	1,609.81	3.84	20.02°	Taylor-Maccoll
		2.28%	0.31%	3.19%	3.99%	4.34%	1.10%	% error
16	20°	518.59	8,975.14	0.0589	1,487.33	3.29	23.75°	SPFmax
		527.1	9,185.9	0.0607	1,553.19	3.38	24.94°	Taylor-Maccoll
		1.61%	2.29%	3.02%	4.24%	2.43%	4.77%	% error
17	25°	616.87	13,088.16	0.0709	1,402.03	2.86	30.11°	SPFmax
		634.49	12,964	0.0712	1,482.43	2.94	30.16°	Taylor-Maccoll
		2.78%	0.96%	0.45%	5.42%	2.47%	0.17%	% error

Considering the brunt of this dissertation focuses on right circular cones, more granular test cases, varied by only 1° in half-angle, were also run in order to better verify 3D flow. These results are presented in Table 4.9, and again, the errors remain within 5% of the Taylor-Maccoll-predicted values—well within the 10% threshold defined earlier. Similarly, few trends emerge, except density is reliably predicted high and temperature is predicted low. Post-shock pressure, velocity, shock angle, and Mach have no obvious trends.

Table 4.9: Axisymmetric flow over cone, more detail, Air @ Mach = 5

Run #	Cone half-angle	Temp (K)	Pressure (Pa)	Density (kg/m^3)	Velocity (m/s)	Mach	Shock Angle	
9	5°	303.48	2,305.81	0.0265	1,698.18	4.86	11.3°	SPFmax
		317.3	2,317.8	0.0254	1,683.68	4.72	12.29°	Taylor-Maccoll
		4.35%	0.52%	4.26%	0.86%	3.14%	8.06%	% error
10	6°	314.04	2,538.34	0.0282	1,687.34	4.75	12.4°	SPFmax
		326.3	2,554.9	0.0273	1,678.14	4.63	12.8°	Taylor-Maccoll
		3.76%	0.65%	3.15%	0.55%	2.51%	3.13%	% error
11	7°	329.24	2,836.64	0.030	1,664.58	4.58	14°	SPFmax
		335.9	2,820.3	0.0292	1,672.24	4.55	13.4°	Taylor-Maccoll
		1.98%	0.58%	2.69%	0.46%	0.58%	4.48%	% error
12	8°	343.18	3,125.01	0.0316	1,647.26	4.44	14°	SPFmax
		346.2	3,119.7	0.0314	1,666.19	4.47	14.08°	Taylor-Maccoll
		0.87%	0.17%	0.58%	1.14%	0.60%	0.57%	% error
13	9°	349.54	3,378.86	0.0336	1,640.50	4.38	14.57°	SPFmax
		357.2	3,451.46	0.0336	1,659.57	4.38	14.82°	Taylor-Maccoll
		2.15%	2.10%	0.15%	1.15%	0.03%	1.69%	% error
14	10°	364.84	3,845.91	0.0366	1,627.05	4.26	16.17°	SPFmax
		368.9	3,815.6	0.0361	1,652.41	4.29	15.61°	Taylor-Maccoll
		1.10%	0.79%	1.35%	1.53%	0.84%	3.59%	% error

The lower-velocity Mach 2 test case results are in Table 4.10. Similar to the flat plate validation, the errors are slightly higher, particularly shock angle, but within the 10% threshold. Interestingly, all parameters except shock angle are predicted lower than their theoretical values.

Table 4.10: Right circular cone flow, Air @ Mach = 2

Run #	Cone half-angle	Temp (K)	Pressure (Pa)	Density (kg/m^3)	Velocity (m/s)	Mach	Shock Angle	
8	10°	306.99	1,957.29	0.022	625.24	1.78	34.2°	SPFmax
		309.92	2,136.6	0.024	647.19	1.83	31.2°	Taylor-Maccoll
		0.94%	8.39%	7.82%	3.39%	2.73%	9.62%	% error

The final stretch case results, with CO_2 as the fluid, are presented in Table 4.11. Density is predicted low by roughly 7%, while all other parameters are within roughly 5%. Interestingly, this case and run 15 are the only cases in which the temperature is predicted higher than their theoretical values.

Table 4.11: Right circular cone flow; CO_2 @ Mach 5

Run #	Cone half-angle	Temp (K)	Pressure (Pa)	Density (kg/m^3)	Velocity (m/s)	Mach	Shock Angle	
18	20°	476.6	5,521.1	0.0599	1,159.87	3.42	24.2°	SPFmax
		463.3	5,656.8	0.0646	1,217.05	3.608	24.53°	Taylor-Maccoll
		2.86%	2.40%	7.27%	4.70%	5.21%	1.35%	% error

The detailed data behind tables 4.8-4.11 are presented in Table 4.12. Similar to the flat plate cases, included is the calculated T_{onset}, as described in Chapter 3, and the radial temperature at which this is reached (T_{y1}, T_{y2}) at the axial locations (x_1, x_2) along the cone.

Table 4.12: Detailed data for cone validation cases

Fluid	Mach	Run #	Cone half-angle	T_{onset} (K)	T_{y1}/T_{y2} (m)	x_1,x_2 (m)	y_1/y_2 (m)	z_1,z_2 (m)	ts_1, ts_2
Air	2	8	10°	289.90	0.60	-1.0		0.0, 0.0	20, 40
					0.26	-0.5	0.16		
	5	9	5°	289.55	0.52	-2	0.28		
					0.32	-1	0.16		
		10	6°	290.60	0.56	-2	0.32		
					0.34	-1	0.20		
		11	7°	292.12	0.59	-2	0.32		
					0.34	-1	0.20		
		12	8°	293.52	0.61	-2	0.36		
					0.36	-1	0.20		
		13	9°	294.15	0.65	-2	0.4		
					0.39	-1	0.24		
		14	10°	295.68	0.68	-2	0.44		
					0.39	-1	0.24		
		15	15°	304.03	0.65	-1.5	0.46		
					0.47	-1.0			
		16	20°	311.06	0.66	-1.25	0.52		
					0.44	-0.75			
		17	25°	320.89	0.65	-1.0	0.52		20, 35
					0.36	-0.5			
CO_2		18	20°	307.85	0.675	-1.25	0.52		20, 40
					0.45	-0.75	0.32		

4.3 Convergence Results

A primary concept behind particles in SPH is that each particle is small enough in physical space to represent a homogeneous volume of the working fluid. SPH particles are not intended to represent individual molecules—an important distinction—but rather a small volume of fluid in which all properties are the same. However, given unlimited memory and processing capability, and the number of modeled particles approaches infinity, the homogeneous fluid volume will shrink; thus, eventually a particle would become an analogue to a molecule and the errors would be eliminated [89,90]. This can be proven via convergence testing, wherein the same simulation is run several times with differing numbers of particles, allowing trends to be discovered.

In SPH, convergence rate verification is typically done with the density parameter, as it is the state directly calculated by the equations of motion. This can be approximated to the lowest order, p, via

$$\left|\frac{x_n-\xi}{\xi}\right| \propto C\, n^{-p} \tag{4.2}$$

where C is a constant, n is the number of particles, ξ is the exact solution, and x is the SPH-calculated value. For this dissertation, convergence rate analysis was conducted for a 10° half-angle right circular cone in air at Mach 5, with n = {164,000; 120,000; 70,000; 22,000}. Table 4.13 shows the data for which a power series curve was fitted, with the results of the fit shown in Figure 4.9.

Table 4.13: Density Convergence Rate Analysis Data

# Particles	SPH Density (kg/m^3)	Exact solution (Taylor-Maccoll)	% error
164,000	0.03642	0.0361 kg/m^3	0.88
120,000	0.03640		0.84
70,000	0.03687		2.14
22,000	0.02927		18.92

The convergence rate, p, is 1.83, with a constant, C, of 1.677×10^7. This convergence rate is of the same order as found determined by Zhu, et. al.[90]. It should be noted that even with the seemingly spurious large error at n = 164,000, Figure 4.9 is a log-log plot, increasing the apparent error; the power series was a tight fit, with $R^2 = 0.9992$ with a Root Mean Square Error of 0.003053.

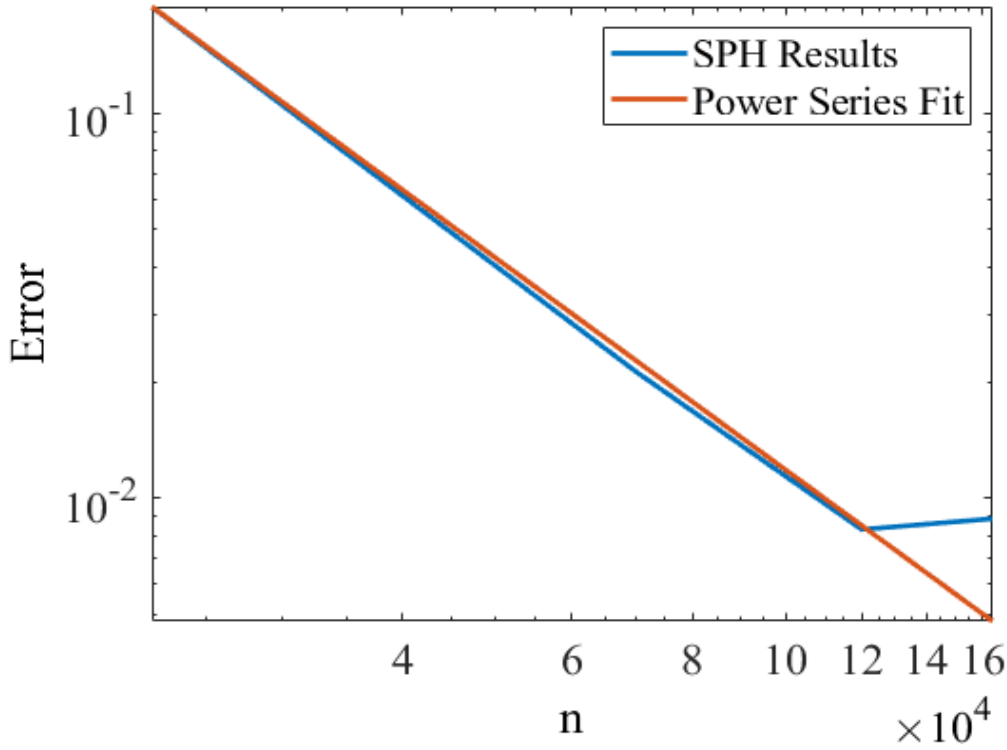

Figure 4.9: Convergence Rate for Density

For completeness, the same analysis was performed for temperature, which is typically the most difficult post-shock parameter for SPH methods to match. Table 4.14 includes these data, with Figure 4.10 showing the curve fit.

Table 4.14: Temperature Convergence Rate Data

# Particles	SPH Temperature (K)	Exact Solution (Taylor-Maccoll)	% error
164,000	365.35	368.9 K	0.96
120,000	367.74		0.31
70,000	370.83		0.52
22,000	432.51		17.24

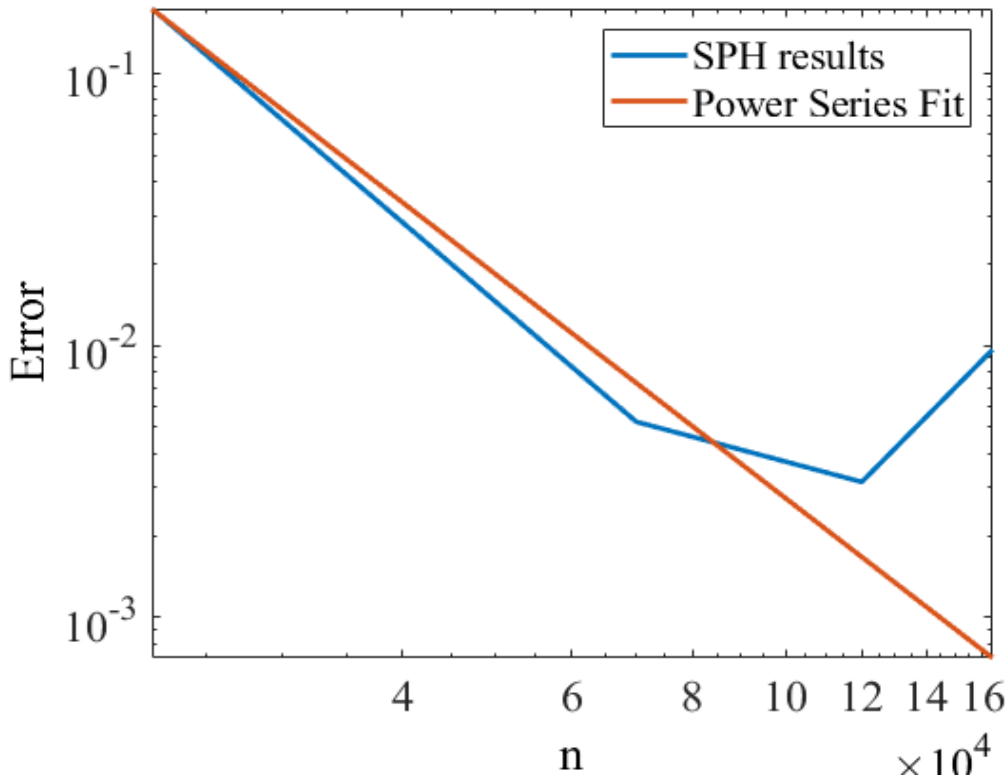

Figure 4.10: Temperature Convergence Rate

Here, the convergence rate is 2.733 with the constant at 1.268×10^{11}. There were no data found in the literature with which to compare this temperature convergence rate. For temperature, $R^2 = 0.9959$ with a Root Mean Square Error of 0.006551—again, a very tight curve fit.

4.4 3D Cone Vibration Validation

The primary source of data for vibration validation comes from Liu, et.al. [7], where sting frequency response is provided as well as raw (noisy) wind tunnel measurements of a Mach 7 simulation approximating 35 km altitude. The aluminum wind tunnel, shown in Figure 4.11, model is 1.5 m long, a base diameter of 0.518 m, and a mass of 57 kg. The length and diameter were both replicated in SPFmax. Table 4.15 contains the other parameters of the simulation, with Total Enthalpy and Total Pressure provided by Liu based on the JF12 shock tunnel capabilities and density and temperature derived from the 1976 US Standard Atmosphere [91] at 35 km altitude.

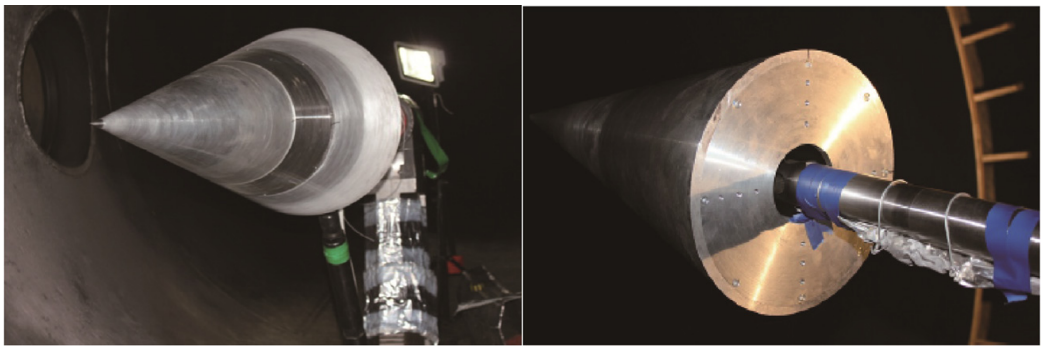

Figure 4.11: Liu Wind Tunnel Model

Table 4.15: Flow properties for Liu validation simulations

Cone half-angle	Altitude (approx, km)	Mach	Total Enthalpy (MJ/kg)	Total Pressure (MPa)	Density (kg/m^3)	Temperature (K)
10°	35	7.0	2.5	3.0	0.011203	238.5

Figure 4.12 shows the data from Liu; namely, the axial force, normal force, and pitching moment measurements as strain gauge voltages. No information is provided to calibrate these strain gauge voltages to any physical-unit values, however, trends and relative amplitudes are sufficient for this validation. The frequency response of the sting is shown in Figure 4.13, with 2 primary frequency components at 39.7 Hz and 53.1 Hz.

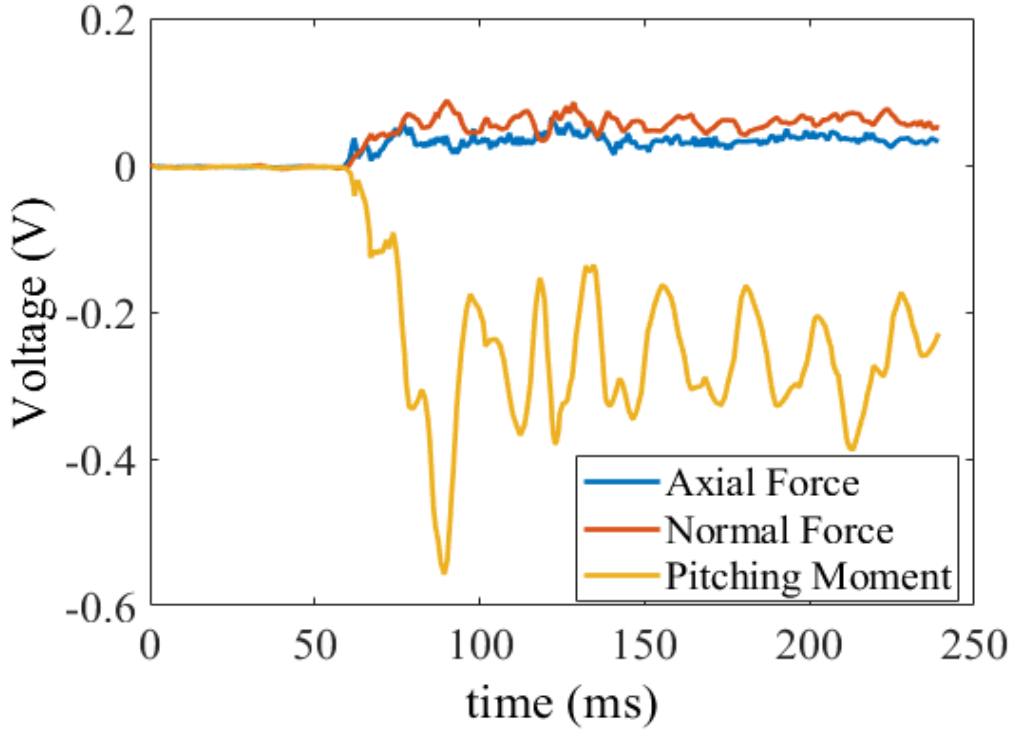

Figure 4.12: Raw wind tunnel data [7]

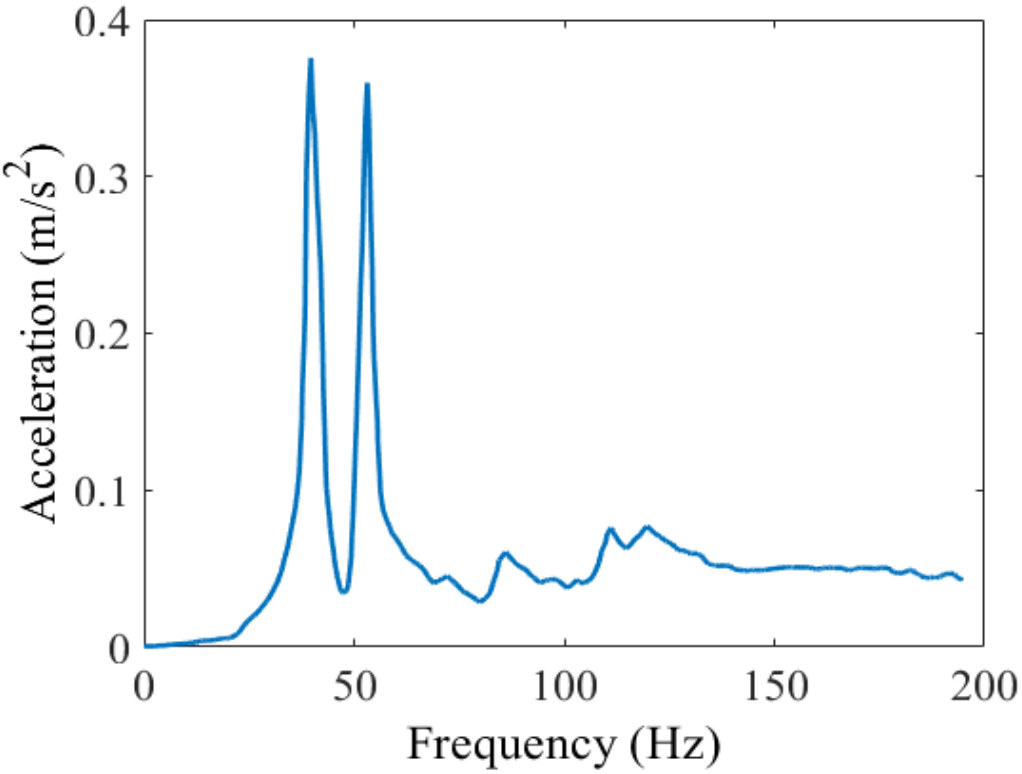

Figure 4.13: Frequency response of sting [7]

The sting frequency response was generated by placing the model in the wind tunnel prior to any flow analysis, and striking the apparatus with a hammer with the model accelerometers active in order to measure the accelerations experienced by the model. Using the acceleration data from Figure 4.13, the initial signal is reconstructed in the time domain with

$$S_t = A_1\cos(2\pi f_1 t) + A_2\cos(2\pi f_2 t) + \cdots + A_n\cos(2\pi f_n t) \tag{4.3}$$

where S_t is the time domain signal reconstruction, and A_n and F_n are the amplitude and frequency components, respectively. This reconstruction, shown in Figure 4.14, is helpful to visualize the impulse dissipation.

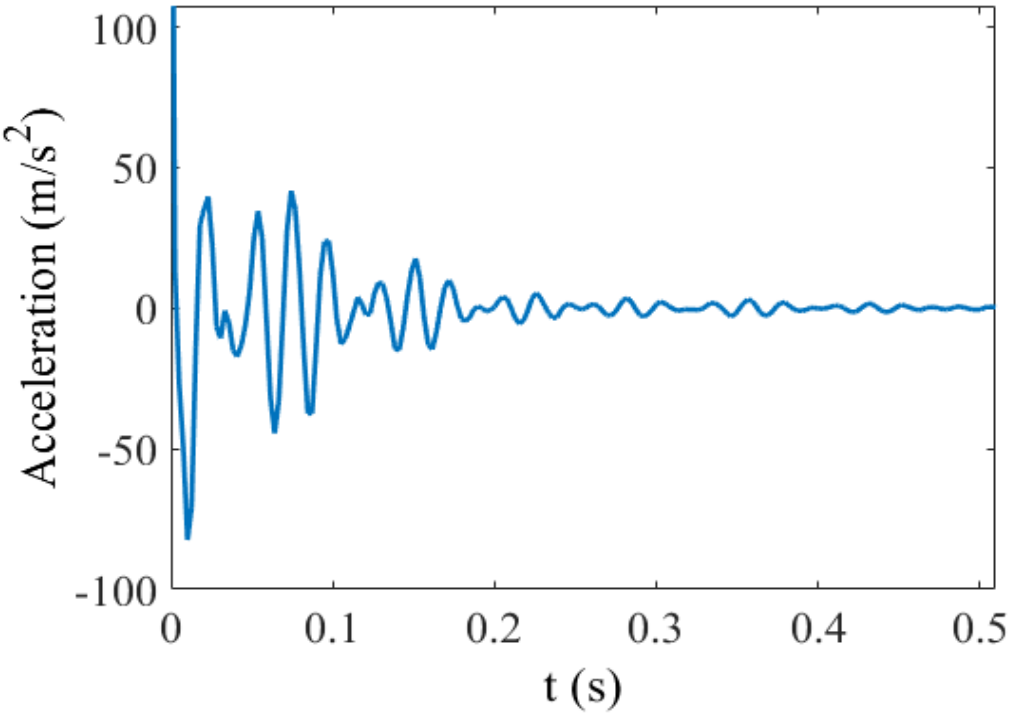

Figure 4.14: Time domain reconstruction of sting response

The Fast Fourier Transform (FFT), defined as

$$X_k = \sum_{n=0}^{N-1} x_n e^{\frac{-i2\pi kn}{N}} \tag{4.4}$$

where $I = \sqrt{-1}$, n is time, N is the number of samples, x_n is the value of the signal at time n, k is a frequency component, and X_k is the amplitude of frequency k in the signal [92], is used to convert time domain signals into the frequency domain. Truncating the

signals to not include the first 100 ms, as Liu states this data is unreliable due to the flow setting up, the FFT is applied to the data from Figure 4.12 in order to convert them from time domain signals into the frequency domain. The results, in Figure 4.15, show there are no recoverable usable frequency data in the axial and normal force measurements so pitch will be the primary focus for these analyses. The pitch results, interestingly, have several frequency peaks, with a large peak at 43.2 Hz, and smaller peaks at 28.8 Hz, 57.5 Hz, 79.2 Hz, and 115.0 Hz. The frequency resolution, R_f, given by

$$R_f = \frac{F_s}{N} \tag{4.5}$$

where F_s is the sample rate, is 7.13 Hz for the pitch moment data, meaning the frequencies are grouped into 'bins' 7.13 Hz wide, and are listed in Table 4.16. For the peak at 42.8 Hz to be so high compared with the next-lower bin, at 35.7 Hz, means the measurement has a frequency component very close to 42.8 Hz—not closer to the 39.7 Hz predicted by the sting analysis—otherwise, the value at 35.6 Hz would be similar in magnitude to the value at 42.8 Hz. Likewise, the sting response at 53.1 Hz falls roughly between the FFT bins at 49.9 Hz and 57.0 Hz, yet the peak is primarily at 57.0 Hz.

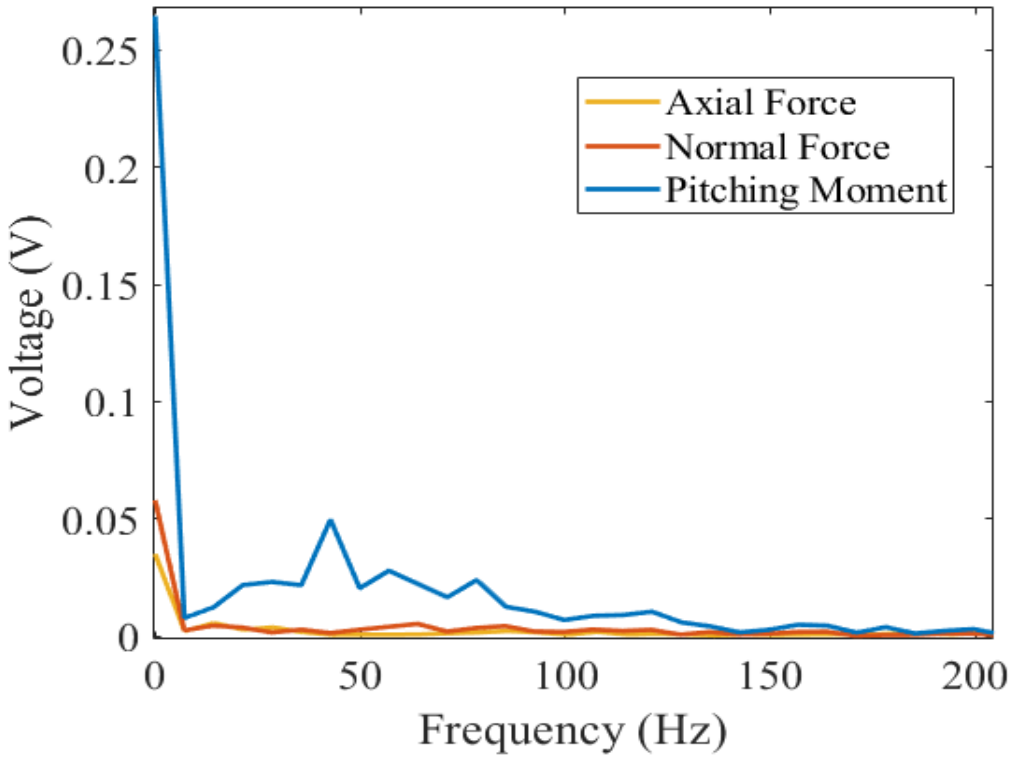

Figure 4.15: FFT of raw wind tunnel data

Table 4.16: Frequency bins after FFT

Bin #	0	1	2	3	4	5	6	7	8	9	10	11	12	13
Frequency (Hz)	0.0	7.1	14.3	21.4	28.5	35.7	42.8	49.9	57.0	64.2	71.3	78.4	85.6	92.7
Bin #	14	15	16	17	18	19	20	21	22	23	24	25	26	27
Frequency (Hz)	99.8	106.9	114.1	121.2	128.3	135.5	142.6	149.7	156.9	164.0	171.1	178.3	185.4	192.5

Figures 3-5 of Ref. [7] shows the stress balance is mounted to the rear of the wind tunnel model. From the pictures and description it can be determined that the primary motion is a rotation about the point at which the sting is mounted to the wind tunnel wall with a moment arm of approximately 1.75 m, based on the 3.5 m diameter of the test section. While the amplitude of vibration is not given, it is expected the motion would be small such that the motion would be primarily in the windward/leeward direction. Nevertheless, in the presentation of the modeling of these data these data, two vibration models are studied: linearly in the ± x-axis direction, with a maximum displacement of 5 cm; and rotationally (pitching) about the nose of the cone, with a maximum angular displacement of 0.15° in angle of attack. If the model is vibrated using the method shown in Chapter 3 at the frequencies experienced during the sting measurements, 39.7 Hz and 53.1 Hz, with relatively magnitudes of 1.0 and 0.95, respectively, the pressure traces correspond the same frequency components, as shown in Figure 4.16. The wide peak starts at 35.97 Hz and ends at 57.56 Hz, thus fully encompassing the primary frequencies within the FFT bins, with the slightly lower levels shown on to the right, corresponding to the 0.95 relative magnitude. The smaller peak at 158 Hz is likely a harmonic of the 39.7 Hz vibrational mode.

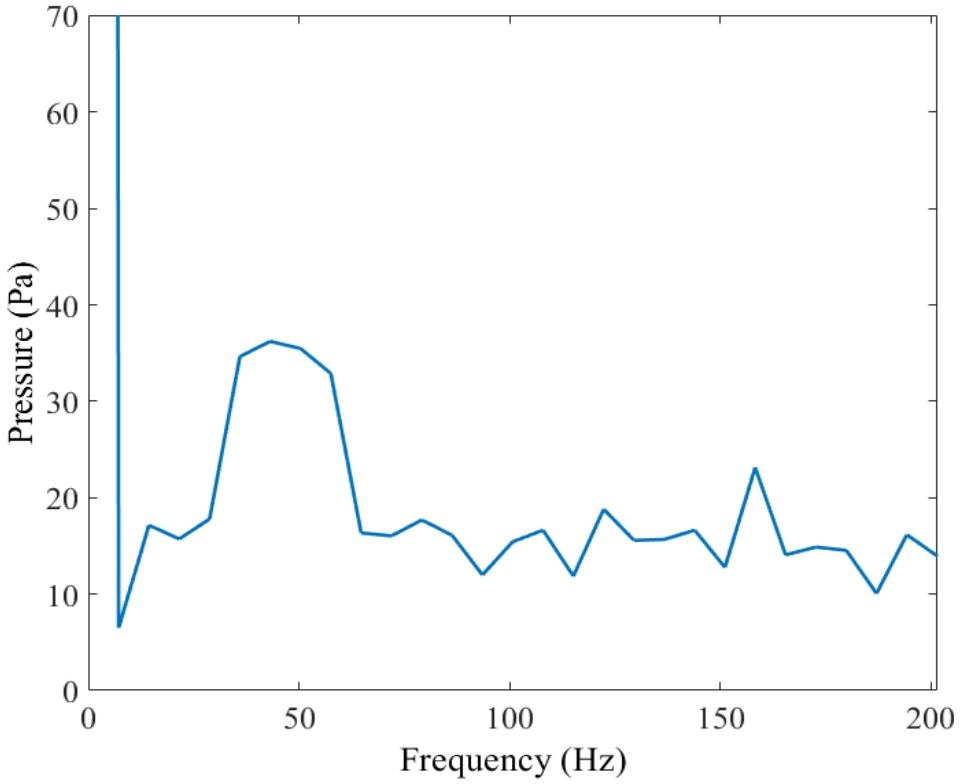

Figure 4.16: SPFmax Simulation with Vibrations at 39.7 Hz and 53.1 Hz

However, if the simulations are vibrated linearly with a noise profile specifically chosen to match the frequency response of the Liu data, the relative magnitudes and placement are more accurately replicated, as shown in Figure 4.17. Here, the model was vibrated at the frequencies recovered from the data—28.8 Hz, 43.2 Hz, 57.5 Hz, 79.2 Hz, and 115.0 Hz—with relative magnitudes of 0.45, 1.4, 0.6, 0.45, and 0.25, respectively, with a gross magnitude of 0.05 m/s^2 to any one frequency, corresponding to roughly 1 h-distance. This magnitude was chosen arbitrarily as the primary goal for this validation is to match relative magnitudes and frequency positions. Using the largest frequency peak, the response at 43.2 Hz, to normalize the others, the simulation matched the Liu

data within 1.2%, 2.6%, 2.8%, and 36.9% at 28.8 Hz, 43.2 Hz, 79.1 Hz, and 115.0 Hz, respectively. This assumed anchoring the data to a perfect match at 43.2 Hz, with no error. The frequency response of the boundary particles is shown in Figure 4.18, demonstrating the frequency placement and relative magnitudes. SPFmax determines the sampling rate, via the routine to calculate time-step, which, for these simulations, averages 39.66 kHz (an average time-step of 25.2 μm). In order to match the 7.13 Hz frequency resolution of the Liu data, the SPFmax simulation are run for 139 ms, as appropriate to satisfy Eq. (4.5), in order to simplify frequency/amplitude matching.

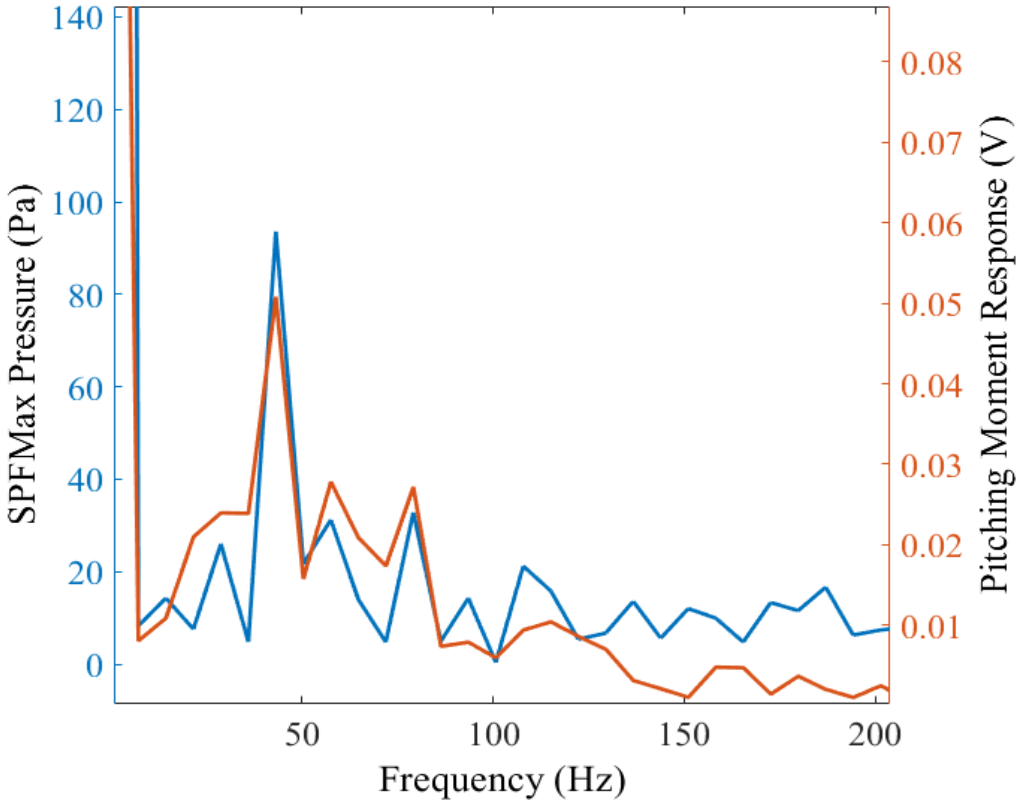

Figure 4.17: Multiple Frequency Components Matched with Simulation

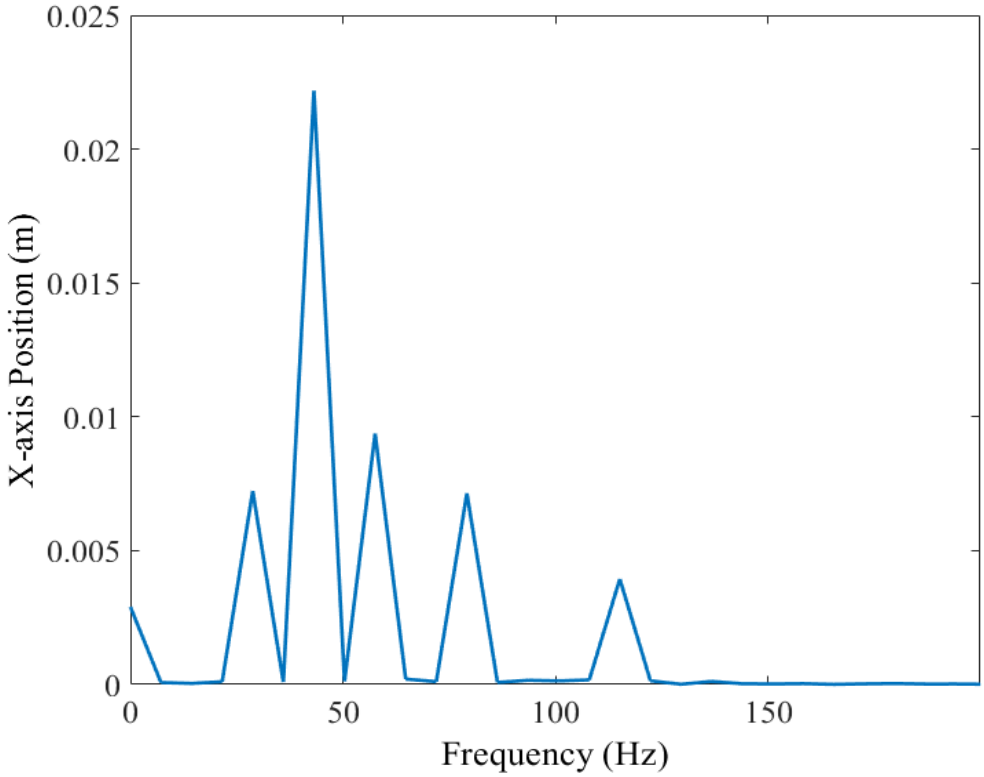

Figure 4.18: Frequency Response of Conical Body

Using the same noise profile to vibrate the model in angle-of-attack produces a similar result, shown in Figure 4.19. However, unexplained higher-order harmonics and frequency components surface, particularly above 150 Hz. As a result, the remainder of these analyses will be conducted with a linear-only motion simplification, with the understanding that the real captures in the wind tunnel data is likely complex with both liner and rotational vibrational modes.

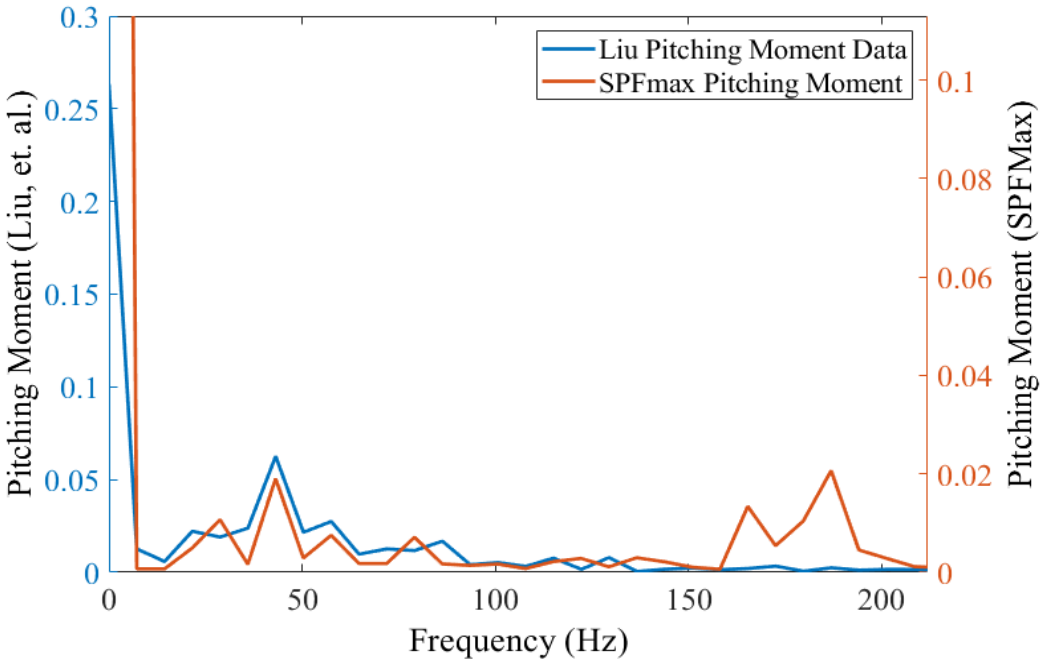

Figure 4.19: Pitching moment comparisons with noisy angle of attack

This demonstrates the frequencies obtained via sting response analyses are not directly superimposed onto the measurement data, but also that SPH methods are capable of faithfully matching the data. It is also interesting to note that the relative magnitudes are not directly superimposed upon the data, indicating the flow has a hand in amplifying or attenuating certain frequencies.

4.5 Filter vs no-filter Comparisons

Wind tunnel data is typically notch filtered in order to remove the sting vibrational effects [93]. This section will present results of such filtering. For the sting response from Figure 4.13, with peaks at 39.7 Hz and 53.1 Hz, usually 2 filters would be

designed with separate notches [94], or simply averaged [7], which acts as a simple low-pass filter. However, since the wind tunnel data provided is short in duration, with a best-case frequency resolution of 7.13 Hz due to constraints from Eq. (4.5), these analysis are conducted with 1 notch, covering 35.7 Hz to 57.0 Hz; otherwise the notches would not align with the sting's frequency peaks. For example, the 39.7 Hz peak is between the frequency bins of 35.7 and 42.8 Hz, and the 53.1 Hz peak falls between the 49.9 Hz and 57.0 Hz bins. The frequency response of the filter used is shown in Figure 4.20. Filtering was accomplished by performing the FFT on the data, as described in Eq. (4.4) and nulling out the amplitudes at the frequencies of interest. This frequency domain data is then reconstructed into the time domain via the inverse FFT, which reverses the operation as performed via the FFT, and is defined as

$$x_n = \frac{1}{N} \sum_{k=0}^{N-1} X_k e^{\frac{i 2 \pi k n}{N}} \tag{4.6}$$

where x_n is the signal at time n, and X_k is the amount of frequency k in the signal. This filtering method did not upset the power spectral density as the amplitude values at these filtered-out frequencies is relatively small, especially compared to the 0 Hz offset, and the fact that very few frequency bins are modified.

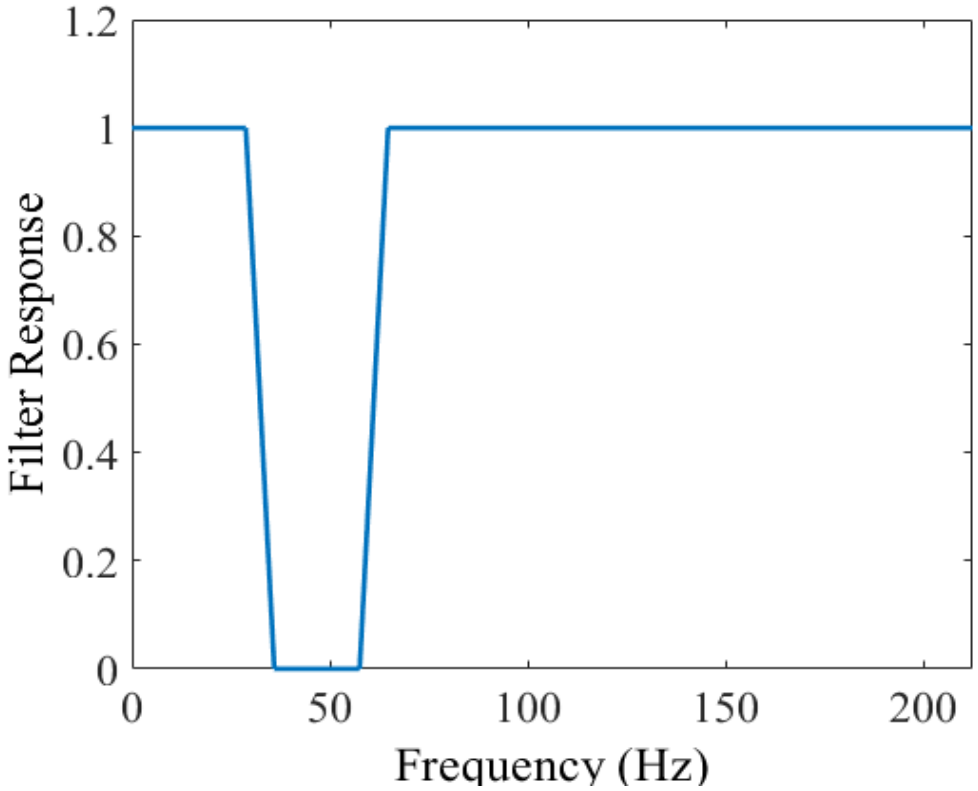

Figure 4.20: Frequency response of notch filter used in analysis

Figure 4.21 graphically depicts the filtering procedure used, and how the plots of this section are generated. The second round of transformations is to verify the filtering did not extensively upset the power spectral density of the signal. Additionally, a group delay [95] is introduced to the signal when reverted back to the time domain after the FFT defined by

$$T_g(f) = -\frac{1}{2\pi}\frac{d\,\theta(f)}{df} \tag{4.7}$$

where, f is frequency and $\theta(f)$ is the phase response defined as

$$\theta(f) = -2\pi f t_0 \tag{4.8}$$

where t_0 is the initial time of the function. This delay effect is ignored in these analyses because aside from plotting the time domain signals for display and inspection purposes, no other analyses are performed strictly in the time domain. However, if in-situ filtering is ever performed, this effect will be come more pronounced.

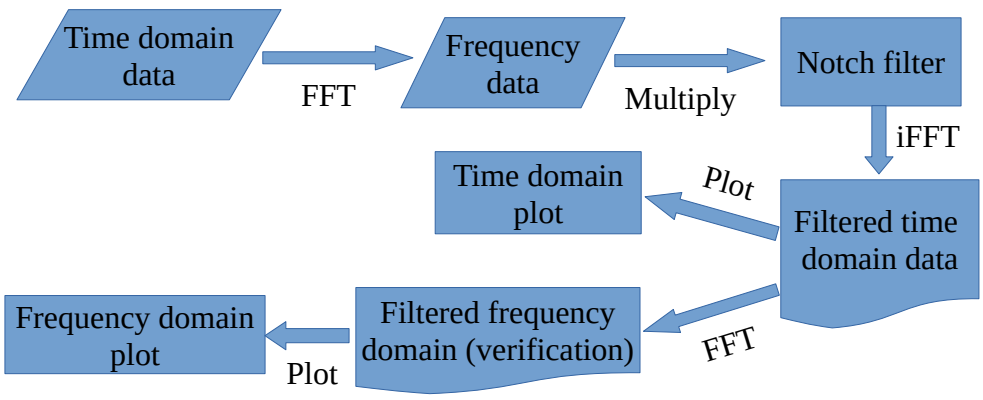

Figure 4.21: Filtering Process

The first results shown demonstrate the result of filtering in the event the model actually vibrated in accordance with the frequency response of the sting. The simulation modeled vibrations at the sting's peaks of 39.7 Hz and 53.1 Hz. The resulting data filtered using the notch described in Figure 4.20. Figure 4.22 shows the signals compared in the time domain, while Figure 4.23 is the frequency responses. This shows, again, if the

model vibrated only with the frequency characteristics of the sting, filtering the sting's response frequencies does, in fact, leave all other frequency components. However, if simple averaging (i.e. low-pass filtering) is used, all frequency data would be lost; which, as demonstrated here, would lose an important artifact at ~160 Hz—roughly the 4th harmonic of the 39.7 Hz peak.

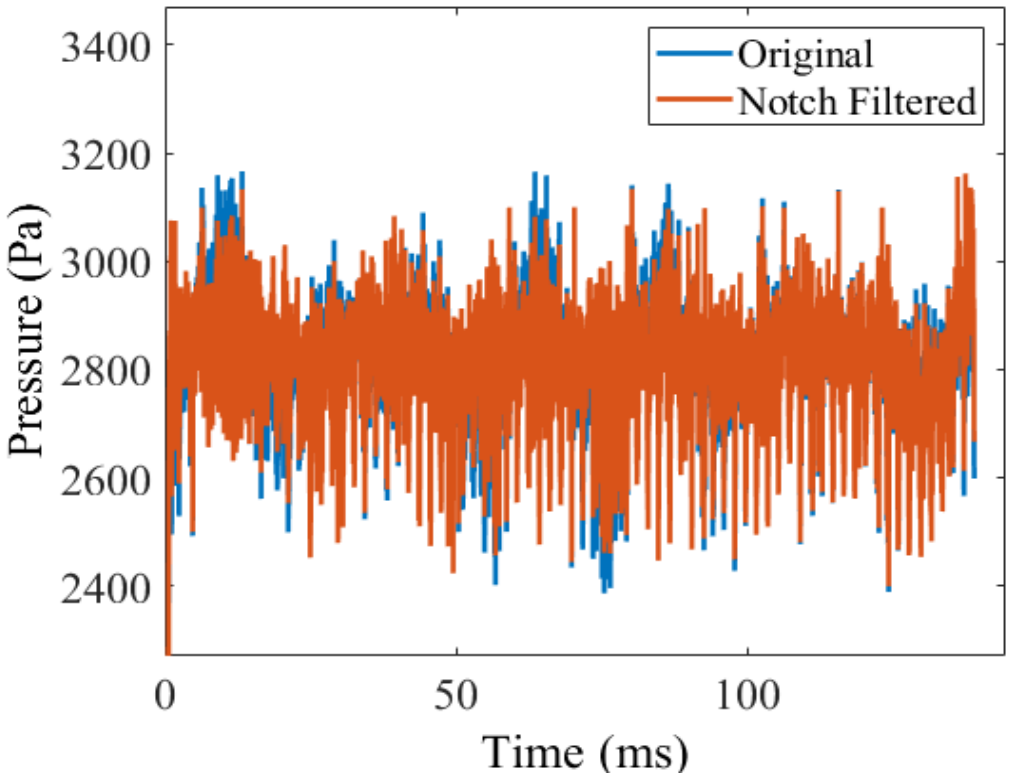

Figure 4.22: Time domain signals with model vibrated at sting frequencies

Figure 4.23 also shows the filtering did not appreciably affect the power spectral density of the data, and simply nulled out the frequencies of interest, due to how closely the pre- and post-filtered data overlay.

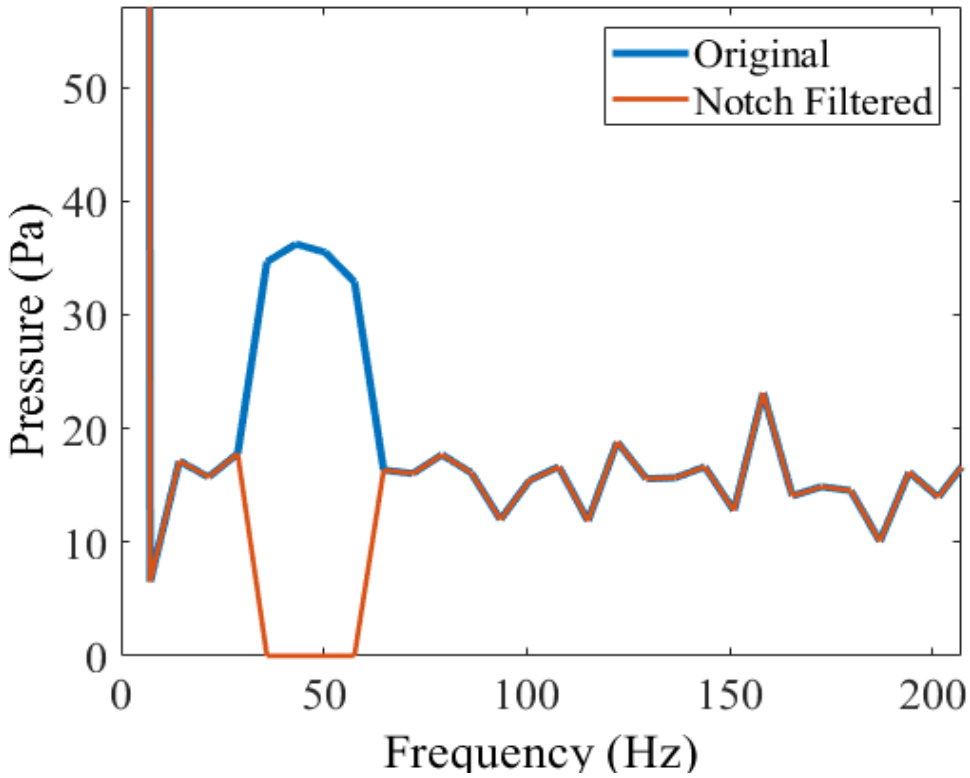

Figure 4.23: Frequency response with model vibrated at sting response

If the model is vibrated according to the data as demonstrated in Section 4.4, notch filtering is not as effective. Similar to the previous case, Figure 4.24 compares the filtered and unfiltered simulation data in the time domain while Figure 4.25 is the corresponding frequency domain signals. While the notch is effective at removing 2 of the large peaks in the data cause by model vibrations, it is ineffective at removing the peaks at 29.8 Hz and 79.2 Hz.

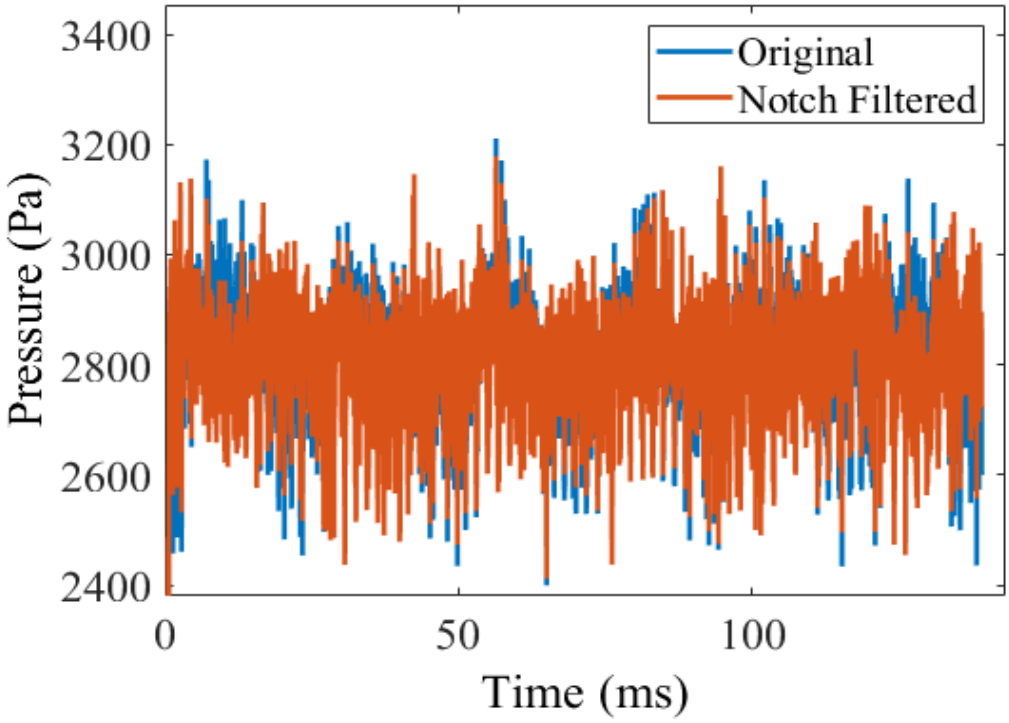

Figure 4.24: Time domain signal of filtered simulation data with accurate vibrations

Again, the data overlay perfectly in the frequency domain in Figure 4.25, thus proving the power spectral density is not upset by the notch filtering.

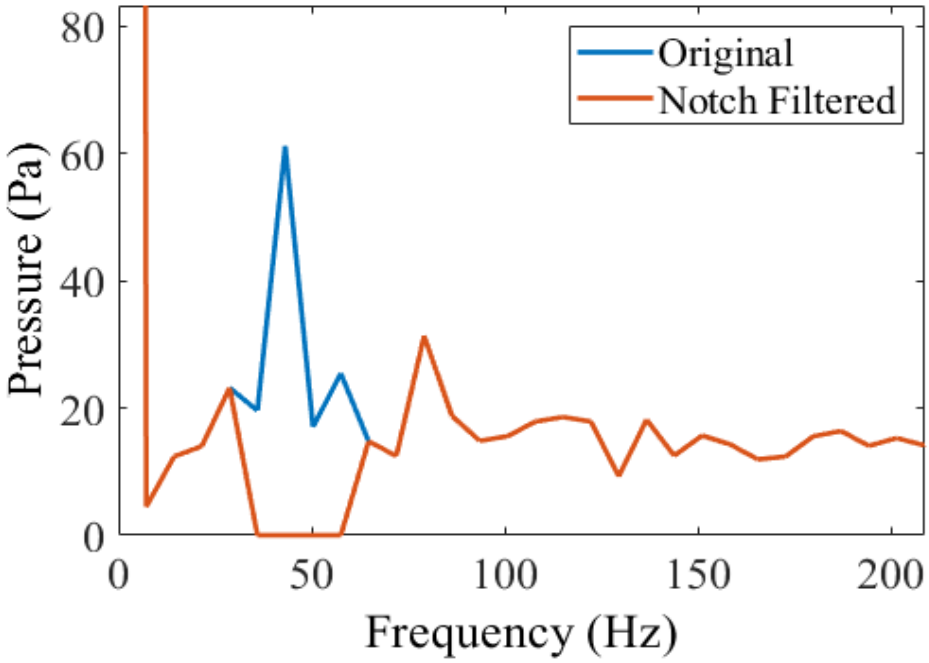

Figure 4.25: Frequency response of filtered simulation data with accurate vibrations

Combining all the data from Section 4.4 and this section, the data is shown again in Figure 4.26 overlaid with the data from Figure 4.17; the voltages from the pitching moment strain gauge. The notch filtering left a relatively large peak at 78.4 Hz, which is likely the 2nd harmonic of the 43.2 Hz frequency simulated; they are not perfect multiples of one another due to the frequency bins of the FFT.

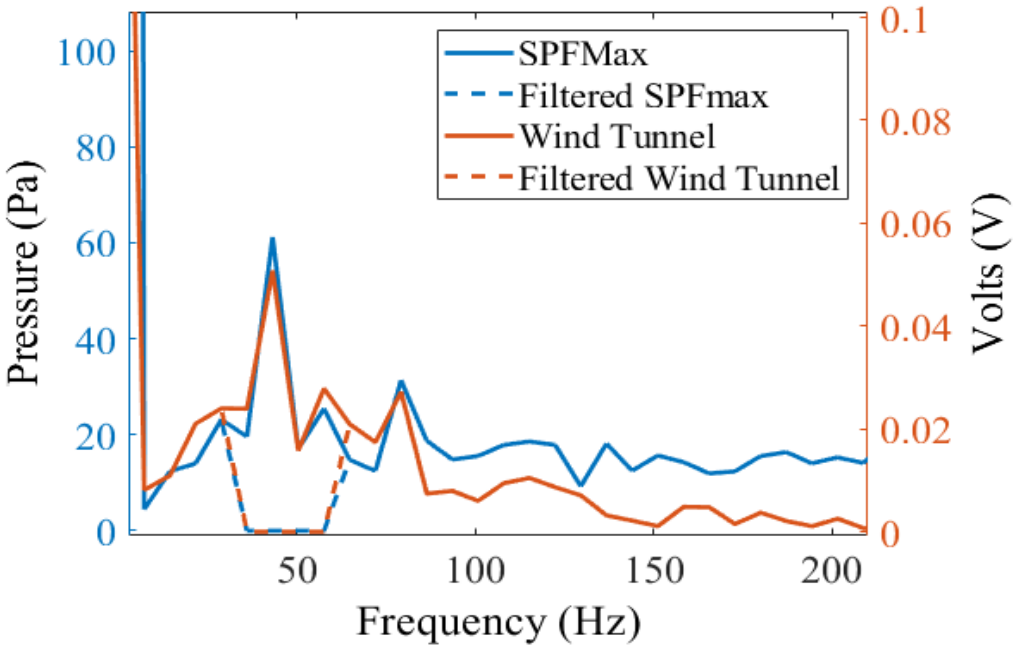

Figure 4.26: Frequency response data overlaid with wind tunnel data

4.6 Hypersonic Flow and Frequency Attenuation

With the SPH method validated for simulating vibrations, the capability is then used to model extended test cases to discover the impacts on aerodynamics forces and moments as well as conduct sensitivity analyses. For example, to determine what harmonics are present, and possibly dominate, when the model is vibrated at particular frequencies. Table 4.17 is the list of test cases, which provide the ability to observe trends in the force and moment coefficients as a function of incidence angle as well as which variables provide the most effect on the flight dynamics. A non-vibrating case, run 25, is included for completeness to compare against its comparable vibrating twin, case 21.

Table 4.17: Test cases for varying angle of attack and sensitivity analysis

Run #	Fluid	Mach	Altitude (km)	Cone Half-angle	Frequency (Hz)	Amplitude (m, in x-direction)	Angle of Attack
19	Air	5	30	10°	40, 100	0.05 (max gross amplitude)	0°
20							5°
21							10°
22							15°
23				15°			5°
24			20	10°			5°
25			30		None	N/A	10°

The frequencies of 40 Hz and 100 Hz are chosen for several reasons: they are reasonable compared to frequency responses of stings found in the literature; they have a relatively high least common multiple, 400 Hz, so the effects of harmonics will be easier to distinguish; and they are far enough apart that notch filtering would hypothetically be more effective and easier to implement than the previous section. The 30 km altitude, arbitrarily chosen but reasonable for hypersonic flight, prescribes free-stream temperatures and densities of 226.51 K and 0.01841 kg/m^3, respectively, via the 1976 Standard Atmosphere [91]. A lower, 20 km altitude case is included to investigate the impacts of differing free-stream conditions, namely a density of 0.08891 kg/m^3 and temperature of 216.65 K, again provided by the 1976 Standard Atmosphere. A final test case, with a 15° half-angle cone, is included to determine the effects caused by altering the geometry. The base diameter in all cases is 1.0 m, giving the simulated model a length of 2.836 m for 10° half-angle cones and 1.866 m for the 15° half-angle cone.

Example initial configurations for these runs are shown in Figure 4.27 with both 0° and 10° angles of attack, and 10° cone half-angle, where blue is the cone, red is the shear cylinder to keep the fluid cylinder, yellow, from collapsing and striking the point of the cone and causing stand off shocks. For clarity, only half of the fluid cylinder is shown.

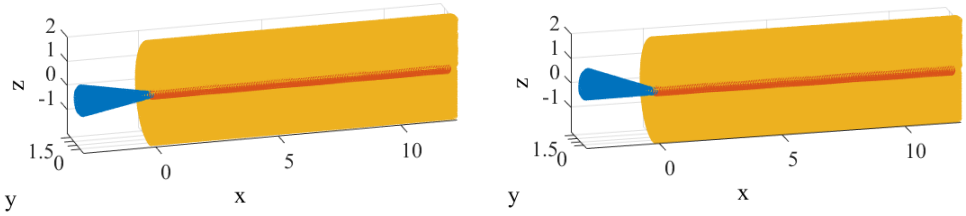

(a) (b)

Figure 4.27: Initial setup of (a) 0° and (b) 10° angle-of-attack cases

To verify the motion of the model, which is the same for all test cases in this section except run 25, the position of the nose tip is plotted in both time and frequency domains, shown in Figure 4.28 and Figure 4.29, respectively. The two frequencies are visibly superimposed in the time domain plot.

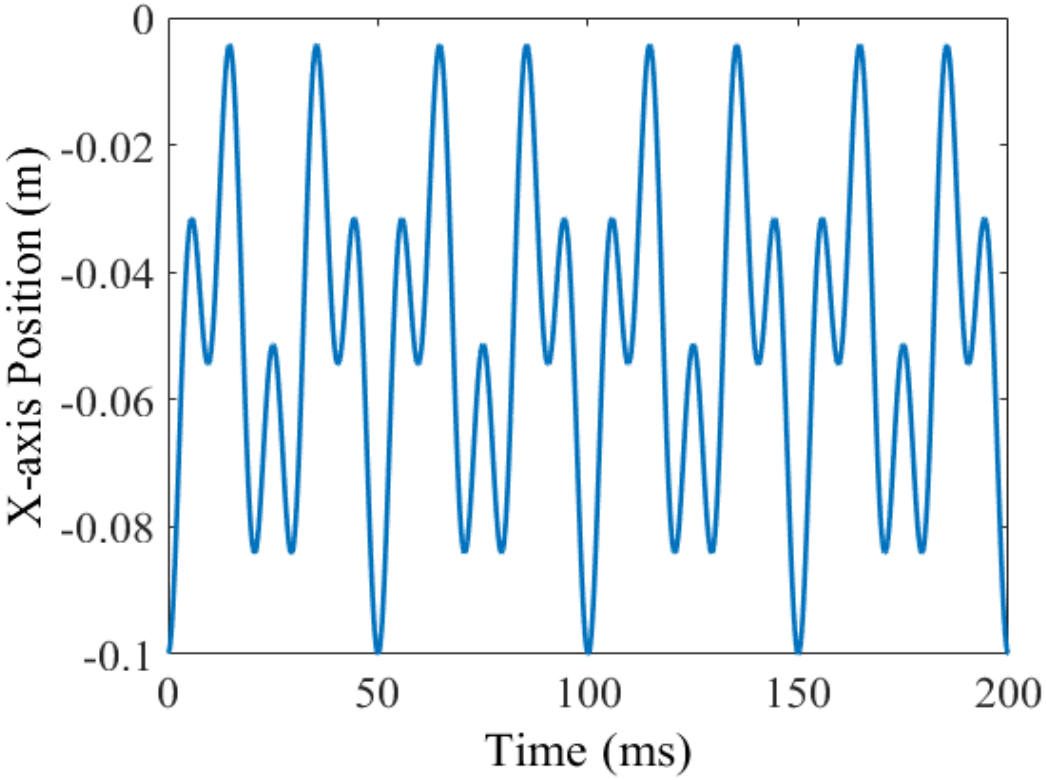

Figure 4.28: Time domain plot of cone nose tip

The 0 Hz value in Figure 4.29 is due to the nose tip being set at -0.05 m initially; essentially a DC-offset, and is shown in the time domain plot as the curve's rough average. The peak at 100 Hz is slightly smaller than the peak at 40 Hz, with amplitudes of 0.02561 m and 0.02433 m, respectively, verifying the 1.0 and 0.95 amplitudes implemented. The peaks sum to 0.04994 m thus verifying the 0.05 m gross position disturbance magnitude to within 0.1%; a difference likely due to machine accuracy.

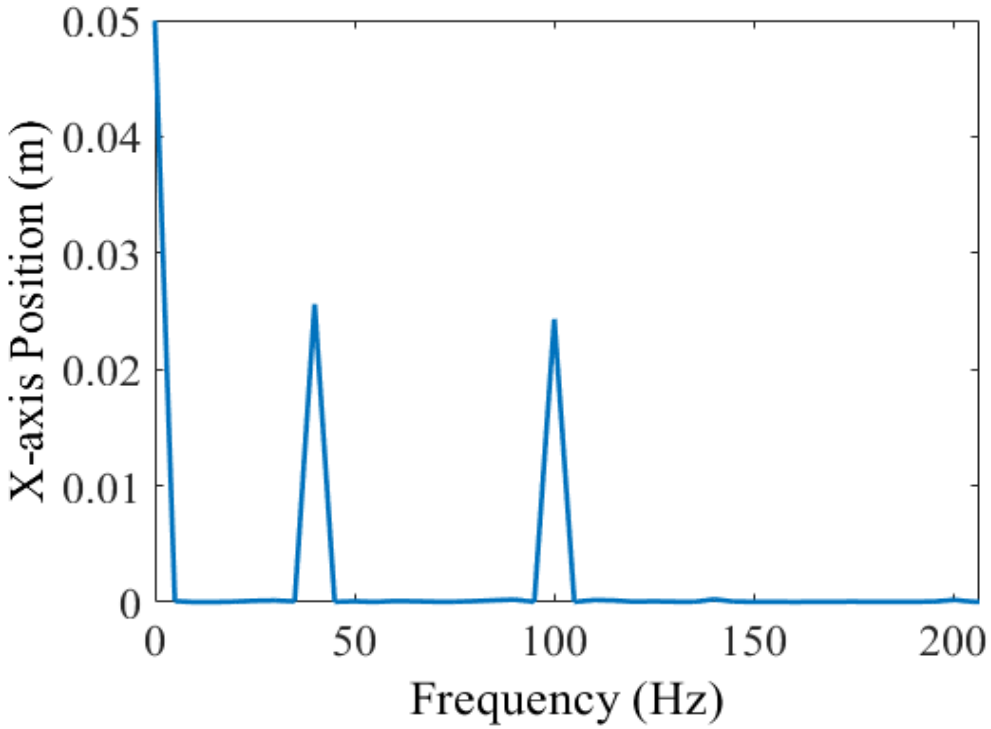

Figure 4.29: Frequency domain of body motion

The next step is to verify the forces and moment calculations to observe their overall trends and verify the method calculates these values accurately. Figure 4.30 is a plot of all the force and moment calculations for runs 19-24, taken by averaging the values throughout the simulation, prior to any frequency analysis. Of note is the self-consistency between runs 20 and 24—where the difference only is altitude—meaning the code does not introduce any errant artifacts stemming from ambient, free-stream conditions. The resulting trends are consistent with the literature for right circular cones at angles of incidence [96,97]. In particular, when comparing the 15° half-angle cone to the 10°, the facts that the C_l is roughly double, C_d is on the order of 3 times higher, and the L/D is roughly half, respectively, all agree very well with Roane

[97] at Mach 7 and Harris [96] at Mach 9.75. Pitching moment coefficients are difficult to compare due to the datum used, however the general trend is in agreement; namely, roughly a linear relationship versus angles of attack within this range. These trends are shown in Figure 4.31.

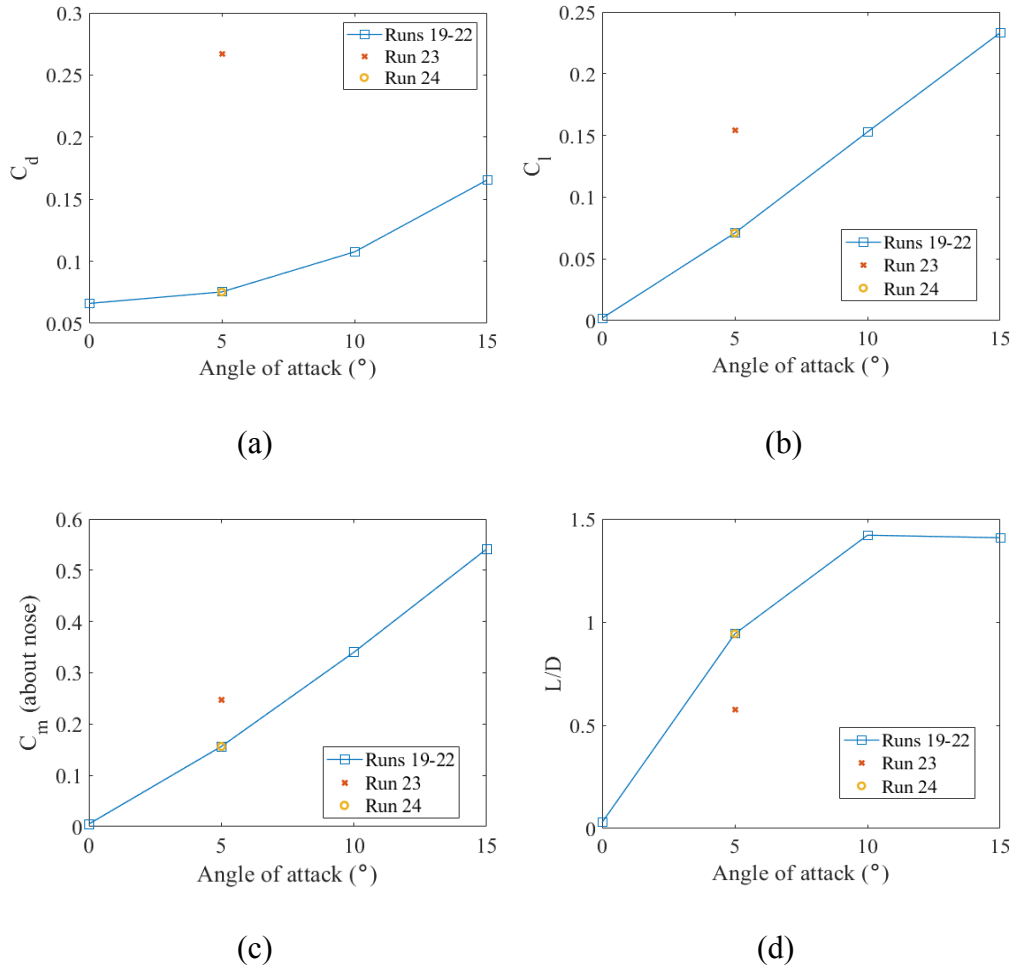

Figure 4.30: Forces and moment calculations for extended runs, with (a) drag, (b) lift, and (c) pitching moment coefficients and (d) L/D ratio

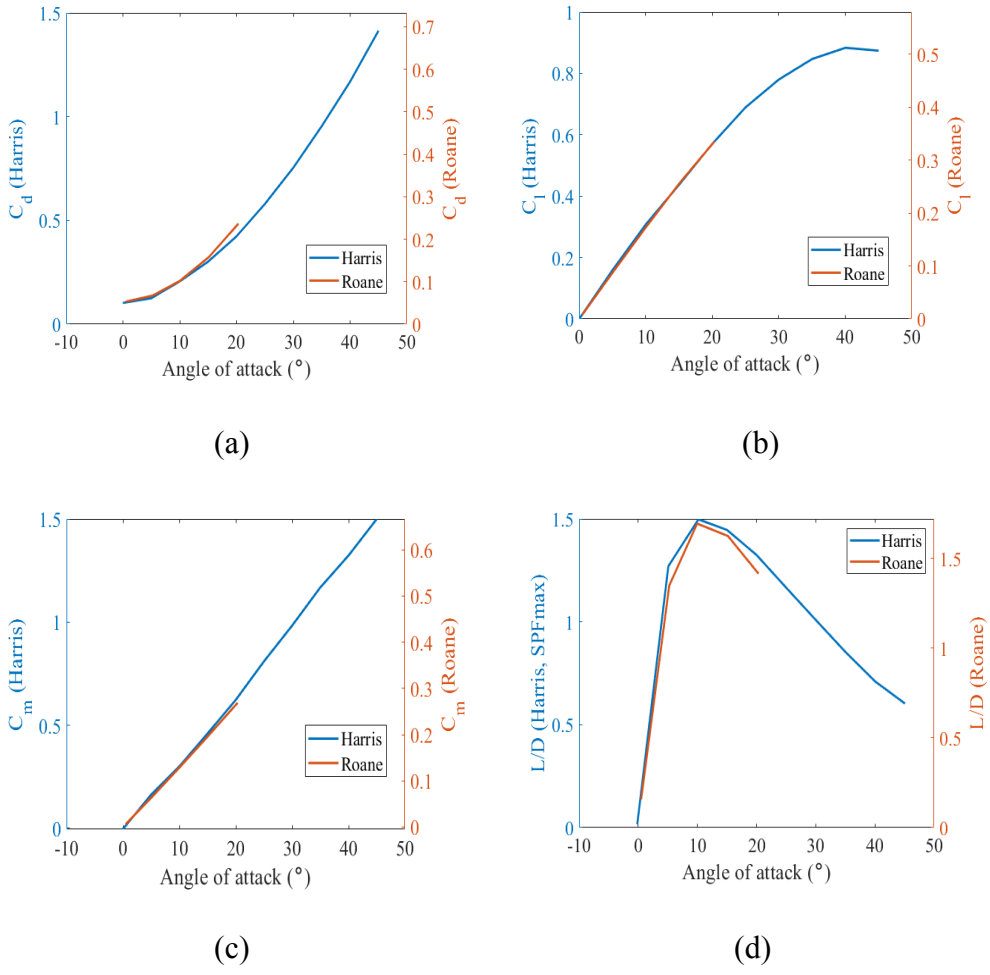

Figure 4.31: Forces and moment trends from literature

All these data are then processed through the FFT in order to quantify their frequency components and determine any observable trends. The simulations consist of 200 samples spanning 200.0 ms, which provides a frequency resolution of 5.0 Hz according to Eq. (4.5). Figure 4.32 shows the aerodynamic force and moment coefficients zoomed into the 0 Hz (DC offset) frequency bin, which, if no vibrations were present, would be the value for the coefficient. Another verification, helping to show the self-consistency of the model, the 0 Hz values for the coefficients for runs 20 and 24 are

virtually identical, making them difficult to discern in the plot; these are the 10° half-angle cones at 5° angle of attack, with run 20 at 30 km altitude and run 24 at 20 km altitude.

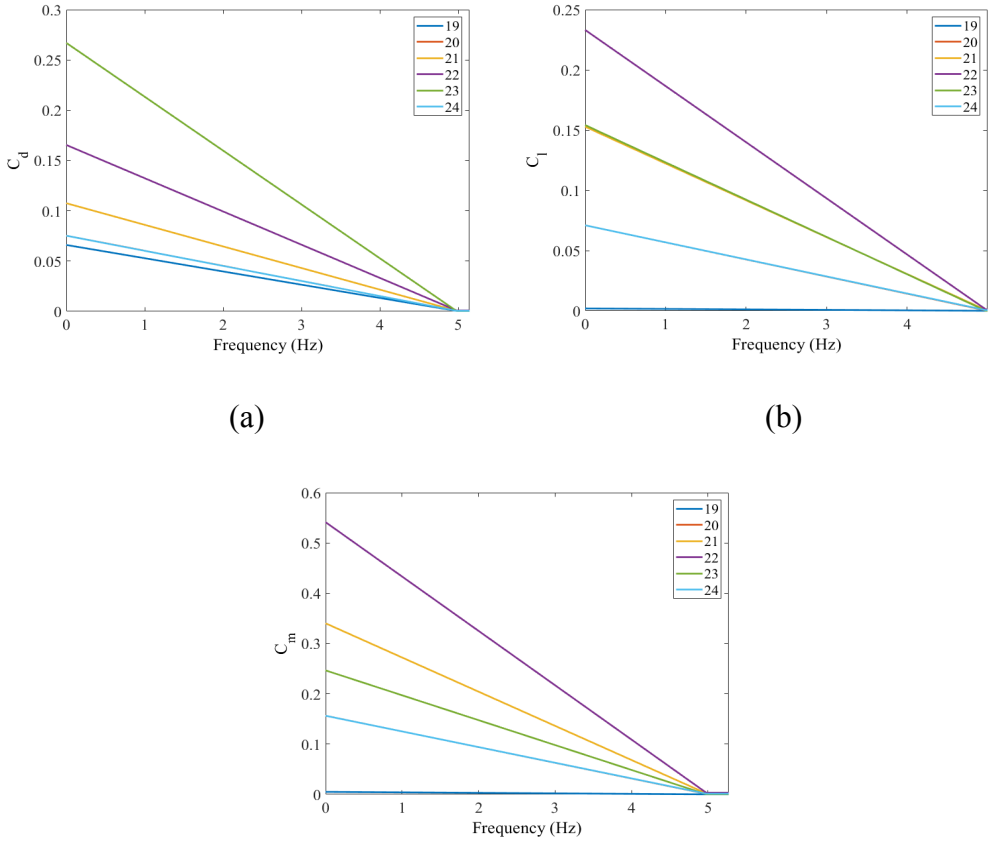

Figure 4.32: FFT of the (a) drag coefficient, (b) lift coefficient, and (c) pitching moment zoomed into the DC offset (0 Hz frequency bin). This would typically represent the long-term averaged, or noiseless value. The legend is the run number from Table 4.17

The 0 Hz values are particularly useful for the rest of these analyses as it is used to normalize the data across the rest of the frequency bins. Since force and moment coefficients are unitless, dividing them by the DC offset provides a means to scale them in order to speak to their relative magnitudes, say, as a percentage of the non-vibrating

value. For the purposes of discussion, a peak in the frequency domain must exceed a minimum threshold of 2σ, or 2 times the standard deviation of the non-zero frequency amplitudes, in order to be considered of consequence and not divert attention to noise likely attributable to typical SPH variation. This is shown to be a reasonable threshold in Figure 4.33, which are the coefficients for run 25 where no vibrations are simulated and no peaks exceed the 2σ value.

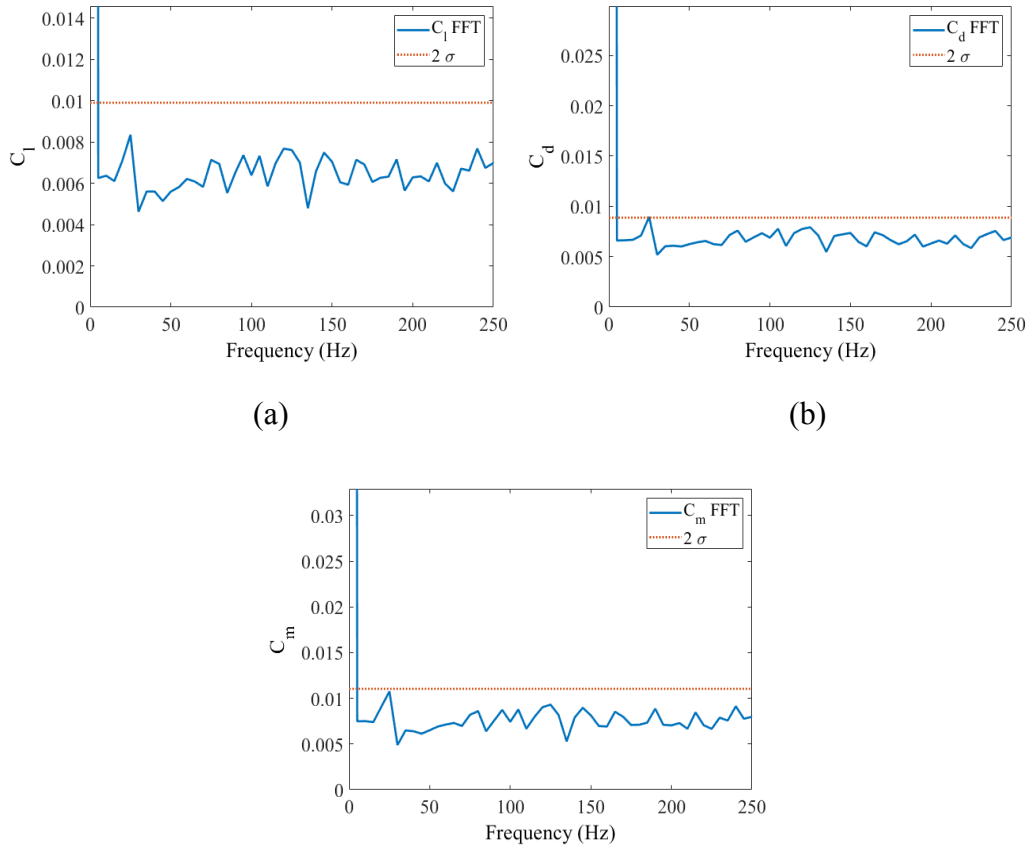

Figure 4.33: Normalized (a) C_l, (b) C_d, and (c) C_m coefficients for run 25 (non-vibrating)

Figure 4.34 is the normalized lift coefficient for run 19, which is the 10° half-angle cone at 0° angle of attack. There are 3 peaks that exceed the 2σ threshold; 2 of which are to be expected, at 40 Hz and 100 Hz; however there is an unexpected peak at 135 Hz. Their amplitudes are 8.5%, 13.8%, and 9%, respectively, of the 0 Hz value which, from Figure 4.32, is almost zero at 0.002, which is to be expected for an axi-symmetric shape at no angle of attack.. Therefore, it is unexpected for these peaks to have any influence on the flight dynamics, but are included for completeness as they do appear in the data.

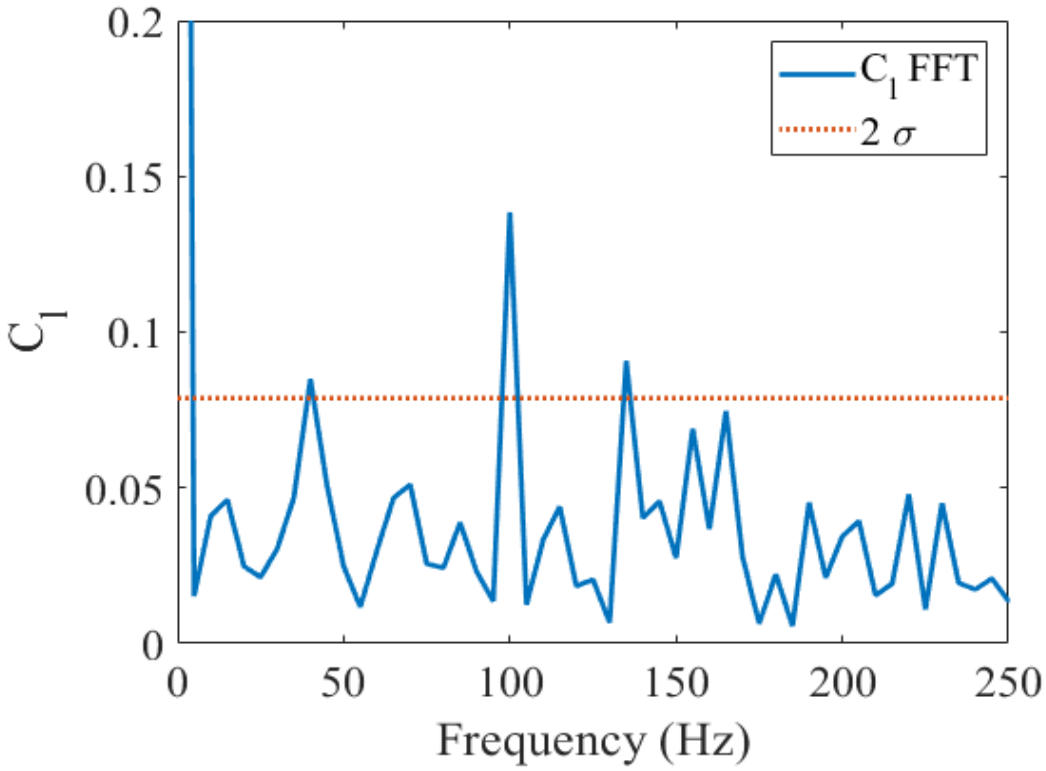

Figure 4.34: Normalized C_l in frequency domain for run 19

The drag coefficient is displayed in Figure 4.35 for the same run 19. Here, there are 2 peaks that exceed the 2σ threshold, with one at the expected 100 Hz, while the other is at 25 Hz, with relative magnitudes of 1.1% and 1.0%, respectively, compared to the 0 Hz value of 0.06.

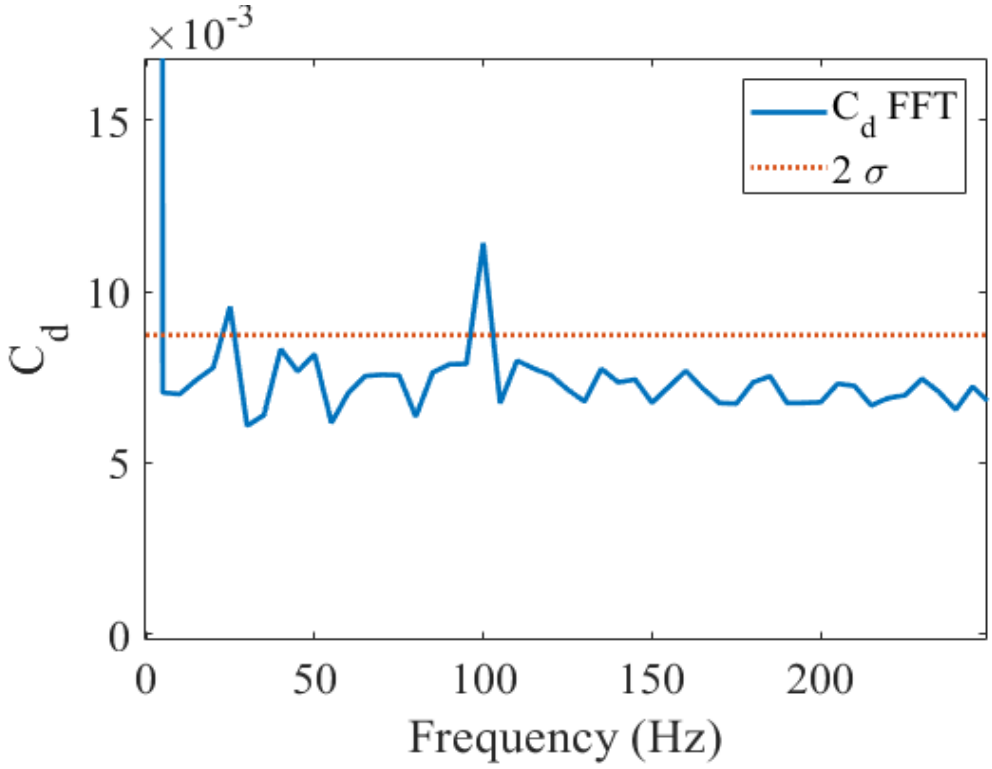

Figure 4.35: Frequency response of C_d for run 19

The frequency response for the pitching moment of run 19 is in Figure 4.36. Three peaks exceed the 2σ threshold, while only 1 of which is expected—at 100 Hz, with a relative magnitude of 13.1% compared to the 0 Hz value of 0.005. The other 2 are at 135 Hz and 165 Hz, with relative magnitudes of 7.8% and 7.4%, respectively; neither of which are a harmonic of 40 Hz, while the 40 Hz peak fails to meet the threshold. However, the overall 0 Hz value is so small, as expected for 0° angle of attack similar to the lift

coefficient, this is likely of no consequence, but is interesting in the unexpected placement of the peaks.

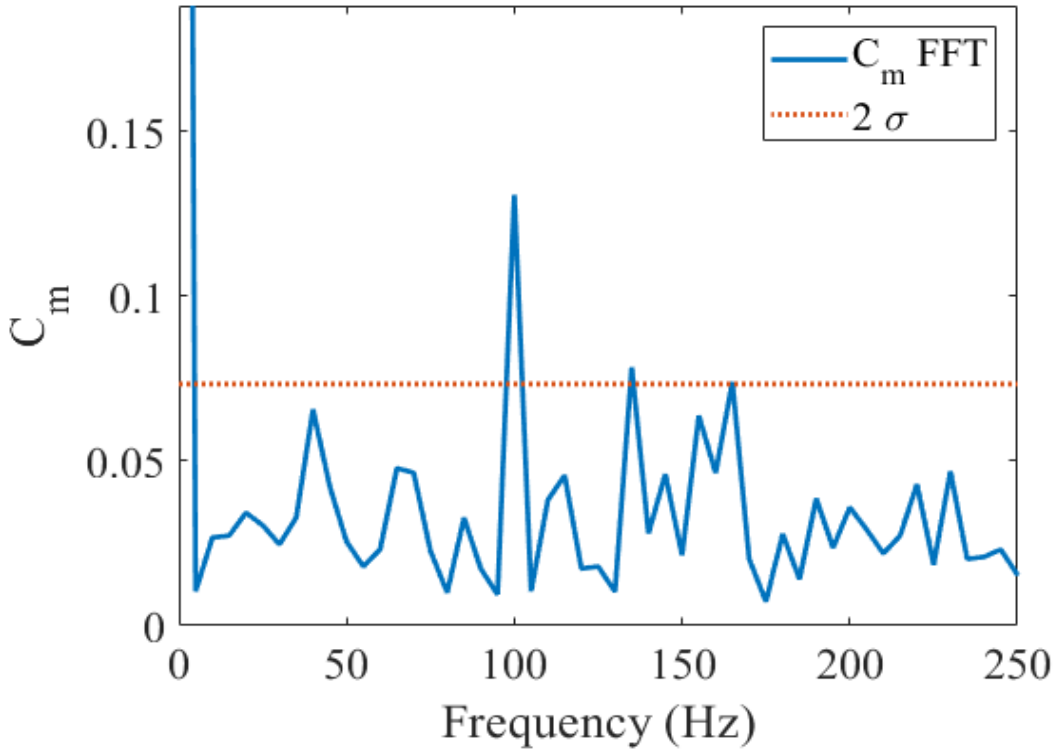

Figure 4.36: Frequency response of C_m for run 19

Moving along into the simulations with non-zero angles of attack, Figure 4.37 contains the lift coefficient frequency response for run 20. There are 3 peaks, at 25 Hz, 40 Hz, and 100 Hz, with relative magnitudes of 1.1%, 1.3%, and 2.1%, respectively, of the 0 Hz value of 0.071. The 25 Hz frequency is unexpected, as well as the lack of any harmonics. It should be noted, that if these data were notch filtered to remove the 40 Hz and 100 Hz components, it is likely the 25 Hz component would remain and could cause problems.

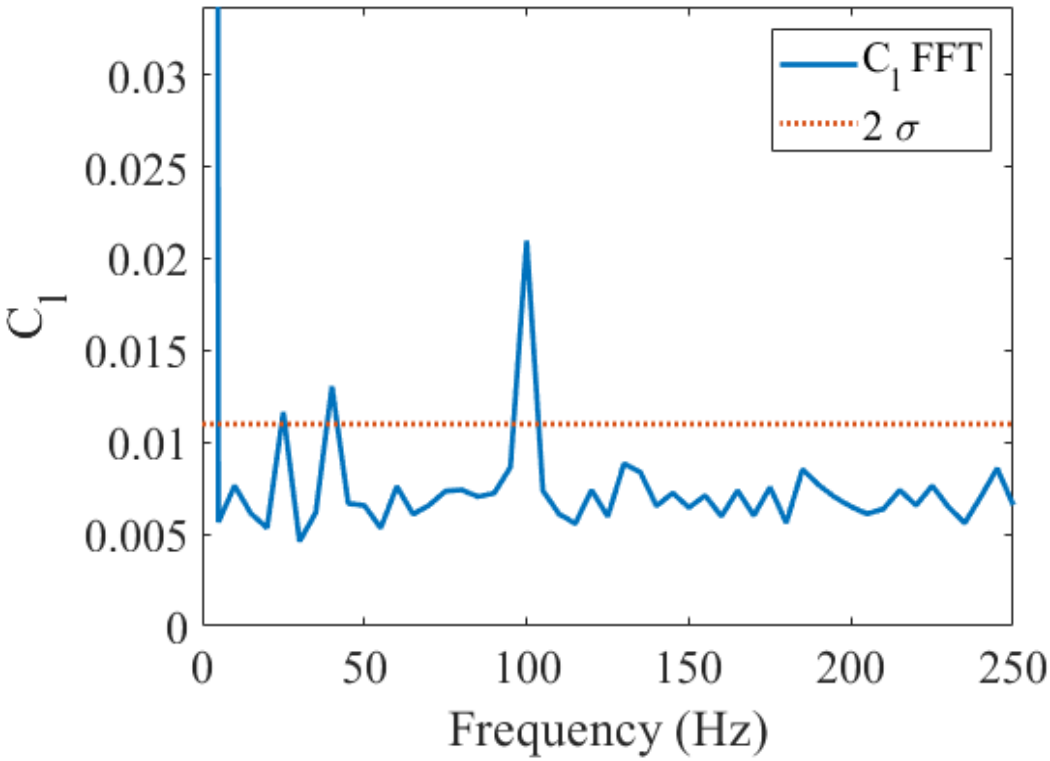

Figure 4.37: Normalized C_l in frequency domain for run 20

The drag coefficient frequency response for run 20 has similar frequency peaks, shown in Figure 4.38, except the 40 Hz component barely reaches the 2σ threshold. The relative magnitudes for these peaks are 0.9%, 0.86%, and 1.2%, respectively, compared to the 0 Hz value of 0.0753.

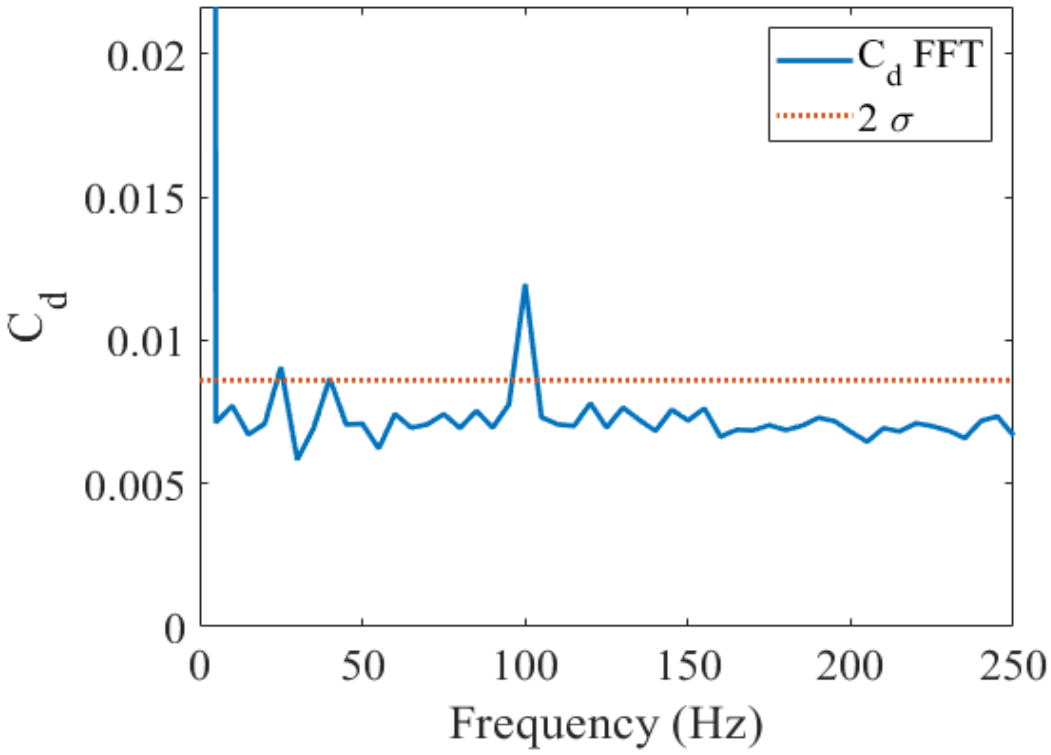

Figure 4.38: Normalized C_d in frequency domain for run 20

The pitching moment continues the same 3-peak trend, shown in Figure 4.39, with relative magnitudes of 1.5%, 1.4%, and 2.0%, respectively, compared to the 0 Hz value of 0.1564.

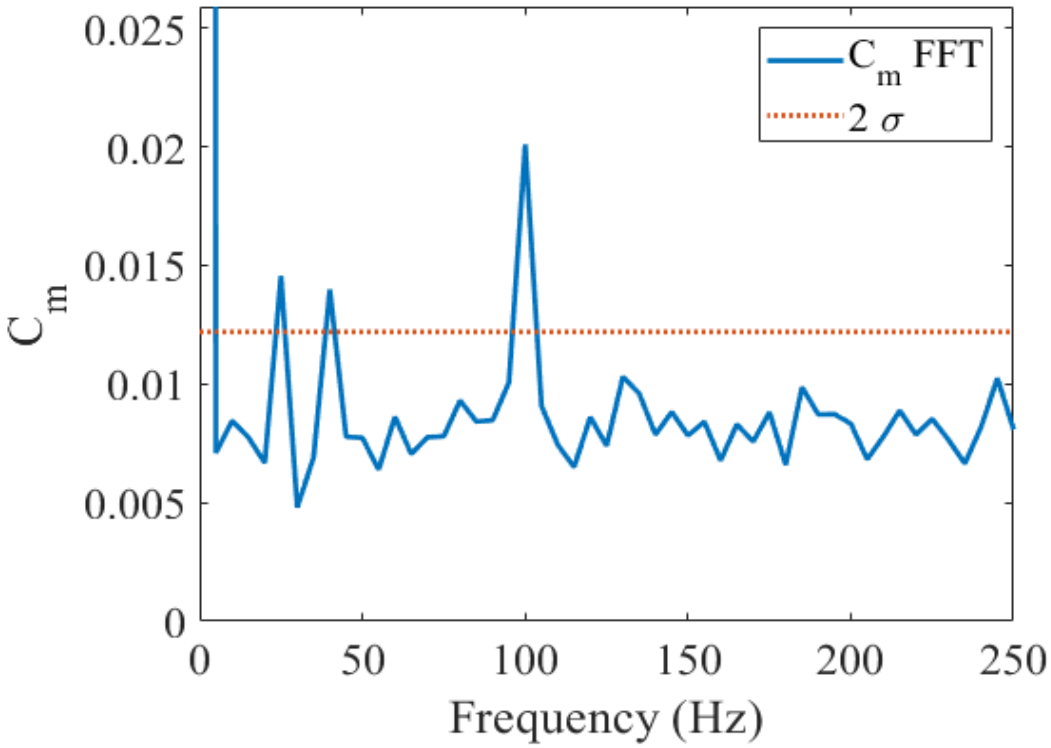

Figure 4.39: Normalized C_m in frequency domain for run 20

The 10° angle of attack cases are next, with the lift coefficient for run 21 in Figure 4.40. Here, the odd 25 Hz peak from run 20 is muted, as well as the 40 Hz peak barely reaching the 2σ threshold, at a relative magnitude of 1.0% compared to the 0 Hz value of 0.1528. The 100 Hz peak is relatively large, at 2.0% of the 0 Hz value.

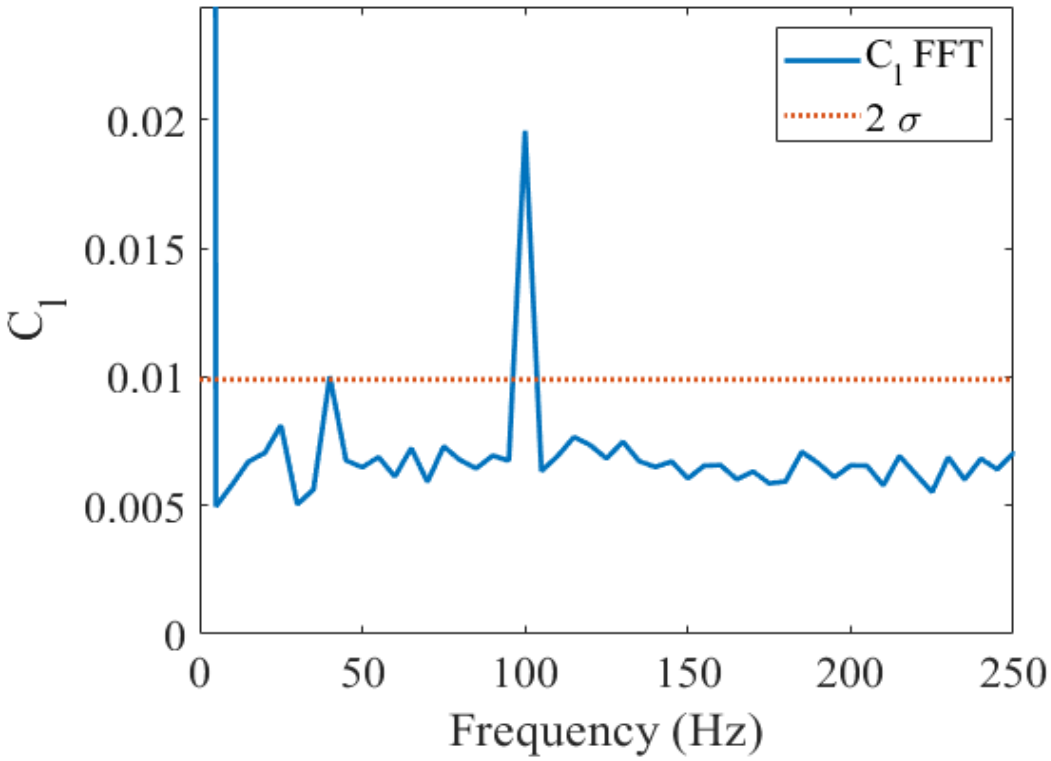

Figure 4.40: Normalized C_l in frequency domain for run 21

The drag coefficient frequency response is shown in Figure 4.41. Here, the 25 Hz peak has returned, while the 40 Hz peak barely meets the 2σ threshold, with relative magnitudes of 0.9% and 0.89%, respectively. The 100 Hz peak is the largest, at 1.4% of the 0 Hz value of 0.1075.

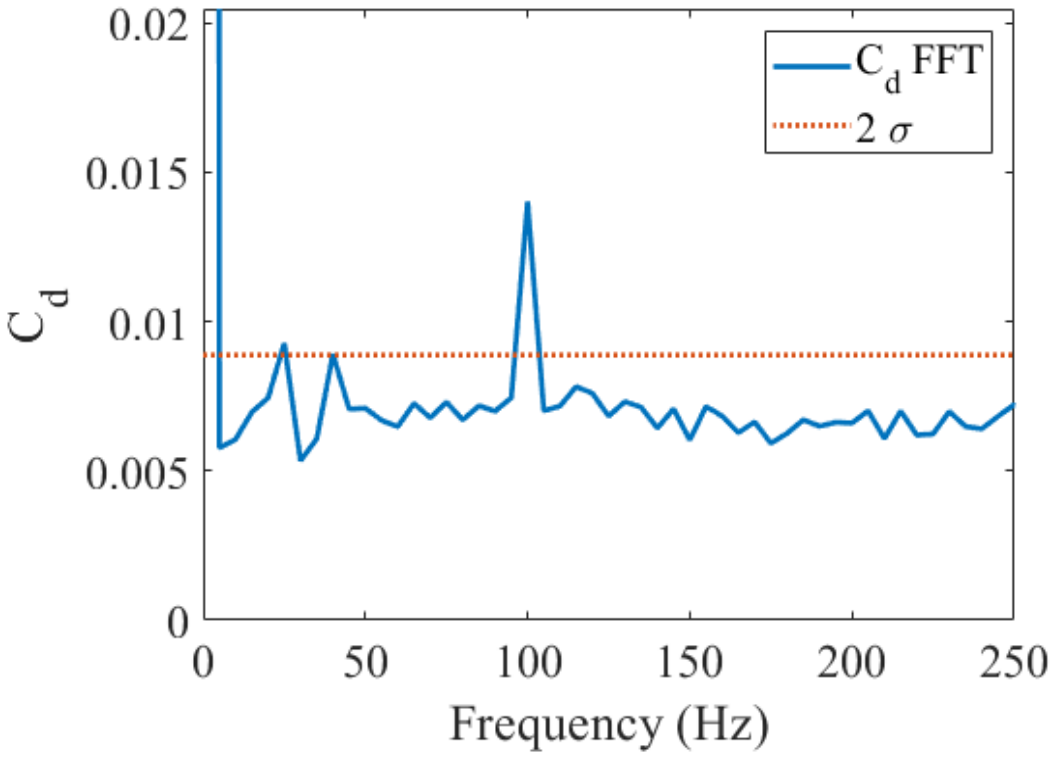

Figure 4.41: Normalized C_d in frequency domain for run 21

The pitching moment for run 21 is shown in Figure 4.42, where only one peak, at 100 Hz, exceeds the 2σ threshold. The relative magnitude of this peak is 1.9% of the 0 Hz value of 0.3402. Those under threshold, the 40 Hz peak is larger than the unexpected peak at 25 Hz.

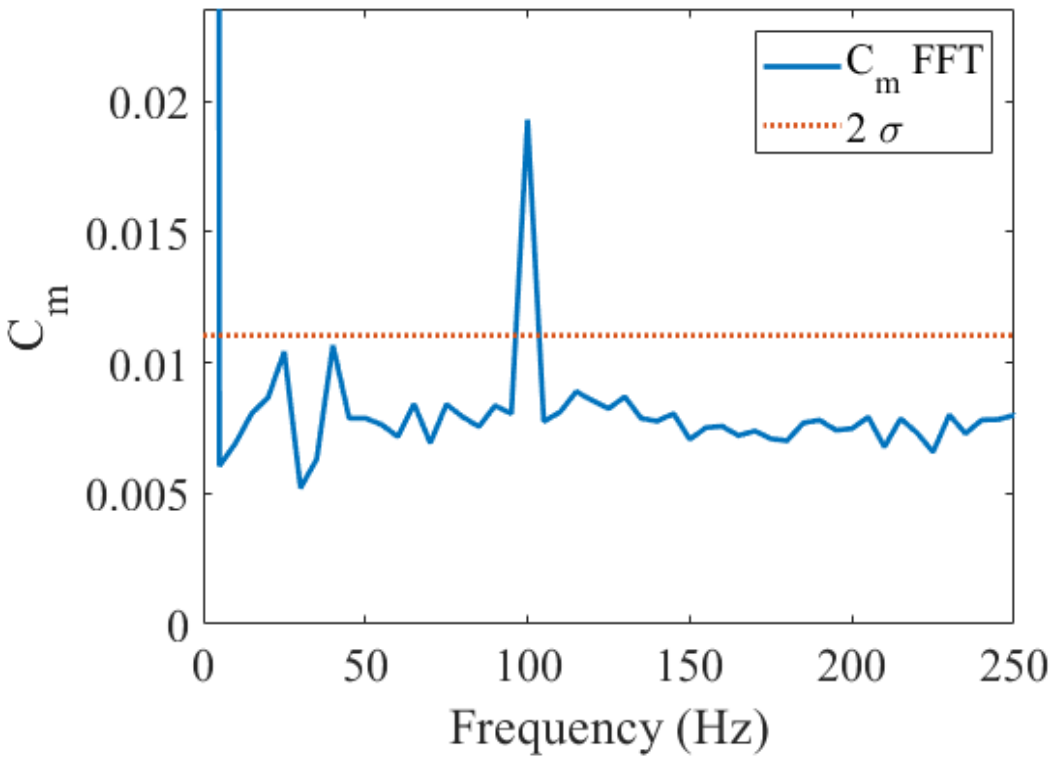

Figure 4.42: Normalized C_m in frequency domain for run 21

A comparison between run 21 and 25, which are the same except run 25 does not vibrate, is shown in Figure 4.43. This demonstrates the fact that the vibrational frequencies are not perfectly superimposed, particularly the 40 Hz tone, as it appears somewhat spread out over several frequency bins. Also, the 25 Hz peak is very slightly amplified such that it exceeds the 2σ threshold for C_d while it does not quite do so in the non-vibrating case.

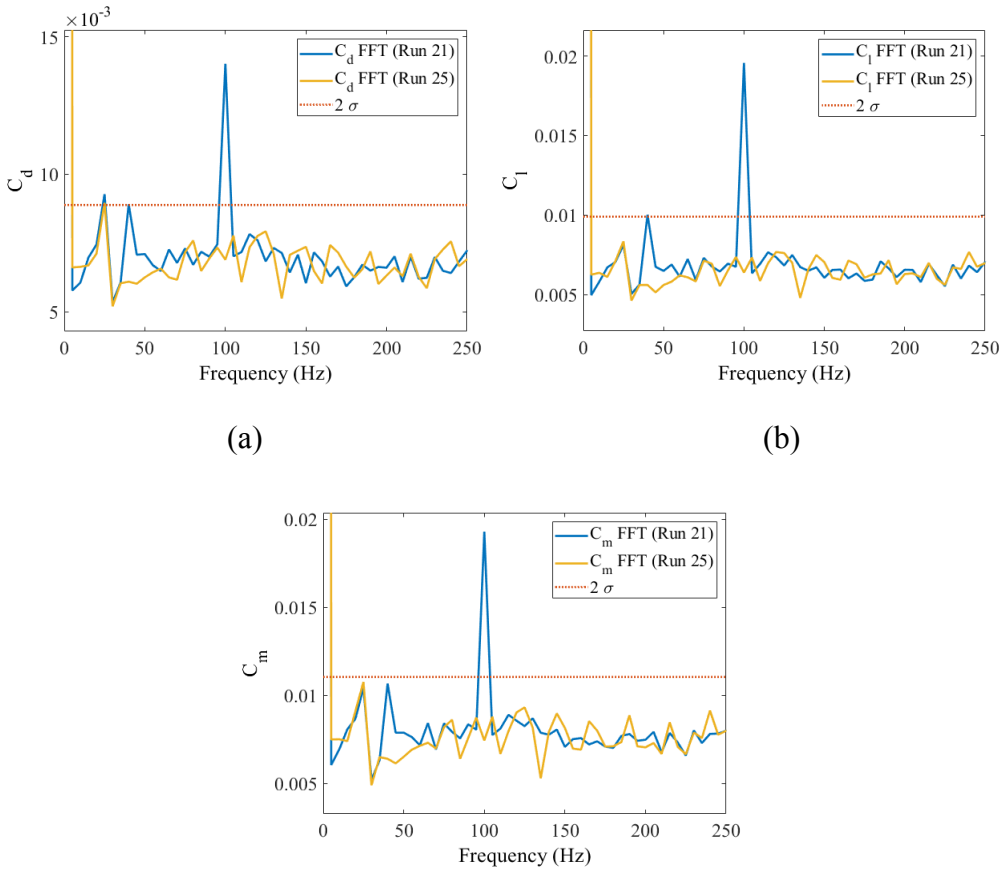

Figure 4.43: Comparison of the normalized (a) C_d, (b) C_l, and (c) C_m coefficients between runs 21 and 25, vibrating and non-vibrating, respectively

The highest angle of attack case, run 22, is next, with the frequency response of the lift coefficient in Figure 4.44. The 3 peaks return, again at 25 Hz, 40 Hz, and 100 Hz, with the relative magnitudes at 25 Hz and 40 Hz virtually identical at 1.1%, while the 100 Hz peak reaches 1.9% of the 0 Hz value of 0.2331

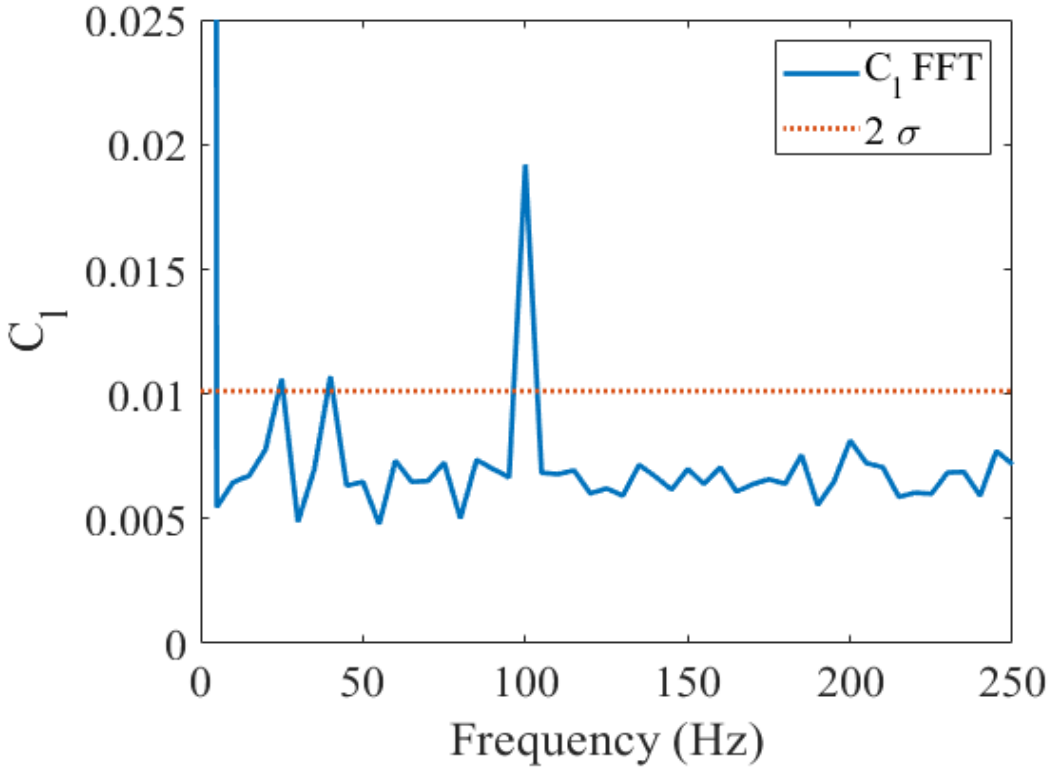

Figure 4.44: Normalized C_l in frequency domain for run 22

Figure 4.46 contains the frequency response of the drag coefficient for run 22. Here, the 25 Hz peak is again larger than the 40 Hz peak, while the 100 Hz peak dominates. The relative magnitudes are 1.1%, 0.97%, and 1.6%, respectively, compared to the 0 Hz value of 0.1654.

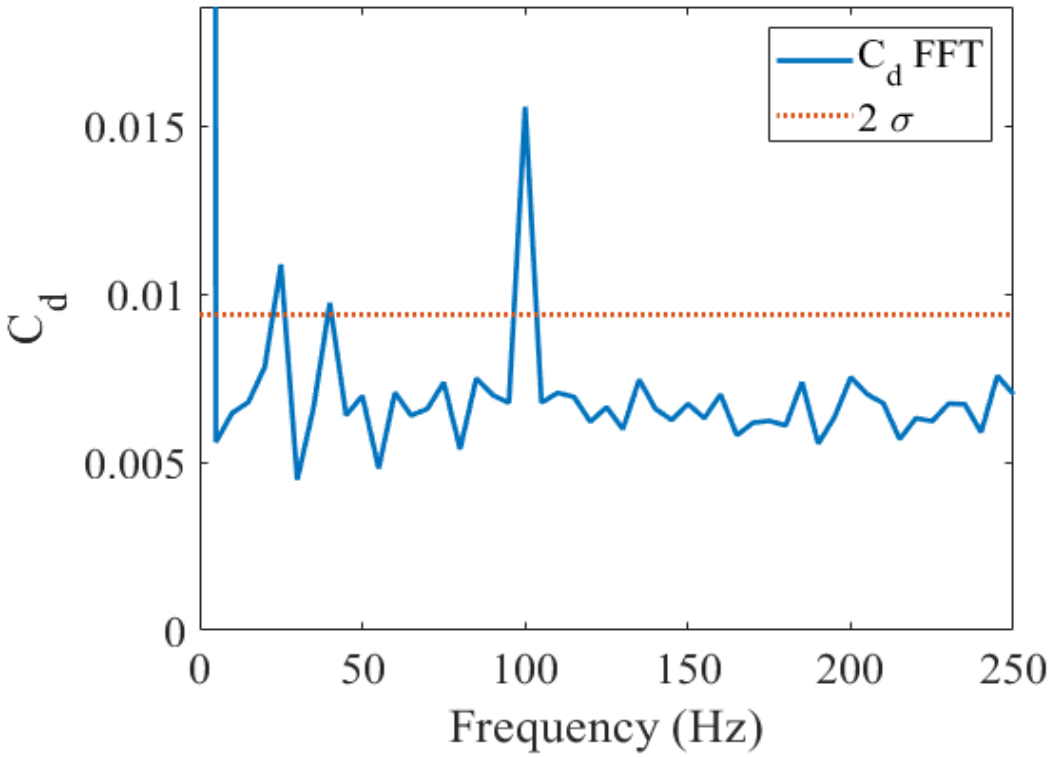

Figure 4.45: Normalized C_d in frequency domain for run 22

The pitching moment coefficient frequency response is shown in Figure 4.46. The 25 Hz peak is larger than the 40 Hz peak, at 1.3%, with the 40 Hz peak not even exceeding the 2σ threshold. The 100 Hz peak is again the largest, at 1.8% of the 0 Hz value of 0.5413.

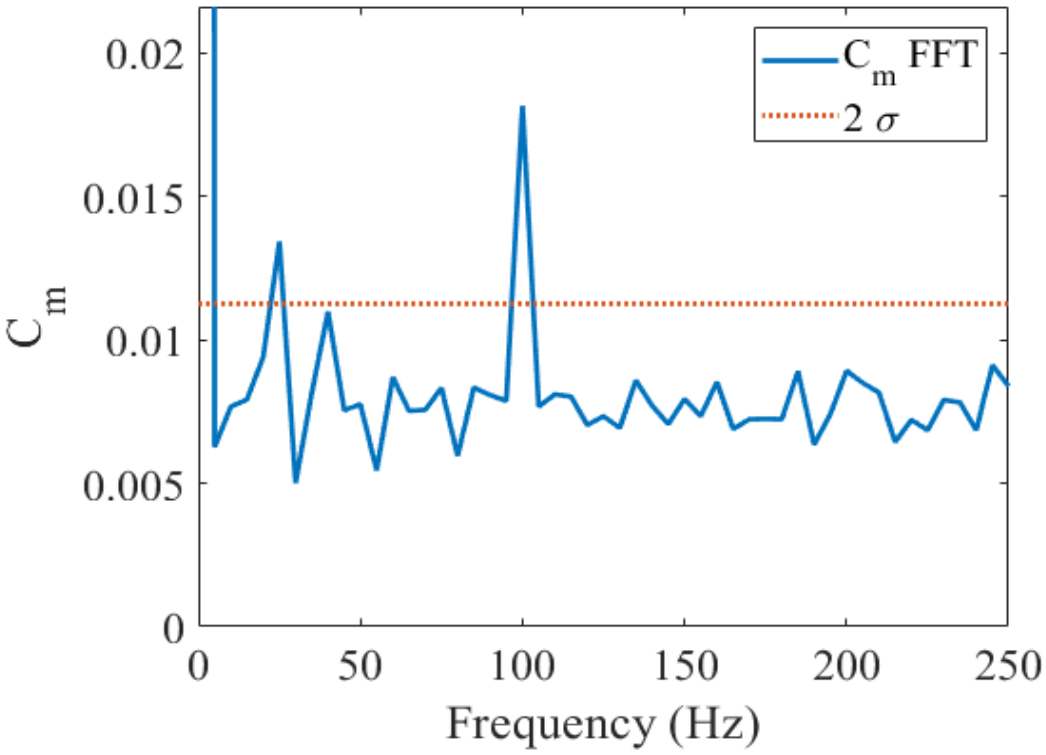

Figure 4.46: Normalized C_d in frequency domain for run 22

The case with a different cone half-angle of 15°, run 23, is next with the frequency response of the lift coefficient in Figure 4.47. Here, the 25 Hz peak has all but vanished, replaced by 2 smaller peaks at 30 Hz and 70 Hz. However, the only 2 to exceed the 2σ threshold are the expected peaks at 40 Hz and 100 Hz, with relative magnitudes of 1.0% and 1.9%, respectively, compared to the 0 Hz value of 0.1542.

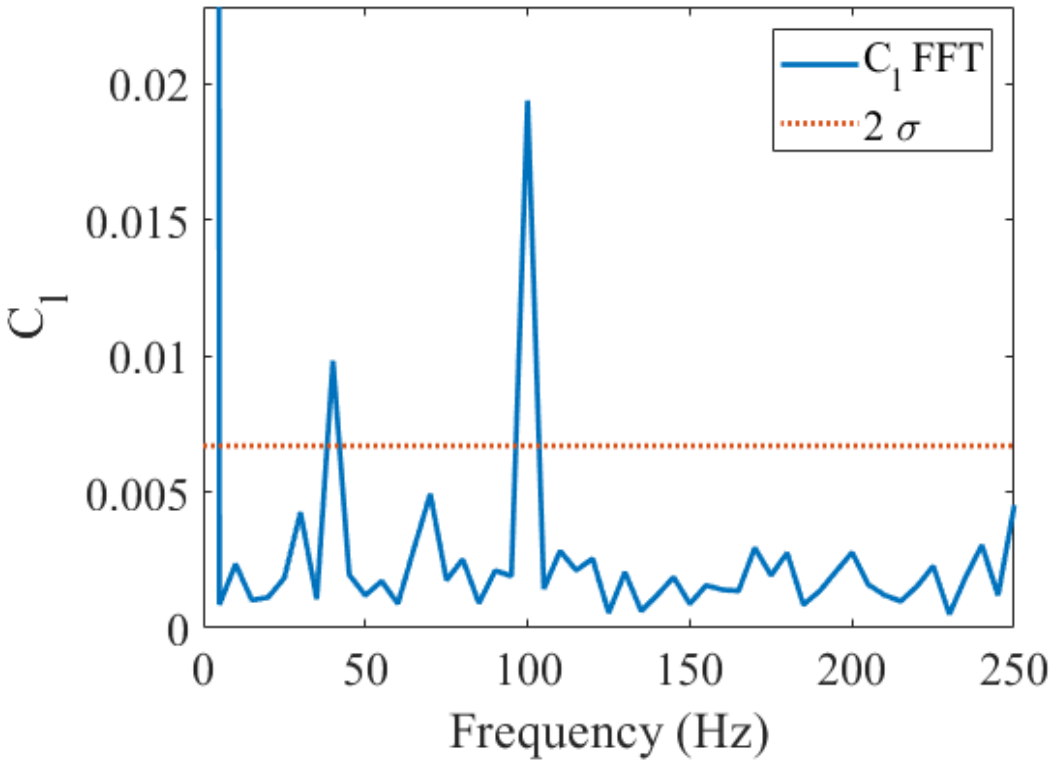

Figure 4.47: Normalized C_l in frequency domain for run 23

The drag coefficient frequency response for run 23 is shown in Figure 4.48. Here there are no discernible peaks outside those expected at 40 Hz and 100 Hz. The 40 Hz peak has a relative magnitude of 0.7% compared to the 0 Hz value of 0.267 while the 100 Hz peak stands at 1.3%.

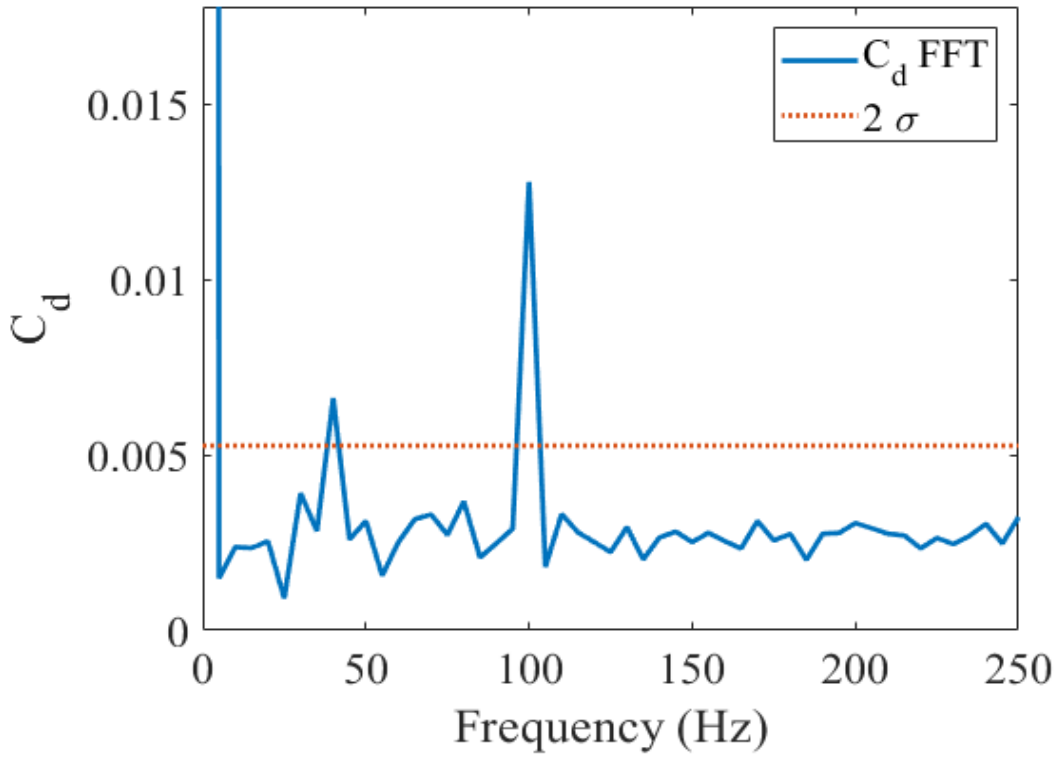

Figure 4.48: Normalized C_d in frequency domain for run 23

Figure 4.49 shows the pitching moment frequency response for run 23. The small peaks at 30 Hz and 70 Hz return, but do not exceed the 2σ threshold. The expected peaks at 40 Hz and 100 Hz have relative magnitudes of 0.9% and 1.8% compared to the 0 Hz value of 0.2466.

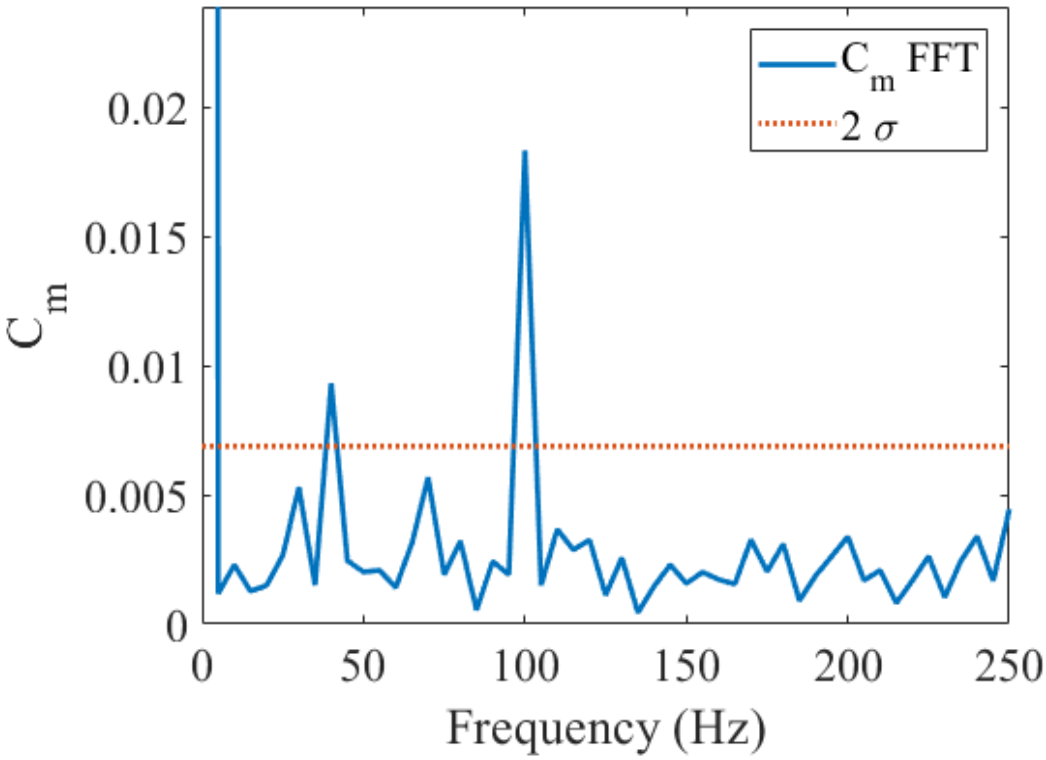

Figure 4.49: Normalized C_m in frequency domain for run 23

The final test case, run 24, returns to the 10° cone half-angle, with an angle of attack of 5°; it differs from run 20 in altitude only—20 km vice 30 km. Figure 4.50 contains the frequency response of the lift coefficient. Here, there are no discernible peaks outside the 2 expected peaks at 40 Hz and 100 Hz, which have relative magnitudes of 1.2% and 2.0% compared to the 0 Hz value of 0.071.

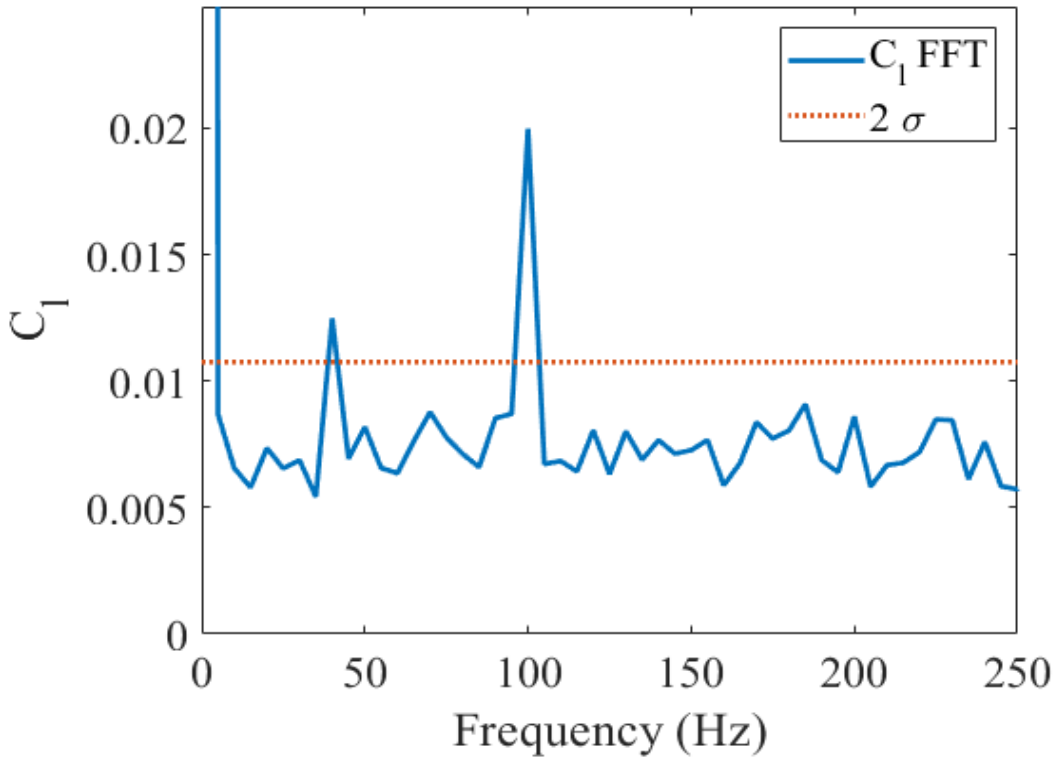

Figure 4.50: Normalized C_l in frequency domain for run 24

The plot for the drag coefficient frequency response is in Figure 4.51. Here, the 40 Hz peak barely meets the 2σ threshold, with a relative magnitude of 0.9%. The 100 Hz peak is the largest with a relative magnitude of 1.1% compared to the 0 Hz value of 0.0752.

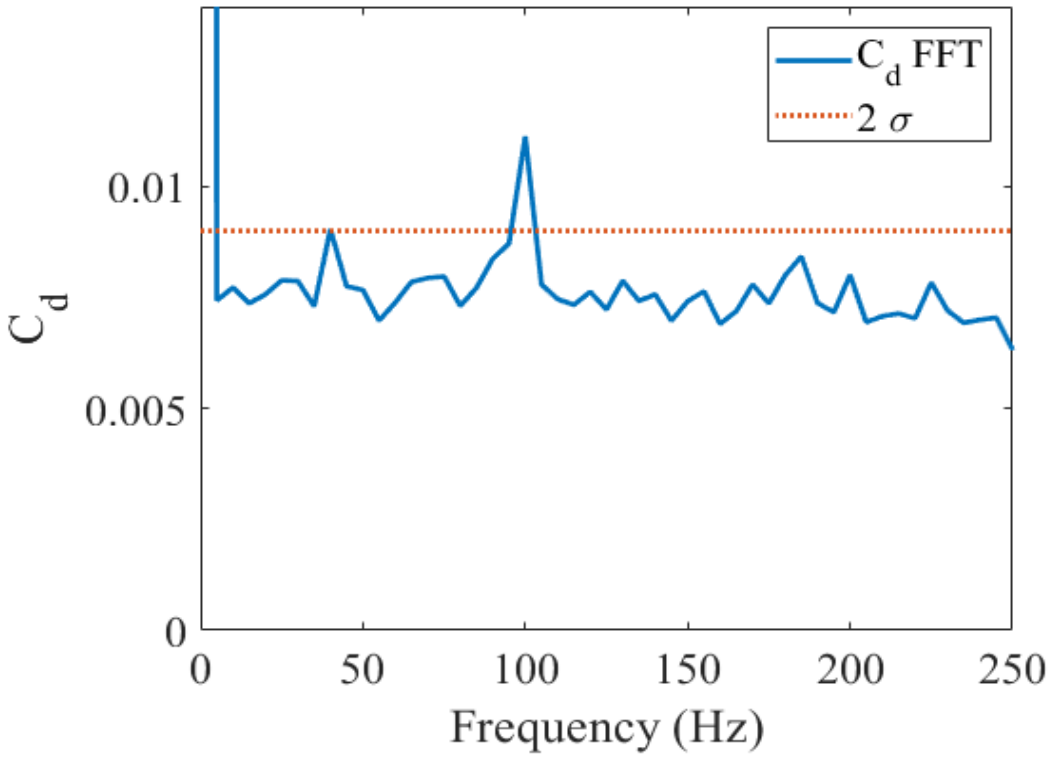

Figure 4.51: Normalized C_d in frequency domain for run 24

Finally, the pitching moment frequency response for run 24 is shown in Figure 4.52. Again, the only 2 discernible peaks occur at the expected 40 Hz and 100 Hz, with relative magnitudes of 1.3% and 2.0%, respectively, compared to the 0 Hz value of 0.1563.

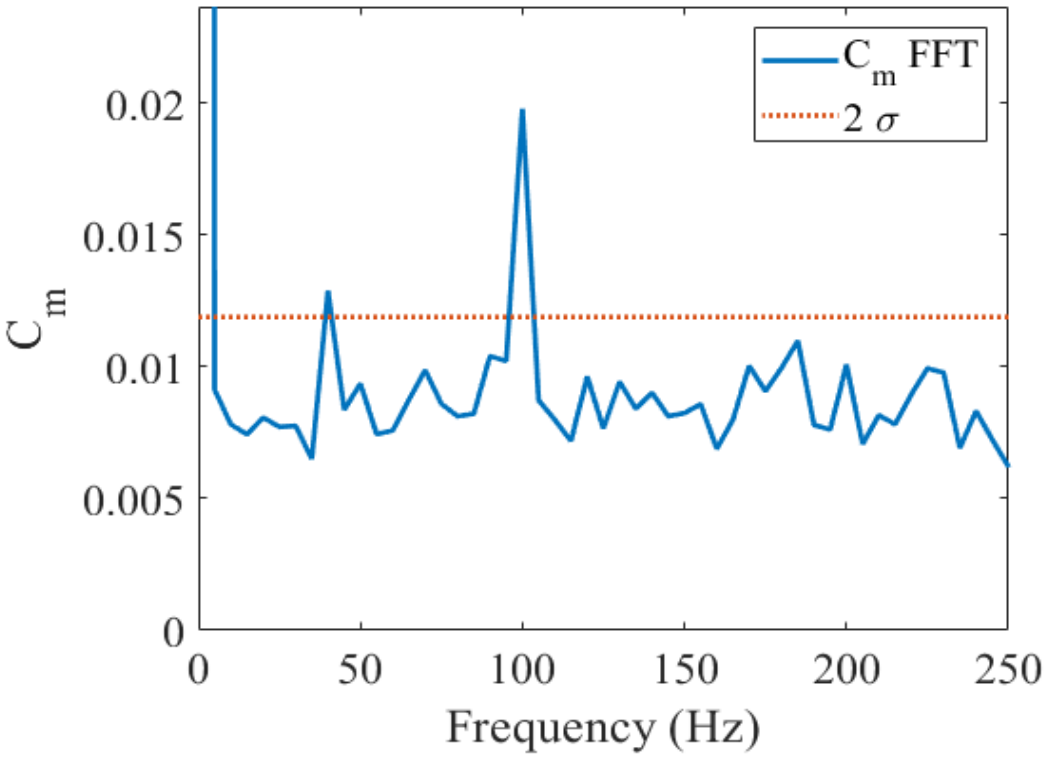

Figure 4.52: Normalized C_m in frequency domain for run 24

Figure 4.53 contains plots of all 6 runs overlaid in order to find any discernible trends. The most obvious trend is the 100 Hz peak is consistently the largest, even though it has a slightly smaller relative magnitude in the vibration implementation. A peak at 40 Hz is generally reliable, yet even though it is the largest frequency at which the model is vibrated, it does not always even exceed the 2σ threshold. Run 22, a 10° half-angle cone at 15° angle of attack, routinely displays the largest 25 Hz peak of unknown origin, which tends to diminish as the angle of attack decreases.

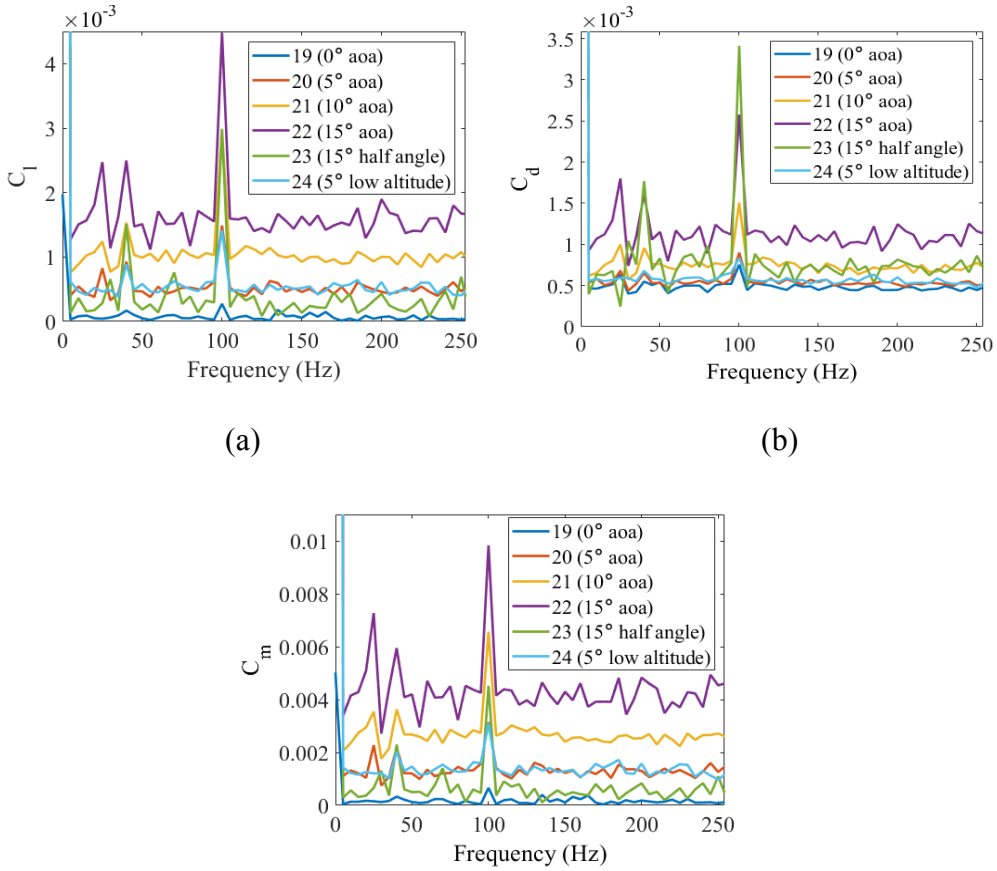

Figure 4.53: Frequency responses for all runs cases plotted together, including (a) lift coefficient, (b) drag coefficient, and (c) pitching moment

These data are all summarized in Table 4.18.

Table 4.18: Summary of vibrational test cases

Run #	Coefficient	Frequency Peak	% of 0 Hz value	0 Hz value
19	C_l	40	8.5	0.002
		100	13.8	
		135	9.0	
	C_d	25	1.1	0.6
		100	1.0	
	C_m	100	13.1	0.005

Run #	Coefficient	Frequency Peak	% of 0 Hz value	0 Hz value
		135	7.8	
		165	7.4	
20	C_l	25	1.1	0.071
		40	1.3	
		100	2.1	
	C_d	25	0.9	0.071
		40	0.86	
		100	1.2	
	C_m	25	1.5	0.1564
		40	1.4	
		100	2.0	
21	C_l	40	1.0	0.1528
		100	2.0	
	C_d	25	0.9	0.1075
		40	0.89	
		100	1.4	
	C_m	100	1.9	0.3402
22	C_l	25	1.1	0.2331
		40	1.1	
		100	1.9	
	C_d	25	1.1	0.1654
		40	0.97	
		100	1.6	
	C_m	25	1.3	0.5413
		100	1.8	
23	C_l	40	1.0	0.1542
		100	1.9	
	C_d	40	0.7	0.267
		100	1.3	
	C_m	40	0.9	0.2466
		100	1.8	

Run #	Coefficient	Frequency Peak	% of 0 Hz value	0 Hz value
24	C_l	40	1.2	0.071
		100	2.0	
	C_d	40	0.9	0.0752
		100	1.1	
	C_m	40	1.3	0.1563
		100	2.0	

4.6.1 Discussion

Some modeling artifact noise is expected with particle-based methods such as SPH, due to steady state not being fully achieved. In other words, in contrast to gridded codes where eventually steady state is achieved via the minute control volumes each reaching steady state, SPH and other particle-based methods are not guaranteed this due to an inherent instability, and unpredictability, in the particle movements throughout a simulation. This can be both good and bad; good because, to some degree, natural variance is modeled, as well as particles reliably finding their way around the body without much concern needed for body particle placement (vice a carefully constructed grid). However, it can be bad because, as evident in these plots and further exemplified in run 25, there is ever-present low-level white noise. This was the reason behind establishing the minimum threshold for a frequency component to be considered relevant.

All that said, with a threshold in place, it can be reasonably assumed if a frequency component exceeds the threshold, it is likely due to some physical phenomenon occurring in the flow—one of the main purposes of this research. The rest of this section will discuss trends observed in the data.

For runs 20-22, a 10° half-angle cone at 30 km altitude with varying angles of attack, a peak reliably occurs at 25 Hz. This is not likely a modeling artifact due to the fact that it vanishes for the other runs, particularly run 23 where the only change is the cone half-angle—the altitude, 30 km, and angle of attack, 5°, are identical to run 20. In addition, no other modeling processes operate at this frequency; a particle recycling routine operates at 500 Hz—well above any analyses conducted here. Also, even though the 25 Hz signal is somewhat present in the non-vibrating case (run 25) it is smaller, though only slightly, smaller than is present in the otherwise identical vibrating case. The author speculates this frequency component is due to an unexplained shifting and attenuation of the 40 Hz peak; this would also explain why the 40 Hz peak is consistently smaller than the 100 Hz due to some of the spectral power being spread across several frequencies. Further speculation explaining this low-frequency attenuation is that it could be due to how many particles the body interacts with at these velocities as a function of mean-free path; future work could vary the Mach number to see if this frequency shift and attenuation is affected.

Run 19 also has some interesting frequency peaks, particularly at 135 Hz and 165 Hz, even though the overall lift forces and pitching moments are small, their presence indicates oddities in the flow. Characteristics like these are important things to remember when designing an aircraft; theoretical physics and textbooks predict zero lift and pitching moment for symmetrical objects at 0° angle of attack, and while that may be the case when averaged over long periods, it is not necessarily true at all times during a

flight. Therefore, if the closed loop control system is not ready for regular, periodic perturbations in these forces and moments, control-induced oscillations can occur.

Another observation is found when comparing run 24 to run 20, where only altitude differ. Interestingly, the lower altitude case does not exhibit the same 25 Hz peak as found in run 20. It is possible the higher free-stream density provides a dampening of some sort.

A final, and universal, observation is the fact that the peak at 100 Hz is always the largest peak. This is notable because its magnitude component input into the body is only 95% that of the 40 Hz peak. It appears some type of unknown, low-frequency dampening occurs; again because no other modeling routines operate at this frequency. This is particularly shown when comparing run 21 and 25, where the peak nearest 40 Hz is somewhat spread over several frequency bins, with no corresponding peak in the non-vibrating case.

CHAPTER 5

CONCLUSIONS

Wind tunnel data is consistently plagued by noise, stemming from multiple sources, including sensor placement, data acquisition equipment and methods, and deflections of the sting holding the model in the test section. This latter source was the focus of this dissertation, wherein these deflections cause the model to vibrate within the wind tunnel, leading to different flow characteristics occurring over the body. The standard practice for experimentalists is to use notch filtering, also known as band-stop filtering, to remove fluctuations in wind tunnel data at these frequencies. It was hypothesized that these vibrations, which generally occur at the fundamental frequencies of the sting, cause the data to exhibit frequency components outside these specific frequencies, such that simply filtering them out does not entirely remove their effect.

This dissertation explores how mechanical vibrations that occur during wind tunnel testing impact the flow over the test model. A method to simulate the behavior was developed using smoothed particle hydrodynamics (SPH) which required extensive, and novel, physics-based modifications including: updated boundary conditions, an innovative switch for artificial viscosity and heating, methods to calculate forces and moments over a body, and methods to introduce vibrations upon boundaries.

Additionally, implementation-specific modifications were required in order to conduct longer runtimes necessary for the FFTs to function, including particle recycling and particle collimation. These modifications discussed in depth in Sections 3.2.2-3.2.6. This was accomplished by first verifying SPH for 2D and 3D hypersonic flow, and then extending the validation to accurately reproduce noisy wind tunnel data, thus validating the ability to vibrate a model within SPH. With confidence in the numerical model and post-processing of the results, this methodology was used to simulate a hypothetical vibrating model to investigate if these vibrations cause fundamental changes to the flow.

5.1 Summary of Main Results

Verification tests were performed against 2D oblique shock and axisymmetric conical shock exact solutions, comparing post-shock flow parameters, including temperature, pressure, density, velocity, Mach, and shock angle—a first for SPH-based solutions. The test suite included 7 compression corner cases, varying the angle of incidence, Mach, and working fluid, and 11 conical cases, varying the cone angle, Mach, and working fluid. The success threshold was defined to be an error less than 10% compared to theoretical values which was achieved in all but 2 cases: a 30° compression corner and a 20° cone at Mach 5 in CO_2. For most cases, the error for all parameters was less than 5%. The parameter with the highest likely error in a run was the shock angle, which is typical according to the literature for SPH-based external flow applications with shocks and is still an active area of research.

The SPH implementation was then verified for axi-symmetic conical flow, with 11 test cases varying cone half-angle, Mach number, and fluid against the Taylor-Maccoll numerical method where again the code matched the theoretical results within 10% for all cases. Generally, the results matched within 5% with the exception of shock angles for a 10° cone in M = 2 flow and a 5° cone in M = 5 flow.

To further exercise the code's capabilities, a convergence test was performed, varying the number of particles within the simulation. This effectively varied the resolution of the simulation, and is useful in determining a code's self-consistency and helps define the point of diminishing returns on particle density and runtime. The SPH implementation used was determined to have a convergence rate of 1.83 which is similar to the 1.4 rate found in literature [90] for other SPH-based implementations.

Validation was then performed against noisy wind tunnel data from Liu [7], where strain gauge readings were provided for axial force, normal force, and pitching moment. No recoverable frequencies were observed in the axial and normal forces in the data provided. However, the pitching moment data contained usable frequency information. It is typically assumed that the sting's frequency signature is simply superimposed upon the wind tunnel measurements and thus could be simply notch filtered out. However, this was shown not to be the case, where several more frequency components were present with varying amplitudes. We found 3 extra frequency components in the data, none of which were harmonics of the sting's vibrational signature, while the 2 primary sting frequencies were shifted and attenuated. However, the modeling methods developed using SPH were able to accurately reproduce the wind

tunnel data and validate the approach when vibrated accordingly, based on the data. The simulation data was then notch filtered according to the sting's signature and it was shown not all frequency components were removed. Together, this confirmed the dissertation's hypothesis that notch filtering at the sting's primary frequency nodes will not accurately remove the noise from the data, and that vibrations at hypersonic flow fundamentally change the flow, thus causing frequency components to be attenuated/amplified.

5.2 Detailed Result Regarding Vibrations in Hypersonic Flow

The results presented in Chapter 4 validated the hypothesis that a sting's vibrational modes are not simply superimposed upon the flow properties due to the presence of frequencies outside those input into the simulation showing up in the resulting data. This was proved via 2 methods. First by accurately reproducing the noisy data and then by analyzing a hypothetical sting and model system. These methods are discussed below.

First, in Section 4.5 wherein the dominate frequencies of the sting were not simply superimposed in the resulting data. While the sting vibrated at 2 primary frequencies, 39.7 Hz and 53.1 Hz, with the 39.7 Hz peak being slightly higher, the data did not reflect this. Instead, there was one dominate frequency closer to 42.8 Hz, with several smaller components. In fact, the model required 5 discrete frequencies—28.8 Hz, 43.2 Hz, 57.5 Hz, 79.2 Hz, and 115.0 Hz—in order to accurately match the raw wind tunnel data. This demonstrates there is some damping that occurs due to the hypersonic

flow itself which alters the amplitudes and frequencies superimposed in the data. Further, is was shown that simply notch filtering the data at the dominate sting frequencies did not remove all the resulting noise from the wind tunnel data and left harmonics at higher frequencies.

Second, in Section 4.6 with the ability to model vibrations validated, simulations were conducted with a surrogate model vibrating at 40 Hz and 100 Hz. Similar to the previous sections results, these vibrations were not directly superimposed upon the aerodynamics coefficients, again demonstrating a dampening effect within hypersonic flow. Specifically, frequencies as low as 25 Hz were shown, and as high as 135 Hz and 165 Hz appeared in the data, similar to how the raw wind tunnel data in the previous section contained frequencies well outside those of the sting. Furthermore, the amplitudes of the superimposed frequencies did not match those input into the model, with the 100 Hz peak consistently being the largest, even though it was only input into the model at 95% the strength of the 40 Hz node.

5.3 Research Achievements

The primary achievement of this research was proving the discontinuity between vibrations input into a hypersonic system, e.g. vibrations due to the mounting sting, and the vibrations occurring within the outputted data. System vibrations cause fundamental changes in hypersonic flow and the flow can either dampen certain vibrational nodes, as is the case in Section 4.6 where the 40 Hz inputted dominate frequency is greatly

attenuated, or shift/spread them to other frequencies, as demonstrated in both Sections 4.4 and 4.6.

A second achievement was to fully document the inability of filtering to remove all the expected noise within hypersonic results. As shown in Section 4.5, simply notch filtering the data does not remove all the inputted frequency nodes, as these were shifted and attenuated by the flow itself. These left-over frequency components could negatively impact the design of hypersonic control systems. If these frequencies are not taken into account during the design of the closed-loop algorithms—a control system fundamental frequency could be overlapped leading to control-induced oscillations. Furthermore, averaging the data, essentially a low-pass filter, could lead to bad conclusions if the data contains frequency components lower than are accurately captured within short wind tunnel experiments.

A final achievement of this research was the capability to model vibrations within fluid flow with the SPH model. Grid-based CFD codes lack in this capability without complicated workarounds and other particle-based methods to not appear to have fully developed this capability. With the ability to model vibrating and moving bodies in hypersonic flow, the door is opened to explore more complicated hypersonic geometries while being able to determine the flow characteristics without assuming a completely immobile vehicle. Furthermore, with the ability to simulate the actual wind tunnel vibrations and validate directly to the raw data, more rigorous agreement is established, thus the aerodynamic predictions can be better trusted. Additionally, since the

simulations are better validated against real data, more post-simulation modifications can be applied, such as removing the vibrations, or changing them, and trusting the results.

5.4 Problems overcome and outstanding issues and limitations

This research required several adjustments to the SPH method, some of which are new and novel. First, boundary conditions required the modifications listed in Section 3.2.2, which mostly focused on preventing fluid particles from penetrating walls. SPH excels at handling fluid-fluid interactions, but fluid-boundary interactions can not behave as expected, with fluid-penetration the primary errant behavior. This was elegantly solved via treating the fluid particles interacting with solid boundaries as elastic collisions.

Artificial viscosity required a modification, as explained in Section 3.2.3, in order to allow for high-shear situations, specifically when a fast-moving fluid particle is moving parallel to a static wall. This novel switch effectively turns off artificial viscosity unless the particles are expected to intersect within the next time step. This solution contrasts with other switches used in SPH artificial viscosity routines as most of them do not incorporate the volume carved out by a particle over a time-step.

The primary outstanding issue is the lack of available, raw wind tunnel data. It was quite difficult to find the small amount of noisy, raw wind tunnel data used in these analyses. Typically, wind tunnel experimenters provide only post-processed and filtered data to aircraft designers and CFD coders as that is what is typically requested by these consumers. However, given these analyses prove the filtered data may remove pivotal

data, this may change over time. Along these same lines, sting vibrational data is provided more often, however it is typically in human-readable form with all phase information lost from the Fast Fourier Transform. This makes it hard to reconstruct the time domain signal as done in Section 4.4.

One limitation that still exists in this SPH implementation is the relatively simple geometries that can be modeled. SPH can ingest any {x,y,z} particle lists. However, surface particles need accurate normal vectors computed a-priori for the force and moment calculations to work. That said, the limitation solely exists in the geometry generation rather than the method itself. Research was performed into using convex hulls to generate surface geometries. However, these did not tightly pack particles in such a way that fluid particles would not penetrate the surface. More sophisticated convex hull generators, or better surface normal estimation routines, would aid in alleviating this limitation.

5.5 Future Work

A goal for future investigation could be to further validate these approaches against more raw wind tunnel data. The methods presented in this dissertation could be further refined by applying them to more complicated vehicle geometries, longer run-time wind tunnel or flight test, and different flight regimes. This would drive SPH methods toward more accurately predicting hypersonic flow, to well within the 10% margin used in this work. Furthermore, these analyses could further uncover how hypersonic flow is altered in the presence of vibrations, develop theories and

mathematical models predicting said behaviors, and could even lead to advanced aircraft or missile designs that exploit these phenomena.

REFERENCES

[1] S. Batill, Experimental Uncertainty and Drag Measurements in the National Transonic Facility, University of Notre Dame, Notre Dame, Indiana, 1994. https://ntrs.nasa.gov/archive/nasa/casi.ntrs.nasa.gov/19940032438.pdf (accessed June 18, 2019).

[2] D. Yen, F. Bräuchle, Calibration and Uncertainty Analysis for the UC Davis Wind Tunnel Facility, (2000). https://research.engineering.ucdavis.edu/flight/wp-content/uploads/sites/33/2015/01/Calibration.pdf (accessed April 10, 2019).

[3] C.P. Young, R.D. Buehrle, S. Balakrishna, W.A. Kilgore, Effect of Vibration on Inertial Wind-Tunnel Model Attitude Measurement Devices, (1994).

[4] J.J. Bertin, Defining the Aerodynamic Environment, in: Hypersonic Aerothermodynamics, 3rd ed., AIAA, Washington, DC, 1994: pp. 87–155.

[5] J.D. Anderson Jr., Computational-Fluid-Dynamic Solutions of Hypersonic Viscous Flows, in: Hypersonic and High-Temperature Gas Dynamics, 2nd ed., American Institute of Aeronautics and Astronautics, Reston ,VA, 2006: pp. 415–445. https://doi.org/10.2514/4.861956.

[6] Z.-Y. Ye, Y.-J. Xie, J. Wu, The effects of wind-tunnel model vibration on flow field and aerodynamics of an airfoil, Gongcheng Lixue/Engineering Mechanics. 26 (2009) 240–245.

[7] Y. Liu, Y. Wang, C. Yuan, C. Luo, Z. Jiang, Aerodynamic force and moment measurement of 10° half-angle cone in JF12 shock tunnel, Chinese Journal of Aeronautics. 30 (2017) 983–987. https://doi.org/10.1016/j.cja.2017.02.008.

[8] A. Jirasek, R. Cummings, Assessment of Sting Effect on X-31 Aircraft Model Using CFD, in: 48th AIAA Aerospace Sciences Meeting Including the New Horizons Forum and Aerospace Exposition, American Institute of Aeronautics and Astronautics, Orlando, Florida, 2010. https://doi.org/10.2514/6.2010-1040.

[9] J.D. Anderson Jr., Some Preliminary Thoughts, in: Hypersonic and High-Temperature Gas Dynamics, 2nd ed., American Institute of Aeronautics and Astronautics, Reston ,VA, 2006: pp. 1–31. https://doi.org/10.2514/4.861956.

[10] T.A. Talay, INTRODUCTION TO THE AERODYNAMICS OF FLIGHT, NASA Langley Research Center, 1975. https://ntrs.nasa.gov/search.jsp?R=19760003955.

[11] J.J. Bertin, General Characterization of Hypersonic Flow, in: Hypersonic Aerotheromodynamics, 3rd ed., AIAA, Washington, DC, 1994: pp. 1–49.

[12] T. Barber, B. Maicke, J. Majdalani, Current State of High Speed Propulsion: Gaps, Obstacles and Technological Challenges in Hypersonic Applications, in: 45th AIAA/ASME/SAE/ASEE Joint Propulsion Conference & Exhibit, American Institute of Aeronautics and Astronautics, Denver, Colorado, 2009. https://doi.org/10.2514/6.2009-5118.

[13] M. Silla, V. Bertola, SPH simulation of oblique shocks in compressible flows: SPH Simulation of Oblique Shocks, Int. J. Numer. Meth. Fluids. 84 (2017) 494–505. https://doi.org/10.1002/fld.4356.

[14] B. Maicke, T. Barber, J. Majdalani, Evaluation of CFD Codes for Hypersonic Flow Modeling, in: 46th AIAA/ASME/SAE/ASEE Joint Propulsion Conference & Exhibit, American Institute of Aeronautics and Astronautics, Nashville, TN, 2010. https://doi.org/10.2514/6.2010-7184.

[15] D. Logan, Introduction, in: A First Course in the Finite Element Method, 5th ed., Cengage Learning, Stamford, CT, 2012: pp. 1–30.

[16] S. Patankar, Control-Volume Formulation, in: Numerical Heat Transfer and Fluid Flow, 1st ed., Taylor & Francis, 1980: pp. 25–40.

[17] H.K. Versteeg, W. Malalasekera, Introduction, in: Computational Fluid Dynamics: The Finite Volume Method, 2nd ed., Pearson Education Limited, Essex, England, 2007: pp. 1–8.

[18] S.R. De Groot, Non-equilibrium Thermodynamics, Corrected ed., Dover, New York, NY, 1984. http://cds.cern.ch/record/1986358.

[19] J.N. Moss, DSMC Simulations of Hypersonic Flows and Comparison With Experiments, in: AIP Conference Proceedings, AIP, Bari (Italy), 2005: pp. 547–552. https://doi.org/10.1063/1.1941593.

[20] M.A. Gallis, DSMC Simulations in Support of the STS-107 Accident Investigation, in: AIP Conference Proceedings, AIP, Bari (Italy), 2005: pp. 1211–1216. https://doi.org/10.1063/1.1941698.

[21] A.J. Barlow, P.-H. Maire, W.J. Rider, R.N. Rieben, M.J. Shashkov, Arbitrary Lagrangian–Eulerian methods for modeling high-speed compressible multimaterial flows, Journal of Computational Physics. 322 (2016) 603–665. https://doi.org/10.1016/j.jcp.2016.07.001.

[22] W. Boscheri, M. Dumbser, Arbitrary-Lagrangian–Eulerian Discontinuous Galerkin schemes with a posteriori subcell finite volume limiting on moving unstructured meshes, Journal of Computational Physics. 346 (2017) 449–479. https://doi.org/10.1016/j.jcp.2017.06.022.

[23] J. Donea, J.-P. Ponthot, A. Rodríguez-Ferran, Arbitrary Lagrangian-Eulerian Methods, in: E. Stein, R. de Borst, T.J.R. Hughes (Eds.), Encyclopedia of Computational Mechanics, John Wiley, Chichester, West Sussex, 2004: pp. 1–25.

[24] F. Duarte, R. Gormaz, S. Natesan, Arbitrary Lagrangian–Eulerian method for Navier–Stokes equations with moving boundaries, Computer Methods in Applied Mechanics and Engineering. 193 (2004) 4819–4836. https://doi.org/10.1016/j.cma.2004.05.003.

[25] R.A. Gingold, J.J. Monaghan, Smoothed particle hydrodynamics: theory and application to non-spherical stars, Monthly Notices of the Royal Astronomical Society. 181 (1977) 375–389. https://doi.org/10.1093/mnras/181.3.375.

[26] W. Jian, D. Liang, S. Shao, R. Chen, K. Yang, Smoothed Particle Hydrodynamics Simulations of Dam-Break Flows Around Movable Structures, International Journal of Offshore and Polar Engineering. 26 (2016). https://doi.org/10.17736/ijope.2016.ak08.

[27] P. Krištof, B. Beneš, J. Křivánek, O. Šťava, Hydraulic Erosion Using Smoothed Particle Hydrodynamics, Computer Graphics Forum. 28 (2009) 219–228. https://doi.org/10.1111/j.1467-8659.2009.01361.x.

[28] C. Altomare, G. Viccione, B. Tagliafierro, V. Bovolin, J.M. Domínguez, A.J.C. Crespo, Free-Surface Flow Simulations with Smoothed Particle Hydrodynamics Method using High-Performance Computing, in: A. Ionescu (Ed.), Computational Fluid Dynamics - Basic Instruments and Applications in Science, InTech, Rijeka, Croatia, 2018: pp. 73–100. https://doi.org/10.5772/intechopen.71362.

[29] P.K. Koukouvinis, J.S. Anagnostopoulos, D.E. Papantonis, T.E. Simos, G. Psihoyios, Ch. Tsitouras, Turbulence Modeling in Smoothed Particle Hydrodynamics Methodology: Application in Nozzle Flow, in: AIP Conference Proceedings, AIP, Rethymno, Crete (Greece), 2009: pp. 248–251. https://doi.org/10.1063/1.3241439.

[30] D. Liang, W. Jian, S. Shao, R. Chen, K. Yang, Incompressible SPH simulation of solitary wave interaction with movable seawalls, Journal of Fluids and Structures. 69 (2017) 72–88. https://doi.org/10.1016/j.jfluidstructs.2016.11.015.

[31] M.A. Rodriguez, J.T. Cassibry, A 3-D Smoothed-Particle Hydrodynamics Model of Electrode Erosion, IEEE Transactions on Plasma Science. 45 (2017) 3030–3037. https://doi.org/10.1109/TPS.2017.2760349.

[32] A. Pazouki, D. Negrut, A High Performance Computing (HPC) approach to the Smoothed Particle Hydrodynamics (SPH) method, 2013. https://www.researchgate.net/publication/326920918_A_High_Performance_Computing_HPC_approach_to_the_Smoothed_Particle_Hydrodynamics_SPH_method.

[33] T. Harada, S. Koshizuka, Y. Kawaguchi, Improvement in the Boundary Conditions of Smoothed Particle Hydrodynamics, (2007). https://pdfs.semanticscholar.org/c5d3/563df05010044694d5c22b75d19690f5de8d.pdf (accessed February 8, 2019).

[34] S.-Q. Jin, X. Zheng, W.-Y. Duan, K.-N. Niu, A New Boundary Treatment Method for Smoothed Particle Hydrodynamics, Procedia Engineering. 126 (2015) 655–659. https://doi.org/10.1016/j.proeng.2015.11.256.

[35] S. Adami, X.Y. Hu, N.A. Adams, A generalized wall boundary condition for smoothed particle hydrodynamics, Journal of Computational Physics. 231 (2012) 7057–7075. https://doi.org/10.1016/j.jcp.2012.05.005.

[36] A. Leroy, D. Violeau, M. Ferrand, C. Kassiotis, Unified semi-analytical wall boundary conditions applied to 2-D incompressible SPH, Journal of Computational Physics. 261 (2014) 106–129. https://doi.org/10.1016/j.jcp.2013.12.035.

[37] D.L. Amdahl, Modeling Aerodynamic Problems Using Smoothed Particle Hydrodynamics (SPH), in: Aerotech 1993, SAE International, Cosa Mesa, CA, 1993. https://doi.org/10.4271/932512.

[38] D. Peckham, Exploratory Tests on Sting Interference at a Mach Number of 6.8, Ministry of Aviation, London, UK, 1960.

[39] G. Pick, Sting Effects in Hypersonic Base Pressure Measurements, Naval Ship Research and Development Center, Bethesda, MD, 1971.

[40] D.G. Mobey, Flow Unsteadiness and Model Vibration in Wind Tunnels at Subsonic and Transonic Speeds by, Ministry of Aviation Supply, London, UK, 1970.

[41] J.P. Billingsley, Sting Dynamics of Wind Tunnel Models, Arnold Engineering Development Center, Arnold AFB, TN, 1976.

[42] J.P. Reding, L.E. Ericsson, Dynamic Support Interference, Journal of Spacecraft and Rockets. 9 (1972) 547–553. https://doi.org/10.2514/3.61738.

[43] L.E. Ericsson, J.P. Reding, Transonic Sting Interference, Journal of Spacecraft and Rockets. 17 (1980) 140–144. https://doi.org/10.2514/3.57720.

[44] L.E. Ericsson, J.P. Reding, Viscous Interaction or Support Interference-The Dynamicst's Dilemma, AIAA Journal. 16 (1978) 363–368. https://doi.org/10.2514/3.60898.

[45] W.B. Igoe, F.J. Capone, Reduction of Wind-Tunnel-Model Vibration by Means of a Tuned Damped Vibration Absorber Installed in the Model, NASA Langley Research Center, Washington, DC, 1968. https://ntrs.nasa.gov/archive/nasa/casi.ntrs.nasa.gov/19680019334.pdf.

[46] Y. He, S. Zhao, D. Li, T. Li, Active vibration control of support sting in wind tunnel by using adaptive method, Vibroengineering PROCEDIA. 14 (2017) 151–156. https://doi.org/10.21595/vp.2017.19037.

[47] X. Shen, Y. Dai, M. Chen, L. Zhang, L. Yu, Active Vibration Control of the Sting Used in Wind Tunnel: Comparison of Three Control Algorithms, Shock and Vibration. 2018 (2018) 1–10. https://doi.org/10.1155/2018/1905049.

[48] T.A. Barber, A Survey of Gaps, Obstacles, and Technical Challenges for Hypersonic Applications, Master's Thesis, University of Tennessee Knoxville, 2012. https://trace.tennessee.edu/utk_gradthes/1131.

[49] P. Šidlof, V. Vlček, M. Štěpán, J. Horáček, M. Luxa, D. Šimurda, J. Kozánek, Wind Tunnel Measurements of Flow-Induced Vibration of a NACA0015 Airfoil Model, (2014) V004T04A029. https://doi.org/10.1115/PVP2014-28294.

[50] P. Sidlof, CFD simulation of flow-induced vibration of an elastically supported airfoil, in: EDP Sciences, 2016. https://doi.org/10.1051/epjconf/201611402105.

[51] D.J. Price, Smoothed particle hydrodynamics and magnetohydrodynamics, Journal of Computational Physics. 231 (2012) 759–794. https://doi.org/10.1016/j.jcp.2010.12.011.

[52] C. Wingate, W. Miller, Workshop on Advances in Smooth Particle Hydrodynamics, Los Alamos National Laboratory, Los Alamos, CA, 1993.

[53] J.J. Monaghan, An Introduction to SPH, Computer Physics Communications. 48 (1988) 89–96.

[54] D. Price, Smoothed Particle Hydrodynamics in Numerical Cosmology, (2012). http://users.monash.edu.au/~dprice/talks/price_nc2012.pdf (accessed January 2, 2019).

[55] D. Price, Smoothed Particle Hydrodynamics, (2013). https://app.spheric-sph.org/sites/spheric/files/Price_keynote_SPHERIC_2013.pdf (accessed May 5, 2019).

[56] A. Cartwright, D. Stamatellos, Controlling artificial viscosity in smoothed particle hydrodynamics simulations of accretion disks, Astronomy and Astrophysics. 516 (2010) A99. https://doi.org/10.1051/0004-6361/201014466.

[57] B. Moylan, Raindrop Demise in a High-Speed Projectile Flowfield, PhD Dissertation, University of Alabama in Huntsville, 2010.

[58] R.F. Stellingwerf, Smooth Particle Hydrodynamics Code Wind-Tunnel Modeling Capability, (2010).

[59] J.J. Monaghan, Smoothed particle hydrodynamics, Reports on Progress in Physics. 68 (2005) 1703–1759. https://doi.org/10.1088/0034-4885/68/8/R01.

[60] J.J. Monaghan, R.A. Gingold, Shock simulation by the particle method, Journal of Computational Physics. 52 (1983) 374–389.

[61] G.R. Liu, M.B. Liu, SPH for General Dynamic Fluid Flows, in: Smoothed Particle Hydrodynamics: A Meshfree Particle Method, World Scientific Publishing, Toh Tuck Link, Singapore, 2009: pp. 103–176.

[62] V. Springel, C.P. Dullemond, Classic Hydrodynamic Solvers, (2012). http://www.ita.uni-heidelberg.de/~dullemond/lectures/num_fluid_2011/index.shtml (accessed January 30, 2019).

[63] J.J. Monaghan, Smoothed Particle Hydrodynamics, Journal of Astronomy and Astrophysics. 30 (1992) 543–573.

[64] S.J. Watkins, A.S. Bhattal, N. Francis, J.A. Turner, A.P. Whitworth, A new prescription for viscosity in Smoothed Particle Hydrodynamics, Astronomy and Astrophysics. 119 (1996) 177–187. https://doi.org/10.1051/aas:1996104.

[65] J.P. Morris, J.J. Monaghan, A Switch to Reduce SPH Viscosity, Journal of Computational Physics. 136 (1997) 41–50. https://doi.org/10.1006/jcph.1997.5690.

[66] P.A. Taylor, J.C. Miller, Measuring the Effects of Artificial Viscosity in SPH Simulations of Rotating Fluid Flows, Monthly Notices of the Royal Astronomical Society. 426 (2012) 1687–1700. https://doi.org/10.1111/j.1365-2966.2012.21747.x.

[67] L. Cullen, W. Dehnen, Inviscid SPH, Monthly Notices of the Royal Astronomical Society. 408 (2010) 669–683. https://doi.org/10.1111/j.1365-2966.2010.17158.x.

[68] J.I. Read, T. Hayfield, SPHS: Smoothed Particle Hydrodynamics with a higher order dissipation switch, Monthly Notices of the Royal Astronomical Society. 422 (2012) 3037–3055. https://doi.org/10.1111/j.1365-2966.2012.20819.x.

[69] G. Fourtakas, B.D. Rogers, Modelling multi-phase liquid-sediment scour and resuspension induced by rapid flows using Smoothed Particle Hydrodynamics (SPH) accelerated with a Graphics Processing Unit (GPU), Advances in Water Resources. 92 (2016) 186–199. https://doi.org/10.1016/j.advwatres.2016.04.009.

[70] M. Kelager, Lagrangian Fluid Dynamics using Smoothed Particle Hydrodynamics, Master's Thesis, University of Copenhagen, 2006.

[71] R. Tomasi, Smoothed Particle Hydrodynamics, (2015). http://www.mathematik.uni-muenchen.de/~diening/ws14/huette/vortraege/tomasi.pdf (accessed April 4, 2019).

[72] T. Weaver, Z. Xiao, Fluid Simulation by the Smoothed Particle Hydrodynamics Method: A Survey:, in: Proceedings of the 11th Joint Conference on Computer Vision, Imaging and Computer Graphics Theory and Applications, SCITEPRESS - Science and and Technology Publications, Rome, Italy, 2016: pp. 213–223. https://doi.org/10.5220/0005673702130223.

[73] J.M. Domínguez, A.J.C. Crespo, M. Gómez-Gesteira, Optimization strategies for parallel CPU and GPU implementations of a meshfree particle method, ArXiv. (2011).

[74] A. Hérault, S. di Catania, G. Bilotta, R.A. Dalrymple, SPH on GPU with CUDA, Journal of Hydraulic Research. 48 (2010) 74–79. https://doi.org/doi:10.3826/jhr.2010.0005.

[75] CUDA C Programming Guide, (2019). https://docs.nvidia.com/cuda/pdf/CUDA_C_Programming_Guide.pdf.

[76] A.D. Chow, B.D. Rogers, S.J. Lind, P.K. Stansby, Incompressible SPH (ISPH) with fast Poisson solver on a GPU, Computer Physics Communications. 226 (2018) 81–103. https://doi.org/10.1016/j.cpc.2018.01.005.

[77] A.D. Chow, B.D. Rogers, S.J. Lind, P.K. Stansby, Numerical wave basin using incompressible smoothed particle hydrodynamics (ISPH) on a single GPU with vertical cylinder test cases, Computers & Fluids. 179 (2019) 543–562. https://doi.org/10.1016/j.compfluid.2018.11.022.

[78] A. Pazouki, R. Serban, D. Negrut, A High Performance Computing Approach to the Simulation of Fluid-Solid interaction Problems with Rigid and Flexible Components, Archive of Mechanical Engineering. 61 (2014) 227–251. https://doi.org/10.2478/meceng-2014-0014.

[79] G. Buresti, A note on Stokes' hypothesis, Acta Mech. 226 (2015) 3555–3559. https://doi.org/10.1007/s00707-015-1380-9.

[80] J.D. Anderson Jr., Hypersonic Flow, in: Modern Compressible Flow: With Historical Perspective, 3rd ed., McGraw-Hill Higher Education, New York, NY, 2003: pp. 547–584.

[81] T.J. Englestad, J.T. Cassibry, Investigations of a Novel Boundary Condition Approach for the Accurate Prediction of Hypersonic Oblique Shocks in Mesh-free Lagrangian Simulations, Aerospace Science and Technology. under review (2019).

[82] W.F. Noh, Errors for calculations of strong shocks using an artificial viscosity and an artificial heat flux, Journal of Computational Physics. 72 (1987) 78–120. https://doi.org/10.1016/0021-9991(87)90074-X.

[83] J.D. Anderson, Oblique Shock and Expansion Waves, in: Fundamentals of Aerodynamics, 5th ed., McGraw-Hill, New York, NY, 2011: pp. 601–668.

[84] D.H. Peckham, Experiments at Hypersonic Speeds on Circular Cones at Incidence, Ministry of Aviation Aeronautical Research Council. 702 (1965) 36.

[85] J.D. Anderson, Introduction to Numerical Techniques for Nonlinear Supersonic Flow, in: Fundamentals of Aerodynamics, 5th ed., McGraw-Hill, New York, NY, 2011: pp. 797–838.

[86] K. Schillo, J. Cassibry, M. Rodriguez, S. Thompson, Suite for Smooth Particle Hydrodynamic Code Relevant to Spherical Plasma Liner Formation and Implosion, ASME J of Nuclear Rad Sci. 5 (2019) 042201. https://doi.org/10.1115/1.4042710.

[87] K.J. Schillo, Three-Dimensional Modeling of Fusion Yield in Plasma Jet-Driven Magneto-Intertial Fusion, PhD Dissertation, University of Alabama in Huntsville, 2019.

[88] L. Jackson, Three-Dimensional Model of a Plasma Railgun using Smoothed Particle Hydrodynamics, Master's Thesis, University of Alabama in Huntsville, 2014.

[89] P.W. Cleary, J.J. Monaghan, Conduction Modelling Using Smoothed Particle Hydrodynamics, Journal of Computational Physics. 148 (1999) 227–264. https://doi.org/10.1006/jcph.1998.6118.

[90] Q. Zhu, L. Hernquist, Y. Li, Numerical Convergence in Smoothed Particle Hydrodynamics, ApJ. 800 (2015) 6. https://doi.org/10.1088/0004-637X/800/1/6.

[91] K. Champion, M. Dubin, A. Hull, U.S. Standard Atmosphere 1976, National Oceanic and Atmospheric Administration, Washington, DC, 1976. https://ntrs.nasa.gov/archive/nasa/casi.ntrs.nasa.gov/19770009539.pdf (accessed August 1, 2019).

[92] K. Azad, An Interactive Guide To The Fourier Transform, BetterExplained. (2012). https://betterexplained.com/articles/an-interactive-guide-to-the-fourier-transform/ (accessed July 25, 2019).

[93] S.P. Schneider, Development of Hypersonic Quiet Tunnels, Journal of Spacecraft and Rockets. 45 (2008) 641–664. https://doi.org/10.2514/1.34489.

[94] L. Bernstein, Force Measurements in Short-Duration Hypersonic Facilities, North Atlantic Treaty Organization, Queen Mary College, University of London, London, UK, 1975. https://apps.dtic.mil/dtic/tr/fulltext/u2/a018842.pdf (accessed July 20, 2019).

[95] R. Ziemer, W. Tranter, Signals and Linear Systems, in: Principles of Communications: Systems, Modulation and Noise, 6th ed., John Wiley & Sons, Hoboken, NJ, 2009: pp. 56–78.

[96] J.E. Harris, Force-coefficient and moment-coefficient correlations and air-helium simulation for spherically blunted cones, NASA Langley Research Center, Washington, DC, 1964.

[97] L. Roane, Aerodynamics Force and Moment Characteristics of Spheres and Cones at Mach 7.0 in Methane-Air Combustion Products, NASA Langley Research Center, Washington, DC, 1965.

[98] J.D. Anderson Jr., Conical Flow, in: Modern Compressible Flow: With Historical Perspective, 3rd ed., McGraw-Hill Higher Education, New York, NY, 2003: pp. 363–376.